Laboratory study of rotation-dominated convective turbulence

Matteo Madonia

European Research Council
Established by the European Commission

This research was supported by the European Research Council (ERC) under the European Union's Horizon 2020 research and innovation programme, Grant agreement No. 678634.

Cover design by Matteo Madonia
Printed by Gildeprint - Enschede

A catalogue record is available from the Eindhoven University of Technology Library

ISBN: 978-90-386-5468-3
NUR: 926

Laboratory study of rotation-dominated convective turbulence

PROEFSCHRIFT

ter verkrijging van de graad van doctor aan de Technische Universiteit Eindhoven, op gezag van de rector magnificus prof.dr.ir. F.P.T. Baaijens, voor een commissie aangewezen door het College voor Promoties, in het openbaar te verdedigen op woensdag 13 april 2022 om 16:00 uur

door

Matteo Madonia

geboren te Marino (RM), Italië

Dit proefschrift is goedgekeurd door de promotoren en de samenstelling van de promotiecommissie is als volgt:

voorzitter:	prof.dr.ir. G.M.W. Kroesen
1e promotor:	prof.dr. H.J.H. Clercx
co-promotor:	dr.ir. R.P.J. Kunnen
leden:	prof.dr. J.M. Aurnou (University of California, Los Angeles)
	prof.dr. M.R. de Baar
	prof.dr.ir. C. Poelma (Technische Universiteit Delft)
	dr.ir. R.J.A.M. Stevens (Universiteit Twente)
	dr. N.J. Dam

Het onderzoek of ontwerp dat in dit proefschrift wordt beschreven is uitgevoerd in overeenstemming met de TU/e Gedragscode Wetenschapsbeoefening.

Contents

Chapter 1

Introduction

The behavior of flows at planetary scales is a complex phenomenon that is characterized by many features. These flows are confined in spherical geometries (e.g. interiors of gas giants [1,2]), many have approximately flat domains (horizontal length scales much larger than vertical ones, e.g. ocean circulation [3–6], atmospheric flow [7]). Magnetic fields can also play a crucial role (e.g. Earth's liquid metal outer core [8–11]). All of them, though, are driven by buoyancy and strongly influenced by rotation. Moreover, all these flows have extremely large length scales and are very difficult to measure directly.

A basic model system that combines the principal effects of both buoyant forcing and rotation into a well-defined problem is rotating Rayleigh–Bénard convection (RRBC): the flow in a fluid layer confined between two horizontal plates, heated from below and cooled from above, while the whole system rotates about its vertical axis.

The study of (non-rotating) Rayleigh–Bénard convection (RBC) started from the studies of Henri Bénard and Lord Rayleigh more than a century ago. While Bénard observed a regular pattern of hexagonal cells in a thin layer of fluid heated from below [12–14], Rayleigh performed the theoretical analysis of the convective instability of a layer of fluid and found a critical parameter that determined the onset of convective flow [15]. This parameter that defines the strength of the buoyancy forcing is the Rayleigh number Ra (it will be formally defined in Chapter 2); it indicates the ratio of buoyancy and dissipation in the fluid. As we mentioned earlier, in this work classical Rayleigh–Bénard convection is modified with the addition of rotation. Rotational influence can be quantified with many critical dimensionless numbers, for example the Ekman number E (also, formally defined in Chapter 2) that indicates the ratio between viscous and Coriolis force; it is inversely proportional to the rotational strength.

Rotating Rayleigh–Bénard convection is, therefore, a simple but relevant model to investigate the interplay between these two forces that can give us deeper insights into geophysical and astrophysical flows, other than being a very intriguing flow configuration of fundamental interest. Buoyancy leads to

3D (three-dimensional) turbulence, while rotation wants to stabilize the flow giving it coherence along the rotation axis. This means that when the rotational influence is much stronger than buoyancy, convection does not set in and there is a specific threshold (a critical Rayleigh number, Ra_C) where it starts; at the other end of the spectrum, where rotation is not relevant anymore, we have non-rotating turbulent Rayleigh–Bénard convection. Our analysis lies between these two extremes.

As a result of their vast proportions, geophysical and astrophysical flows are governed by extreme values of the dimensionless parameters defined before, with $Ra \gtrsim 10^{15}$ and $E \lesssim 10^{-10}$ [5, 16–18]. At the same time, the critical Rayleigh number Ra_C for onset of convective motion is significantly higher when strong rotation is applied: for water (the working fluid used in this work) linear stability theory gives the asymptotic result $Ra_C = 8.6956E^{-4/3}$ in the limit of small E [19]. So, despite the huge Ra values most of these natural flows are still dominated by rotation, implying that the supercriticality Ra/Ra_C retains more modest values. This rotational constraint leads to the dominant force balance being between pressure gradient and Coriolis force, the so-called geostrophic balance [20]. In recent years it was found that this geostrophic state of rotating convection displays a diverse set of flow structures (cells, convective Taylor columns (CTCs), plumes and geostrophic turbulence (GT)) [21, 22] that we will describe in detail below. Each of these flow states is expected to display characteristic scaling behavior for flow statistics, like the convective heat transfer, intensity of temperature and velocity fluctuations and mean temperature gradient.

Flow states of rotating convection

It is known from previous studies [24–26] that rotation induces different regimes in Rayleigh–Bénard convection, but the subdivision of the geostrophic regime of rotating convection into different flow states is of more recent interest [22,27,28]. The states are listed and described below, from the one closest to the onset of convection (rotation dominated) to the one closest to non-rotating Rayleigh–Bénard convection (buoyancy dominated):

- Cells: in this state the flow takes the form of narrow cells, vortical structures aligned with the vertical axis and arranged on a quasi-steady grid (Fig. 1.1(a)).

- Convective Taylor columns (CTC): this state shows columnar structures, where each column is surrounded by a "shield" of oppositely-signed

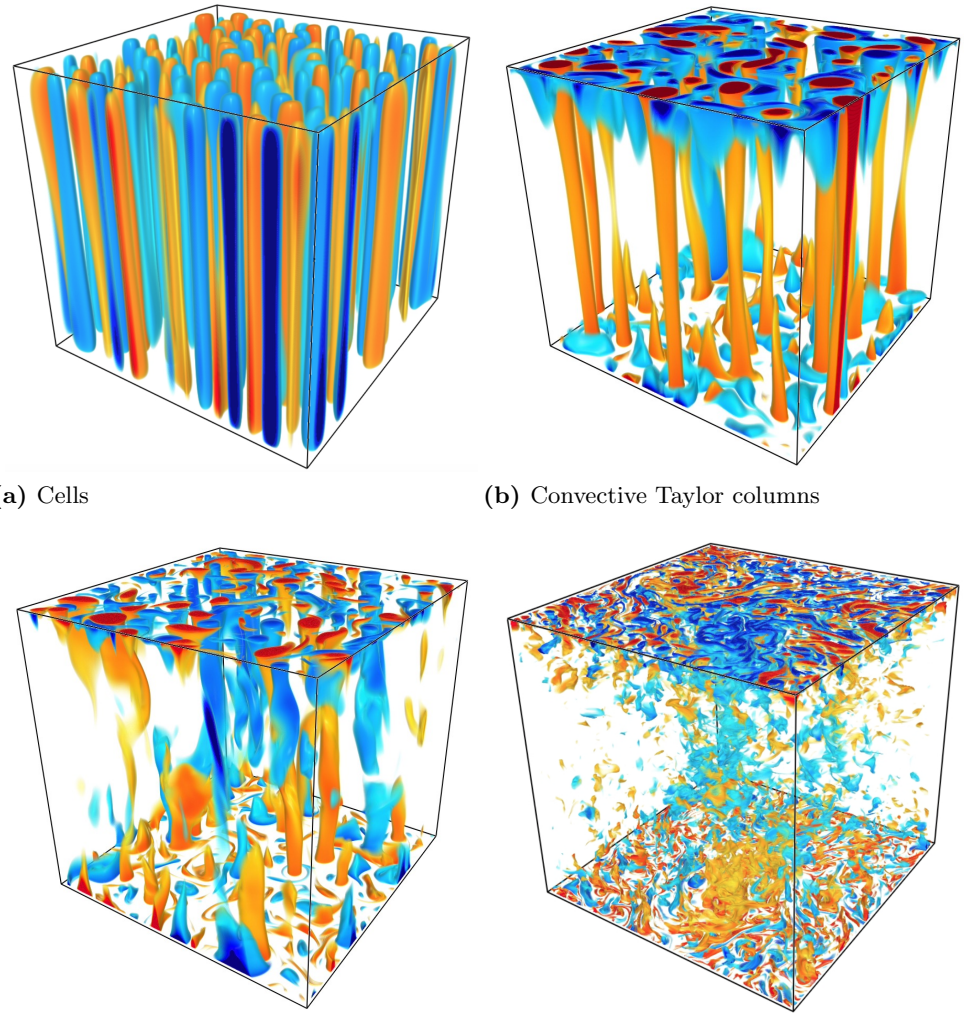

(a) Cells

(b) Convective Taylor columns

(c) Plumes

(d) Geostrophic turbulence

Figure 1.1: *Temperature fluctuations for direct numerical simulations in the regimes of (a) cells, (b) convective Taylor columns, (c) plumes, (d) geostrophic turbulence from Ref. [23]. The computational domain is taller than it is wide, for the purpose of these visualizations they have been stretched horizontally into a cubic geometry. The color scale is chosen to highlight the flow features, where red (blue) indicates temperatures above (below) average.*

vorticity and temperature. The shielding prevents collisions between columns, that are thus long-lasting structures that move around the domain (Fig. 1.1(b)).

- Plumes: at higher thermal forcing, the shields vanish and more vortex-to-vortex interaction is allowed. The flow partially loses its vertical coherence (Fig. 1.1(c)).
- Geostrophic turbulence (GT): in this state also the coherence of the plumes is lost, and a fluctuating turbulent flow state is present. An inverse energy cascade can be triggered, leading to large-scale vortices (LSVs), quasi-two-dimensional vortices that grow to fill the domain (Fig. 1.1(d)).
- Rotation-influenced turbulence (RIT): this novel state, described in further detail in the rest of the thesis, is a state where heat transfer and temperature gradient scalings made it appropriate to distinguish it as a separate regime from GT.
- Rotation-affected turbulence: here the geostrophic balance is no longer the leading balance, but rotation still accounts for some features like the loss of the large-scale circulation (LSC) [29], a characteristic feature of non-rotating Rayleigh–Bénard convection [30].

Scope of the thesis

To enter these flow states one needs to resort to specialized tools: asymptotically reduced models (e.g. Refs. [21, 31]), large-scale numerical simulations on fine meshes (e.g. Refs. [32–34]) or large-scale experiments [27].

Heat transfer measurements have shown that the geostrophic regime expands in size with increasing rotational constraint (decreasing E) [22, 35, 36]. Models that include infinite rotational forces ($E \to 0$) could characterize this regime and its flow states in more depth, even though in idealized settings [37]. Direct numerical simulations (DNS) can explore, at present day, only up to certain rotational influence (a minimum E of 10^{-7}), because of computational limitations [28, 38]. While simulations need to resolve the smallest active length scales to tackle the geostrophic regime, laboratory experiments can intrinsically "resolve" all the scales, even for features that are too small to detect. Laboratory experiments are thus a particularly appropriate approach to investigate the geostrophic regime at those extreme values of the key parameters.

Our work aims to investigate the geostrophic regime in an experimental setup, TROCONVEX, designed to maximize the coverage of that regime in parameter

space. That is why we employ a tall setup that can reach very large Ra and very small E at the same time. TROCONVEX can reach up to $Ra \approx 2 \times 10^{14}$ and can go as low as $E \approx 5 \times 10^{-9}$, that is about an order of magnitude more extreme than any previous rotating convection experiment [27].

A typical way to categorize flow behaviors is to measure the heat transfer efficiency: different states likely steer the flow towards different ways of heat transport. We present such measurements together with flow visualizations and an analysis of the mean temperature gradient across the system. Next to temperature measurements, there is a great demand for experimental flow analysis of geostrophic convection; here we also present the first results in that direction with the use of *in situ* flow measurements. We employ the technique of stereoscopic particle image velocimetry (stereo-PIV), which can measure the three components of the velocity field in a planar section. Stereo-PIV measurements are convenient for both identifying the flow structure and acquiring velocity statistics that describe the flow and its anisotropy.

Thesis outline

This thesis is structured as follows. Chapter 2 introduces the theoretical background of rotating Rayleigh–Bénard convection needed for this study. In Chapter 3 we present our experimental setup in the configuration used for the temperature measurements as well as the one used for the stereo-PIV experiments. From Chapter 4 we start with our analysis of the results and we show our flow visualizations and heat transfer measurements of the different flow states. Chapter 5 introduces our stereo-PIV measurements and gives an overview of the velocity and vorticity fields of seven rotating Rayleigh–Bénard convection cases and a non-rotating case. Then, Chapter 6 presents an analysis on the spatial autocorrelation of vertical velocity and vertical vorticity, introducing the quadrupolar vortex, a large-scale structure that arises in our confined geometry. An investigation of the energy spectra of the cases with an insight on energy transfer through the different length scales is presented in Chapter 7. Finally, in Chapter 8, we provide an overall conclusion including an outlook to future possibilities in the research and characterization of rotating Rayleigh–Bénard convection.

Chapter 2

Theoretical Background

In this chapter we shortly describe the theoretical background that is needed for the following chapters. We start from the equations of motions of our problem under study, rotating Rayleigh–Bénard convection, the key dimensionless quantities, and we address the effects of rotation and buoyancy in the bulk and near the boundaries of the flow domain and how these reflect in the flow phenomenology.

2.1 Equations of motion

The Rayleigh–Bénard convection setup consists of a fluid layer confined between two parallel horizontal plates, where the bottom one is heated and the top one is cooled. The temperature difference between the plates induces a buoyancy driven flow. This flow is generally described employing the Oberbeck-Boussinesq approximation [39, 40]. In this approximation we assume that the properties of the fluid are constant and independent of the fluid temperature and that the variations of density are only important in the buoyant forcing term and are linearly dependent on the temperature

$$\rho(T) = \rho(T_0)(1 - \alpha(T - T_0))\,, \tag{2.1}$$

where ρ is the fluid density, T is its temperature, T_0 is a reference temperature and α is the thermal expansion coefficient of the fluid. This approximation holds reasonably well for small temperature differences ($\alpha\Delta T \lesssim 0.2$ is often used as a rule of thumb [27, 41, 42]). Within this context, we can write the equations for conservation of mass, momentum and energy for an incompressible Newtonian fluid as

$$\boldsymbol{\nabla} \cdot \boldsymbol{u} = 0\,, \tag{2.2}$$

$$\frac{\partial \boldsymbol{u}}{\partial t} + (\boldsymbol{u} \cdot \boldsymbol{\nabla})\,\boldsymbol{u} = -\boldsymbol{\nabla} p + \nu \nabla^2 \boldsymbol{u} + g\alpha T' \hat{\boldsymbol{z}}\,, \tag{2.3}$$

$$\frac{\partial T'}{\partial t} + (\boldsymbol{u} \cdot \boldsymbol{\nabla})\, T' = \kappa \nabla^2 T' \,, \tag{2.4}$$

where $\boldsymbol{u}$ is the velocity, t is time, p is the pressure (with the mean density incorporated in the pressure term), ν is the kinematic viscosity of the fluid, g is the gravitational acceleration, T' in this case is the temperature relative to some reference temperature ($T' = T - T_0$, from now on we will refer to it as T for simplicity), κ is the thermal diffusivity of the fluid and $\hat{\boldsymbol{z}}$ the unit vector in the vertical direction.

Equations (2.2) to (2.4) are valid for inertial frames of reference. Since we are studying rotating convection, we are interested in the application of these equations in a rotating system. A detailed description of the derivation of the following equations are found in [20, 43]. We start by defining a coordinate system that rotates relative to the inertial frame with constant angular velocity $\boldsymbol{\Omega}$. The derivative of the position vector $\boldsymbol{r}$ (thus, the velocity) in the rotating frame is related to the derivative of the position vector $\boldsymbol{r}'$ in the inertial frame by

$$\frac{\mathrm{d}\boldsymbol{r}'}{\mathrm{d}t} = \frac{\mathrm{d}\boldsymbol{r}}{\mathrm{d}t} + \boldsymbol{\Omega} \times \boldsymbol{r} \,. \tag{2.5}$$

Following the same approach we can derive acceleration as

$$\begin{aligned} \frac{\mathrm{d}^2\boldsymbol{r}'}{\mathrm{d}t^2} &= \frac{\mathrm{d}}{\mathrm{d}t}\left(\frac{\mathrm{d}\boldsymbol{r}'}{\mathrm{d}t}\right) + \boldsymbol{\Omega} \times \left(\frac{\mathrm{d}\boldsymbol{r}'}{\mathrm{d}t}\right) = \\ &= \frac{\mathrm{d}^2\boldsymbol{r}}{\mathrm{d}t^2} + 2\boldsymbol{\Omega} \times \frac{\mathrm{d}\boldsymbol{r}}{\mathrm{d}t} + \boldsymbol{\Omega} \times \boldsymbol{\Omega} \times \boldsymbol{r} \end{aligned} \tag{2.6}$$

or

$$\boldsymbol{a}' = \boldsymbol{a} + 2\boldsymbol{\Omega} \times \boldsymbol{u} - \Omega^2 \boldsymbol{r}_\perp \tag{2.7}$$

where $\boldsymbol{a}'$ and $\boldsymbol{a}$ are respectively the accelerations in the inertial and the rotating frames, and $\boldsymbol{r}_\perp$ denotes the projection of the position vector $\boldsymbol{r}$ on the plane perpendicular to $\boldsymbol{\Omega} = \Omega\hat{\boldsymbol{z}}$. The last two terms of Equation (2.6) and Equation (2.7) represent the Coriolis and the centrifugal accelerations, respectively. The centrifugal term can be rewritten as a gradient ($\Omega^2 \boldsymbol{r}_\perp = \boldsymbol{\nabla}(\frac{1}{2}\Omega^2 \boldsymbol{r}_\perp^2)$) and incorporated in the pressure gradient term of the momentum conservation equation, so that $\boldsymbol{\nabla} p \to \boldsymbol{\nabla}(p - \frac{1}{2}\Omega^2 \boldsymbol{r}_\perp^2)$, the so-called reduced pressure. In the end, the momentum equation that describes rotating Rayleigh–Bénard convection becomes

$$\frac{\partial \boldsymbol{u}}{\partial t} + (\boldsymbol{u} \cdot \boldsymbol{\nabla})\, \boldsymbol{u} + 2\boldsymbol{\Omega} \times \boldsymbol{u} = -\boldsymbol{\nabla} p + \nu \nabla^2 \boldsymbol{u} + g\alpha T \hat{\boldsymbol{z}} \,. \tag{2.8}$$

2.2 Dimensionless numbers

We have presented the equations of motion using dimensional quantities, but they can be rewritten in a nondimensional fashion to reduce the parameter space and better understand the ratios of the forces involved. To do so, we normalize lengths by the distance between the two plates H, velocities by a characteristic velocity scale U (that will be further analyzed later), time by H/U, temperature by the temperature difference between the two plates ΔT and pressure by $\rho_0 U^2$. Thus, Equations (2.2), (2.4) and (2.8) become

$$\boldsymbol{\nabla} \cdot \boldsymbol{u} = 0\,, \tag{2.9}$$

$$\frac{\partial \boldsymbol{u}}{\partial t} + (\boldsymbol{u} \cdot \boldsymbol{\nabla})\,\boldsymbol{u} + \frac{2\Omega H}{U}\hat{\boldsymbol{z}} \times \boldsymbol{u} = -\boldsymbol{\nabla} p + \frac{\nu}{UH}\nabla^2 \boldsymbol{u} + \frac{g\alpha \Delta T H}{U^2} T \hat{\boldsymbol{z}}\,, \tag{2.10}$$

$$\frac{\partial T}{\partial t} + (\boldsymbol{u} \cdot \boldsymbol{\nabla})\,T = \frac{\kappa}{UH}\nabla^2 T\,. \tag{2.11}$$

where all the symbols now represent nondimensionalized quantities.

In Rayleigh–Bénard convection it is customary to use the free-fall velocity $U_{ff} = \sqrt{g\alpha\Delta T H}$ as the characteristic velocity scale, since it is assumed that the buoyancy term is the leading one and so $g\alpha\Delta T H/U^2 \sim \mathcal{O}(1)$ [44]. This velocity is an upper bound that would represent the case where all the heating power is transferred into fluid motions [45–47]. We can now introduce the two dimensionless groups that are classically related to Rayleigh–Bénard convection, the Rayleigh number and the Prandtl number, and one that is related to rotating flows, the Rossby number [19]:

$$Ra = \frac{g\alpha\Delta T H^3}{\nu\kappa}\,, \tag{2.12}$$

$$Pr = \frac{\nu}{\kappa}\,, \tag{2.13}$$

$$Ro = \frac{U}{2\Omega H}\,. \tag{2.14}$$

The Rayleigh number indicates the strength of the buoyancy forcing, the Prandtl number describes the diffusive properties of the fluid and the Rossby number indicates the ratio between inertial and Coriolis forces. With the choice of $U = U_{ff}$ we can redefine the Rossby number as a *convective* Rossby number

$$Ro_C = \frac{\sqrt{g\alpha\Delta T/H}}{2\Omega} \tag{2.15}$$

and rewrite the equations as

$$\boldsymbol{\nabla} \cdot \boldsymbol{u} = 0\,, \tag{2.16}$$

$$\frac{\partial \boldsymbol{u}}{\partial t} + (\boldsymbol{u} \cdot \boldsymbol{\nabla})\,\boldsymbol{u} + \frac{1}{Ro_C}\hat{\boldsymbol{z}} \times \boldsymbol{u} = -\boldsymbol{\nabla} p + \sqrt{\frac{Pr}{Ra}}\nabla^2 \boldsymbol{u} + T\hat{\boldsymbol{z}}\,, \tag{2.17}$$

$$\frac{\partial T}{\partial t} + (\boldsymbol{u} \cdot \boldsymbol{\nabla})\,T = \frac{1}{\sqrt{PrRa}}\nabla^2 T\,. \tag{2.18}$$

It is also possible to indicate the strength of the rotation influence by a number of other dimensionless numbers: in fact, for our studies, we will use mainly the Ekman number, defined as

$$E = \frac{\nu}{2\Omega H^2} = Ro_C\sqrt{\frac{Pr}{Ra}}\,, \tag{2.19}$$

which provides the ratio of viscous to Coriolis forces. This quantity has the advantage of not depending on the velocity scale U, and it is useful when comparing different rotating convective flows with different characteristic velocity scales. It should also be noted that both Ro and E are inversely proportional to the rotation rate, i.e. they are small when the rotational influence is strong. It is also possible to introduce an alternative velocity scale: the viscous diffusion velocity

$$U_\nu = \nu/H\,. \tag{2.20}$$

It indicates the rate at which viscous forces significantly diffuse the fluid momentum over the characteristic length scale. This scale can be convenient since it does not depend on the Rayleigh number. Two final important dimensionless control parameters that we need to introduce, since we will describe turbulent convection bounded in a cylindrical cell, is the aspect ratio of the set up and the Froude number, defined respectively as

$$\Gamma = \frac{D}{H}\,, \tag{2.21}$$

$$Fr = \frac{\Omega^2 D}{2g}\,, \tag{2.22}$$

where D is the diameter of the cylindrical cell of radius R. While the aspect ratio describes the geometry of the volume, the Froude number is the ratio between centrifugal and gravitational acceleration. In order to properly study rotating Rayleigh–Bénard convection it is important to keep the Froude number small enough in order to exclude centrifugation as another relevant parameter.

The typical output measures of Rayleigh–Bénard convection are usually the

dimensionless Nusselt number

$$Nu = \frac{qH}{k\Delta T}\,, \tag{2.23}$$

where q is the measured heat flux and k the thermal conductivity, and the Reynolds number

$$Re = \frac{u^{RMS}H}{\nu}\,, \tag{2.24}$$

where u^{RMS} is the magnitude of the velocity fluctuations, i.e. the root-mean-square velocity $u^{RMS} \equiv \sqrt{\langle u^2\rangle - \langle u\rangle^2}$. The Nusselt number represents the ratio between the total heat transfer (convection and conduction) and the heat transferred through conduction, in absence of convection, whereas the Reynolds number represents the ratio between inertial and viscous forces or the "strength" of turbulence.

Rotation and convection are the two main forces of rotating Rayleigh–Bénard convection, and they give opposite effects to the flow. While rotation wants to make the fluid more stable, convection has a strong mixing action. This means that for low enough values of E (or Ro) the flow is so stable that no convection takes place, and heat is only transferred via conduction (in this case $Nu = 1$), but at a certain critical Rayleigh number Ra_C we have the onset of convective motions. This Ra_C is given by

$$Ra_C = 8.7E^{-4/3}\,, \tag{2.25}$$

for a rapidly rotating ($E \lesssim 10^{-3}$) laterally unbounded fluid layer and for $Pr \geq 0.68$ [19, 48]. In these fluids, like water, convection sets in as steady convection cells. The characteristic horizontal wavelength of these structures (for the case of the rapidly rotating unbounded layer) is given (again, for fluids with $Pr \geq 0.68$) by [19, 49, 50]

$$\lambda_C/H = 4.8E^{1/3}\,. \tag{2.26}$$

In this work we will frequently resort to the definition of the supercriticality Ra/Ra_C, in order to indicate the "distance" of our study cases from the critical value for onset of convection at the selected Ekman number.

2.3 Geostrophic balance

We have discussed the Navier-Stokes equations for rotating flows in their complete form with the use of the Boussinesq approximation. Now we introduce

another simplification of the system, considering a quasi-steady flow, with inertial forces that are negligible compared to Coriolis forces ($Ro \ll 1$) and analyzing the bulk where viscous effects are negligible ($E \to 0$). The equation of momentum conservation is reduced to

$$2\Omega\hat{\boldsymbol{z}} \times \boldsymbol{u} = \boldsymbol{\nabla} p + g\alpha T\hat{\boldsymbol{z}}\,, \tag{2.27}$$

or, in its component form

$$-2\Omega v = -\frac{\partial p}{\partial x}\,, \tag{2.28}$$

$$2\Omega u = -\frac{\partial p}{\partial y}\,, \tag{2.29}$$

$$0 = -\frac{\partial p}{\partial z} + g\alpha T \tag{2.30}$$

with $\boldsymbol{u} = (u, v, w)$. Equations (2.28) and (2.29) are the so-called *geostrophic balance* between Coriolis force and pressure gradient, that is representative for planetary scale flows. This implies that isobars are streamlines and fluid parcels move along them. Equation (2.30) represents the *hydrostatic balance*, where temperature sets the density having used the Boussinesq approximation.

By taking the derivative of Equation (2.28) with respect to y, and Equation (2.29) with respect to x and subtract the two equations, we arrive at

$$-2\Omega\left(\frac{\partial u}{\partial x} + \frac{\partial v}{\partial y}\right) = 0 \tag{2.31}$$

which, in combination with the incompressibility condition $\boldsymbol{\nabla} \cdot \boldsymbol{u} = 0$, gives

$$\frac{\partial w}{\partial z} = 0\,. \tag{2.32}$$

If we take the derivative of Equations (2.28) and (2.29) to z and make use of Equation (2.30), we arrive at

$$2\Omega\frac{\partial v}{\partial z} = g\alpha\frac{\partial T}{\partial x}\,, \tag{2.33}$$

$$2\Omega\frac{\partial u}{\partial z} = -g\alpha\frac{\partial T}{\partial y}\,, \tag{2.34}$$

that together with Equation (2.32) can be rewritten as

$$\frac{\partial \boldsymbol{u}}{\partial z} = \frac{g\alpha}{2\Omega}\hat{\boldsymbol{z}} \times \boldsymbol{\nabla} T\,, \tag{2.35}$$

that is the *thermal wind balance* [51]. This means that, under the assumptions that we made, vertical velocity gradients can only be caused by horizontal temperature gradients and that vertical gradients of w are zero.

For a barotropic fluid, with density independent of temperature, we have

$$\frac{\partial \boldsymbol{u}}{\partial z} = \mathbf{0}\,, \tag{2.36}$$

that is the Taylor-Proudmann theorem [52, 53]. This implies that for an isothermal fluid, under the mentioned conditions, vertical variation of velocity is not permitted and that the flow is essentially two-dimensional, away from the boundaries.

2.4 Boundary layers

In Section 2.3 we saw that when viscous effects are negligible and rotation is dominant ($Ro \ll 1$) the horizontal motion of the flow is governed by the geostrophic balance (Eqs. (2.28) and (2.29)). Since these equations are based on the assumption that viscosity can be neglected, they are only valid away from the boundaries. In our case, though, rotating Rayleigh–Bénard convection is heavily influenced by its (no-slip) walls and in different ways: the boundary layer that emerge in the proximity of the bottom and top plates are called the Ekman boundary layers, while the zone close to the sidewalls is called the Stewartson boundary layer.

Ekman boundary layer

The equations describing the velocities inside the Ekman boundary layer can be derived from the Navier-Stokes equations with some simplifications: we assume that the bulk flow is in geostrophic balance, we assume that the flow is quasi-steady (i.e. $\partial/\partial t \to 0$) and we apply the usual boundary-layer approximation that wall-normal derivatives are much larger than derivatives along the wall. The components of the velocity can then be expressed as [20, 43]

$$u_E = u_B - \left[u_B \cos\left(z/\delta_E\right) + v_B \sin\left(z/\delta_E\right)\right] e^{-z/\delta_E}\,, \tag{2.37}$$

$$v_E = v_B + \left[u_B \sin\left(z/\delta_E\right) - v_B \cos\left(z/\delta_E\right)\right] e^{-z/\delta_E}\,, \tag{2.38}$$

$$w_E = \frac{\omega_B \delta_E}{2}\left\{1 - e^{-z/\delta_E}\left[\sin\left(z/\delta_E\right) + \cos\left(z/\delta_E\right)\right]\right\}\,, \tag{2.39}$$

where u_E,v_E and w_E are the velocities inside the Ekman boundary layer, u_B,v_B and w_B are the velocities in the bulk, $\delta_E = \sqrt{\nu/\Omega}$ is the Ekman boundary layer thickness and $\omega_B = \partial v_B/\partial x - \partial u_B/\partial y$ is the vertical vorticity in the bulk. We can also see that

$$\frac{\delta_E}{H} \sim E^{1/2}\,. \tag{2.40}$$

Notice that we derived the vertical velocity equation using the horizontal ones, the incompressibility condition and integrating with $\boldsymbol{u} = \boldsymbol{0}$ at $z = 0$. Instead, far outside the boundary layer ($z/\delta_E \to \infty$), where $\boldsymbol{u} = \boldsymbol{u}_B$, we find that

$$\lim_{z/\delta_E \to \infty} w_E = w_B = \frac{\omega_B \delta_E}{2}\,, \tag{2.41}$$

implying that the Ekman boundary layer actively influences the bulk flow through vertical motion with a magnitude that is set by the bulk vorticity. For $\omega_B > 0$ there is a flux from the boundary layer into the bulk (*Ekman pumping*), whereas for $\omega_B < 0$ we have the opposite (*Ekman suction*). Eq. (2.41) is valid near the bottom wall, while for the top wall we need to add a minus sign. This says that the Ekman layer can drive a secondary flow, since there is a flux of magnitude $\mathcal{O}(\delta_E \sim E^{1/2})$ through the layer whenever $\omega_B \neq 0$.

Stewartson boundary layer

As we noticed in the previous section, the bottom and top Ekman layer can cause a secondary circulation. For laterally bounded geometries (like, in our case, a cylinder) that circulation must be closed. This is done with a boundary layer on the sidewall, the Stewarson boundary layer [20, 54–56].

In a cylindrical geometry like our experimental setup, we can assume to have a geostrophic bulk and Ekman layers next to the top and bottom plates. If the geostrophic flow has, for example, a constant negative vorticity ω_B, there is a net radial outward flux of $\mathcal{O}(E^{1/2})$ in each of the Ekman layers generated by the Ekman suction. These fluxes go into the sidewall, in the Stewartson layer that therefore must have an $\mathcal{O}(E^{1/2})$ vertical flux. From [54–56] we know that we can expect a layer of thickness

$$\delta_{S,1/4}/H \sim E^{1/4} \tag{2.42}$$

that carries this vertical flux. To connect also to the sidewall where the azimuthal velocity is zero, we find an additional layer within the $E^{1/4}$ layer, with a thickness of

$$\delta_{S,1/3}/H \sim E^{1/3} \tag{2.43}$$

from the sidewall. The flows inside these two nested layers close the circulation set by the Ekman layers.

2.5 Convective turbulence

We have described rotating convection in the limit of strong rotational influence ($Ro \ll 1$), but geostrophic flows at extreme parameters can show turbulent behavior at small scales. In rotating Rayleigh–Bénard convection, the flow becomes turbulent for high enough Ra. The buoyancy forcing continuously gives energy to a range of active scales, and this energy is transferred to smaller scales through nonlinear processes (vortex stretching) until it is dissipated into heat. If the system is in an equilibrium state, the constant input of energy is matched by dissipation. We therefore have two important quantities in convective turbulence, the dissipation rates of kinetic energy ϵ and of thermal variance N defined as [57]

$$\epsilon \equiv \nu |\boldsymbol{\nabla u}|^2 \,, \tag{2.44}$$

$$N \equiv \kappa |\boldsymbol{\nabla} T|^2 \,. \tag{2.45}$$

The smallest active length scales of velocity and temperature fields are respectively the Kolmogorov length η and the Batchelor length η_T. They are defined according to [57]

$$\eta \equiv \left(\frac{\nu^3}{\epsilon} \right)^{1/4} , \tag{2.46}$$

$$\eta_T \equiv \eta \sqrt{\frac{\kappa}{\nu}} = \left(\frac{\nu \kappa^2}{\epsilon} \right)^{1/4} . \tag{2.47}$$

These quantities can be rewritten in a dimensionless form as

$$\epsilon = \sqrt{\frac{Pr}{Ra}} |\boldsymbol{\nabla u}|^2 \,, \quad N = \frac{1}{\sqrt{PrRa}} |\boldsymbol{\nabla} T|^2 \,, \tag{2.48}$$

$$\eta = \left(\frac{Pr}{Ra} \right)^{3/8} \epsilon^{-1/4} \,, \quad \eta_T = \eta Pr^{-1/2} = \left(Ra^3 Pr \epsilon^2 \right)^{-1/8} \,, \tag{2.49}$$

where all the symbols now represent nondimensionalized quantities. The dissipation rates are local quantities, and they may vary considerably between the bulk and the boundary regions of the flow. Global averaged quantities (averaged over time and volume of the considered domain) can be derived for

(non)rotating Rayleigh–Bénard convection as [58, 59]

$$\langle \epsilon \rangle = \frac{Nu - 1}{\sqrt{PrRa}}\,, \quad \langle N \rangle = \frac{Nu}{\sqrt{PrRa}}\,. \tag{2.50}$$

Chapter 3

Experimental Setup

In this chapter, we introduce our experimental setup TROCONVEX used in this work. First, we present the setup in the configuration used to acquire temperature measurements, explaining its characteristics and some specifics of the measurement techniques that we employ. We then present a complete list of the explored cases for the heat transfer measurements. In the last section, we describe the changes for the configuration used for the stereo-PIV measurements and the parameters of the selected cases.

3.1 Experimental apparatus for temperature measurements[1]

TROCONVEX (Fig. 3.1) is a rotating convection apparatus designed and constructed at Eindhoven University of Technology. The experimental vessel is a Lexan cylinder of height H up to 4 m and constant diameter $D = 0.39$ m, filled with water and held between copper plates which form the upper and lower boundaries. The mean temperature of the water is kept at 31°C, corresponding to $Pr \approx 5.2$ (see Table 3.1 for exact conditions per run). The adverse temperature gradient is imposed at the top and bottom boundaries: heat is passed into the system through the bottom plate by an electrical resistance heater and extracted from the top plate via a water-cooled heat exchanger. The heater, connected to a custom-made power supply, supplies between 4 and 1200 W to the system for this study. The top heat exchanger consists of a double-wound spiral passage through which water recirculates from an external coupled Thermoflex 2500 chiller/Sahara AC200 thermostated bath system. The Lexan cylinder is split up vertically into multiple segments,

[1] The contents of this section have been adopted from J. S. Cheng, M. Madonia, A. J. Aguirre Guzmán, and R. P. J. Kunnen. Laboratory exploration of heat transfer regimes in rapidly rotating turbulent convection. *Phys. Rev. Fluids*, 5(11):113501, 2020 [60]; some symbols have been changed from the article to match with the current notation.

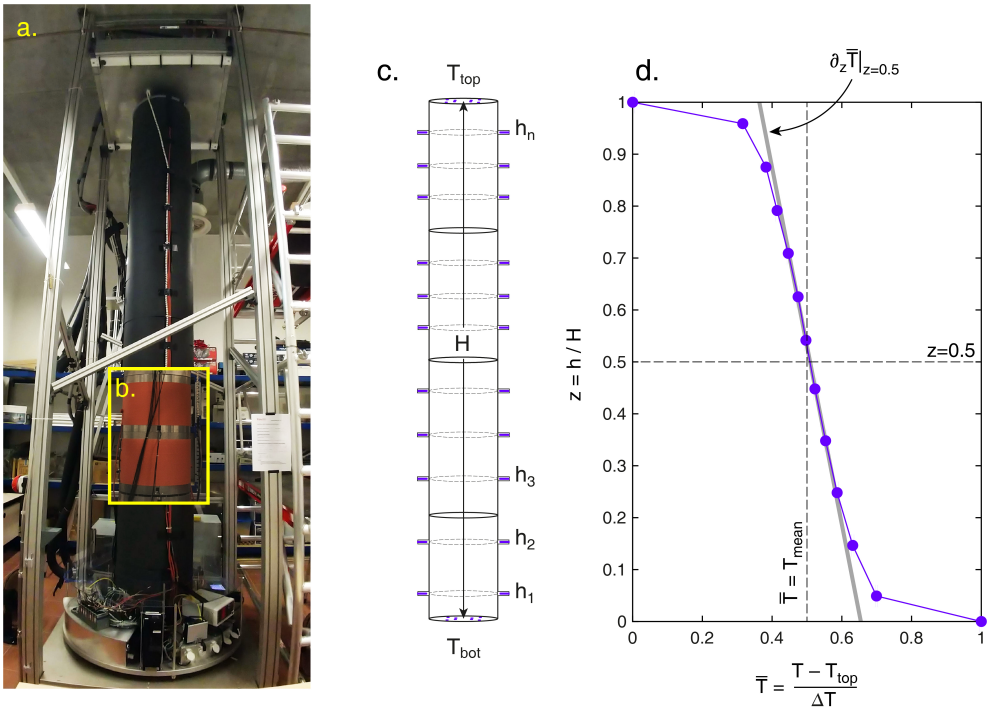

Figure 3.1: *(a) A photograph of the 4 m high rotating convection setup TROCONVEX. A several centimeter thick layer of black insulating foam covers the experimental vessel. (b) A cutout showing the strip heaters underneath the outermost layer of foam. These heaters match the temperature of the fluid layer to minimize sidewall thermal losses. (c) Sidewall thermistor placements. (d) Example of a normalized temperature profile from the* $E = 1.00 \times 10^{-8}$, $Ra = 8.66 \times 10^{12}$ *case. The temperatures at each height are averaged over time and space. The quantity* $-\partial_z \overline{T}\big|_{z=0.5}$ *is derived from a linear fit through the middle six temperatures.*

allowing us to use $H = 0.8$, 2.0 and 4.0 m tank heights (aspect ratio $\Gamma = D/H \approx 1/2$, 1/5 and 1/10, respectively) to cover broader parameter ranges. We conduct many experiments that overlap in parameter values at different tank heights (see Table 3.1) which have, thus far, shown no significant effect of aspect ratio Γ on the heat transfer.

As is clear in Fig. 3.1d, the bulk region of the fluid can contain significant temperature gradients. In order to control heat losses through the sidewall with precision, each segment is further subdivided vertically into two or three sections [Fig. 3.1b], each of which is wrapped in insulating foam, covered with an aluminium heat shield in contact with a flexible resistance strip heater (eleven sections total at $\Gamma = 1/10$). Two negative temperature coefficient (NTC) resistance thermistors are placed at the mid-height of each section,

opposite one another (i.e., separated by 180°), to measure the temperature of the fluid layer; their average temperature is then used as a set point for the corresponding heater. Layers of insulation separate and surround all of these components such that the heaters only passively follow the set point without actively heating the fluid layer. Losses through the Lexan sidewall are therefore minimized even in the presence of large vertical temperature gradients. The sidewall thermistors also turn out to be an important diagnostic tool, described in Section 3.2.

The experimental vessel, power supply, and measurement instruments and controllers are all mounted on the rotating table. Rotation is powered by a Lenze geared motor and gearbox which is connected to a large gear fixed under the table. This allows for precise control of the rotation rate, necessary for maintaining specific Ekman numbers E. For the purpose of this study, centrifugal effects are an unwanted externality, and we seek to reduce them as much as possible. Centrifugation is characterized by the Froude number, $Fr = \Omega^2 D/2g$, the ratio between centrifugal forcing at the sidewall of the tank and gravitational acceleration. We maintain $Fr < 0.12$ throughout all cases (see Table 3.1), meaning gravity is roughly an order of magnitude stronger than centrifugal acceleration even at the sidewall. Ref. [61] argue, though, that centrifugation is significant as long as $Fr \gtrsim \Gamma/2$, with simulation results showing the temperature gradient at the sidewall experiencing much greater vertical asymmetry than that measured in the bulk. The $E = 10^{-8}$ cases at $\Gamma = 1/10$ then exceed this limitation by a factor of two. However, temperature profiles (such as the example shown in Fig. 3.1d, where $Fr = 0.115$) lack the strong vertical asymmetry predicted by [61], and we believe that centrifugation plays a minimal role in our cases.

3.2 Temperature measurement techniques[2]

The results in Chapter 4 are mainly derived from temperature measurements by NTC resistance thermistors installed in the top, bottom, and sidewall boundaries of the vessel, within 0.7 mm of the fluid layer [Fig. 3.1c]. The top and bottom boundaries have identical configurations of eight thermistors spaced out horizontally across the copper plates, while the sidewall thermistors are arranged two per height. The number of sidewall measurements therefore de-

[2]The contents of this section have been adopted from J. S. Cheng, M. Madonia, A. J. Aguirre Guzmán, and R. P. J. Kunnen. Laboratory exploration of heat transfer regimes in rapidly rotating turbulent convection. *Phys. Rev. Fluids*, 5(11):113501, 2020 [60]; some symbols have been changed from the article to match with the current notation.

pends on Γ, with $n = 2$, 5, and 11 measurement heights for the $\Gamma = 1/2$, $1/5$, and $1/10$ tanks, respectively. Measurements are taken once per second, simultaneously across all thermistors, for $N = \mathcal{O}\left(10^4 - 10^5\right)$ seconds[3] . Global heat transfer parameters Nu and Ra rely on our measurements of $\Delta T = T_{\text{bot}} - T_{\text{top}}$, where T_{bot} and T_{top} are the horizontally averaged temperatures at the bottom and top boundaries, respectively. We calculate the fluid properties of water based on the average temperature, $T_{\text{mean}} = \left(T_{\text{bot}} + T_{\text{top}}\right)/2$, and using formulae from [62].

Heat flux through the fluid layer, needed to calculate the Nusselt number Nu, is measured by a Hioki PW3335 power meter. A small amount of heating power is lost from the other side of the heat pad and the sidewalls and dissipated to the room instead of contributing to heating the fluid layer. We estimate these heat losses by manually inputting a temperature setpoint of 31°C at top, bottom, and sidewall of the fluid layer, and observing the amount of heating power that must be supplied by the bottom heater to maintain this state. This quantity (about 0.58 W for the 2 m tank setup, and estimated to be approximately twice as large for the 4 m setup) is then subtracted from the total heating power for calculating Nu. The analysis of the statistical error in quantities measured over long times is detailed in Section 4.2.

As with the top and bottom boundary temperatures, sidewall temperatures are averaged over time and between the (two) thermistors at the same vertical position h. The raw temperature profile for each case can be written $[T_{\text{bot}},\ T(h_1),\ T(h_2), ...,\ T(h_n),\ T_{\text{top}}]$. We normalize this profile as

$$\overline{T} = \frac{T - T_{\text{top}}}{\Delta T}\,. \tag{3.1}$$

The mid-height temperature gradient $-\partial_z \overline{T}\big|_{z=0.5}$ is then defined as a best-fit linear trend of $\overline{T}$ versus z for temperatures in the vicinity of $z = 0.5H$: we use $\overline{T}(h_1,\ h_2)$ for $\Gamma = 1/2$, $\overline{T}(h_1,\ h_2,\ ...,\ h_5)$ for $\Gamma = 1/5$, and $\overline{T}(h_3,\ h_4,\ ...,\ h_8)$ for $\Gamma = 1/10$.

We note that previous studies in nonrotating convection report different temperature profiles at the sidewall versus the axial region of the vessel [63]. This is not the case, however, in rotating convection: in Fig. 3.2 we plot $-\partial_z \overline{T}\big|_{z=0.5}$ versus Ro for cylindrical rotating DNS with non-slip boundaries conducted in [24] and [38]. Unlike nonrotating convection, the sidewall and axial temperature gradients match closely when rotation affects the flow ($Ro_C \lesssim 1$ and

[3] These time scales correspond to a range of $\tau_\kappa = \mathcal{O}\left(10^{-3} - 10^{-2}\right)$ in thermal diffusion time scale units ($\tau_\kappa = H^2/\kappa$) and $\tau_{ff} = \mathcal{O}\left(10^3 - 10^4\right)$ in free-fall time scale units ($\tau_{ff} = H/U_{ff}$)

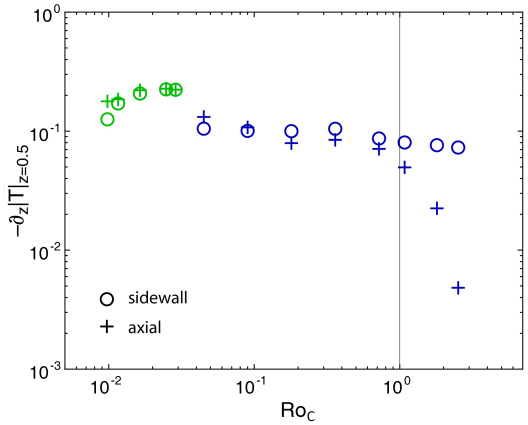

Figure 3.2: *The mid-height temperature gradient (3.1) at the wall ($r = D/2$, circles) and at the central axis ($r = 0$, pluses) in cylindrical rotating convection DNS with non-slip boundary conditions. Data from [24] (blue symbols): Ekman numbers range from $3.6 \times 10^{-6} \leq E \leq 2.0 \times 10^{-4}$ at constant $Ra = 10^9$ and $Pr = 6.4$. Data from [38] (green symbols): Rayleigh numbers $5.0 \times 10^{10} \leq Ra \leq 4.3 \times 10^{11}$ at constant $E = 10^{-7}$ and $Pr = 5.2$. The sidewall and axial temperature gradients match closely for large part of the Ro_C range. They start to diverge only when rotation starts dominating (for $Ro_C \lesssim 10^{-2}$ in [38]) or when rotational influence is mostly lost (for $Ro_C \gtrsim 1$ in [24]).*

$Fr \ll 1$) [45]. Only when rotation starts dominating the flow, in the columnar flow regime, do we see axial and sidewall gradients diverge a bit again (at $Ro_C \lesssim 10^{-2}$ for [38]). Note that the majority of our rotating data exist in the intermediate range where the gradients are equal irrespective of the radial position.

Table 3.1: *Experimental data from TROCONVEX. $\Gamma = 0.494, 0.195$, and 0.097 cases are from the 0.8 m, 2 m, and 4 m high setups, respectively. Nonrotating cases are listed first. Some cases do not have $-\partial_z\overline{T}\big|_{z=0.5}$ values because they were conducted prior to implementation of sidewall temperature measurements (by the NTC resistance thermistors).*

Γ	E	Fr	Ra	Nu	Pr	T_{mean} [°C]	ΔT [°C]	$-\partial_z\overline{T}\big\|_{z=0.5}$
0.494	∞	0	8.49 ($\pm$0.20) $\times 10^{9}$	121 ($\pm$3)	5.99	25.48	0.85	0.052
0.494	∞	0	1.41 ($\pm$0.02) $\times 10^{10}$	146 ($\pm$2)	6.00	25.41	1.41	0.068
0.494	∞	0	2.75 ($\pm$0.02) $\times 10^{10}$	165 ($\pm$1)	6.65	21.50	3.51	–
0.494	∞	0	4.25 ($\pm$0.03) $\times 10^{10}$	199 ($\pm$1)	6.65	21.52	5.41	–
0.494	∞	0	6.87 ($\pm$0.07) $\times 10^{10}$	238 ($\pm$2)	5.99	25.45	6.86	0.038
0.494	∞	0	8.41 ($\pm$0.06) $\times 10^{10}$	253 ($\pm$2)	6.73	21.10	11.00	–
0.494	∞	0	1.45 ($\pm$0.01) $\times 10^{11}$	292 ($\pm$2)	6.75	20.99	19.07	–
0.494	∞	0	2.43 ($\pm$0.04) $\times 10^{11}$	345 ($\pm$5)	5.73	27.21	21.97	0.035
0.494	∞	0	2.69 ($\pm$0.03) $\times 10^{11}$	363 ($\pm$3)	6.33	23.33	30.38	–
0.195	∞	0	1.89 ($\pm$0.04) $\times 10^{11}$	298 ($\pm$7)	5.21	31.01	0.87	0.109
0.195	∞	0	3.41 ($\pm$0.06) $\times 10^{11}$	334 ($\pm$6)	5.21	31.06	1.57	0.079
0.195	∞	0	6.64 ($\pm$0.07) $\times 10^{11}$	448 ($\pm$5)	5.21	31.01	3.06	0.069
0.195	∞	0	1.11 ($\pm$0.01) $\times 10^{12}$	534 ($\pm$6)	5.21	31.04	5.13	0.059
0.195	∞	0	1.90 ($\pm$0.02) $\times 10^{12}$	643 ($\pm$7)	5.18	31.30	8.64	0.051
0.195	∞	0	3.80 ($\pm$0.03) $\times 10^{12}$	781 ($\pm$5)	5.21	31.03	17.49	0.045
0.195	∞	0	6.49 ($\pm$0.06) $\times 10^{12}$	921 ($\pm$8)	5.22	30.98	29.94	0.042
0.097	∞	0	8.75 ($\pm$0.36) $\times 10^{11}$	519 ($\pm$27)	5.22	30.98	0.51	0.150
0.097	∞	0	1.74 ($\pm$0.04) $\times 10^{12}$	639 ($\pm$17)	5.22	30.98	1.01	0.118
0.097	∞	0	3.45 ($\pm$0.97) $\times 10^{12}$	778 ($\pm$23)	5.22	30.99	1.99	0.093

Γ	E	Fr	Ra	Nu	Pr	T_{mean} [°C]	ΔT [°C]	$-\partial_z \overline{T}\big\vert_{z=0.5}$
0.097	∞	0	8.66 ($\pm$0.07) $\times 10^{12}$	996 ($\pm$19)	5.22	30.98	5.01	0.080
0.097	∞	0	1.73 ($\pm$0.01) $\times 10^{13}$	1279 ($\pm$9)	5.22	31.00	9.99	0.071
0.097	∞	0	3.46 ($\pm$0.03) $\times 10^{13}$	1593 ($\pm$15)	5.22	30.99	20.00	0.066
0.097	∞	0	5.19 ($\pm$0.06) $\times 10^{13}$	1820 ($\pm$20)	5.22	31.00	29.99	0.061
0.097	∞	0	6.83 ($\pm$0.09) $\times 10^{13}$	1993 ($\pm$25)	5.00	32.78	36.44	0.063
0.494	2.88×10^{-7}	0.092	1.12 ($\pm$0.02) $\times 10^{10}$	25 ($\pm$1)	5.22	30.94	0.84	0.193
0.494	2.88×10^{-7}	0.092	1.47 ($\pm$0.02) $\times 10^{10}$	44 ($\pm$1)	5.21	31.07	1.10	0.213
0.494	2.86×10^{-7}	0.092	1.96 ($\pm$0.02) $\times 10^{10}$	71 ($\pm$1)	5.18	31.25	1.45	0.211
0.494	3.00×10^{-7}	0.106	2.43 ($\pm$0.02) $\times 10^{10}$	89 ($\pm$1)	5.92	25.91	2.36	0.205
0.494	2.89×10^{-7}	0.092	3.15 ($\pm$0.02) $\times 10^{10}$	111 ($\pm$1)	5.24	30.79	2.39	0.225
0.494	2.90×10^{-7}	0.092	3.94 ($\pm$0.02) $\times 10^{10}$	125 ($\pm$1)	5.26	30.64	3.01	0.249
0.494	2.98×10^{-7}	0.106	4.20 ($\pm$0.02) $\times 10^{10}$	135 ($\pm$1)	5.86	26.28	4.00	0.245
0.494	2.89×10^{-7}	0.092	5.57 ($\pm$0.02) $\times 10^{10}$	152 ($\pm$1)	5.23	30.86	4.21	0.280
0.494	2.90×10^{-7}	0.092	6.17 ($\pm$0.03) $\times 10^{10}$	158 ($\pm$1)	5.26	30.64	4.71	0.287
0.494	2.99×10^{-7}	0.106	6.59 ($\pm$0.04) $\times 10^{10}$	171 ($\pm$1)	5.90	26.02	6.36	0.284
0.494	2.90×10^{-7}	0.092	8.58 ($\pm$0.06) $\times 10^{10}$	189 ($\pm$1)	5.24	30.77	6.51	0.288
0.494	2.88×10^{-7}	0.092	1.026 ($\pm$0.006) $\times 10^{11}$	208 ($\pm$1)	5.22	30.98	7.72	0.279
0.494	2.97×10^{-7}	0.106	1.242 ($\pm$0.007) $\times 10^{11}$	233 ($\pm$1)	5.85	26.41	11.75	0.266
0.494	3.00×10^{-7}	0.106	1.98 ($\pm$0.01) $\times 10^{11}$	285 ($\pm$2)	5.91	25.95	19.19	0.242
0.494	2.93×10^{-7}	0.106	3.47 ($\pm$0.03) $\times 10^{11}$	346 ($\pm$3)	5.75	27.04	31.75	0.212
0.195	2.99×10^{-7}	0.002	1.89 ($\pm$0.04) $\times 10^{11}$	296 ($\pm$6)	5.23	30.92	0.87	0.245

Γ	E	Fr	Ra	Nu	Pr	T_{mean} [°C]	ΔT [°C]	$-\partial_z \overline{T}\big\vert_{z=0.5}$
0.195	3.00×10^{-7}	0.002	3.30 ($\pm$0.04) $\times10^{11}$	346 ($\pm$4)	5.25	30.75	1.54	0.214
0.195	3.00×10^{-7}	0.002	1.14 ($\pm$0.01) $\times10^{12}$	508 ($\pm$6)	5.26	30.67	5.35	0.146
0.195	2.99×10^{-7}	0.002	3.90 ($\pm$0.03) $\times10^{12}$	756 ($\pm$6)	5.23	30.85	18.10	0.091
0.195	2.98×10^{-7}	0.002	6.53 ($\pm$0.07) $\times10^{12}$	908 ($\pm$9)	5.21	31.04	30.06	0.079
0.195	5.00×10^{-8}	0.074	1.06 ($\pm$0.04) $\times10^{11}$	51 ($\pm$3)	5.22	30.99	0.49	0.371
0.195	5.00×10^{-8}	0.074	1.49 ($\pm$0.04) $\times10^{11}$	74 ($\pm$3)	5.22	30.99	0.69	0.335
0.195	5.00×10^{-8}	0.074	2.14 ($\pm$0.04) $\times10^{11}$	115 ($\pm$2)	5.22	30.99	0.99	0.318
0.195	5.01×10^{-8}	0.074	3.29 ($\pm$0.04) $\times10^{11}$	169 ($\pm$2)	5.22	30.94	1.52	0.307
0.195	5.00×10^{-8}	0.074	5.05 ($\pm$0.04) $\times10^{11}$	227 ($\pm$2)	5.21	31.04	2.33	0.319
0.195	5.01×10^{-8}	0.074	6.37 ($\pm$0.05) $\times10^{11}$	273 ($\pm$2)	5.22	30.95	2.95	0.319
0.195	5.00×10^{-8}	0.074	8.79 ($\pm$0.06) $\times10^{11}$	331 ($\pm$2)	5.22	31.00	4.05	0.315
0.195	4.99×10^{-8}	0.074	1.11 ($\pm$0.01) $\times10^{12}$	371 ($\pm$3)	5.21	31.05	5.09	0.316
0.195	5.00×10^{-8}	0.074	1.42 ($\pm$0.01) $\times10^{12}$	418 ($\pm$3)	5.21	31.05	6.54	0.307
0.195	5.00×10^{-8}	0.074	2.23 ($\pm$0.02) $\times10^{12}$	533 ($\pm$4)	5.21	31.02	10.27	0.285
0.195	5.03×10^{-8}	0.073	4.22 ($\pm$0.02) $\times10^{12}$	696 ($\pm$4)	5.23	30.86	19.59	0.247
0.195	5.00×10^{-8}	0.074	6.93 ($\pm$0.05) $\times10^{12}$	856 ($\pm$6)	5.21	31.00	31.95	0.212
0.195	4.85×10^{-8}	0.074	8.40 ($\pm$0.08) $\times10^{12}$	904 ($\pm$8)	5.03	32.48	36.22	0.195
0.097	5.01×10^{-8}	0.005	3.47 ($\pm$0.06) $\times10^{12}$	627 ($\pm$12)	5.22	30.98	2.01	0.255
0.097	4.99×10^{-8}	0.005	8.66 ($\pm$0.05) $\times10^{12}$	871 ($\pm$6)	5.22	30.98	5.01	0.222
0.097	5.00×10^{-8}	0.005	1.73 ($\pm$0.01) $\times10^{13}$	1165 ($\pm$8)	5.22	30.98	10.00	0.158
0.097	4.98×10^{-8}	0.005	3.41 ($\pm$0.03) $\times10^{13}$	1486 ($\pm$12)	5.18	31.28	19.43	0.122

Γ	E	Fr	Ra	Nu	Pr	T_{mean} [°C]	ΔT [°C]	$-\partial_z \overline{T}\big\vert_{z=0.5}$
0.097	1.00×10^{-8}	0.115	2.26 ($\pm$0.03) $\times10^{12}$	122 ($\pm$3)	5.22	30.98	1.31	0.259
0.097	1.00×10^{-8}	0.115	3.47 ($\pm$0.03) $\times10^{12}$	218 ($\pm$5)	5.22	30.98	2.01	0.290
0.097	1.00×10^{-8}	0.115	5.20 ($\pm$0.07) $\times10^{12}$	297 ($\pm$8)	5.22	30.98	3.01	0.301
0.097	1.00×10^{-8}	0.115	7.80 ($\pm$0.12) $\times10^{12}$	421 ($\pm$5)	5.22	30.98	4.51	0.302
0.097	1.00×10^{-8}	0.115	8.66 ($\pm$0.09) $\times10^{12}$	463 ($\pm$4)	5.22	30.98	5.00	0.304
0.097	9.98×10^{-9}	0.115	1.16 ($\pm$0.03) $\times10^{13}$	546 ($\pm$5)	5.20	31.15	6.67	0.303
0.097	1.00×10^{-8}	0.115	1.73 ($\pm$0.07) $\times10^{13}$	715 ($\pm$10)	5.22	30.99	10.01	0.298
0.097	1.00×10^{-8}	0.115	3.46 ($\pm$0.02) $\times10^{13}$	1059 ($\pm$11)	5.22	30.99	20.00	0.265
0.097	1.00×10^{-8}	0.115	5.19 ($\pm$0.03) $\times10^{13}$	1316 ($\pm$15)	5.22	31.00	29.99	0.231
0.097	9.56×10^{-9}	0.115	6.80 ($\pm$0.05) $\times10^{13}$	1457 ($\pm$5)	4.95	33.20	35.60	0.224

3.3 Experimental apparatus for flow measurements[4]

Different from the heat transfer measurements, for the flow measurements we now employ a custom-made transparent acrylic cylinder section and we use $H = 2$ m exclusively for an aspect ratio $\Gamma \approx 1/5$. A picture and a sketch of the stereo-PIV arrangement are shown in Fig. 3.3. A custom-made water-filled prism around the cylinder enables optical access from outside without too much diffraction on the cylinder surface. A laser light sheet ≈ 3.5 mm thick crosses the tank horizontally at mid-height, pulsing at frequencies of 7.5 or 15 Hz; chosen according to the typical flow speeds. The water is seeded with polyamid seeding particles of nominal size 5 μm. The illuminated particle images are recorded with two cameras (Jai SP-500M-CXP2; 5 Mpixel) placed on opposite sides of the cylinder at an angle of $\approx 45°$ with the vertical. Scheimpflug adapters [65] rotate lens and image plane so that the full intersection area is imaged in focus. This stereoscopic arrangement allows for stereo-PIV evaluation [65] of all three velocity components in the light sheet plane; the resulting velocity field fits 122 vectors in the diameter at a vector separation of 3.2 mm in both horizontal directions. Here we analyse between 3000 and 9000 vector fields per experiment, a duration of $200 - 600$ s.

We have selected seven operating conditions that capture various flow subregimes. These settings are indicated in a phase diagram in Fig. 3.4 with red crosses. The mean temperature $T_{mean} = (T_{bot} + T_{top})/2$ is kept at 31 °C, i.e. $Pr = 5.2$. A constant rotation rate $\Omega = 1.9$ rad/s is applied, i.e. $E = 5 \times 10^{-8}$. For the experiments discussed here $Fr = 0.07$; at this value we could not observe significant up/down asymmetry in our sidewall temperature measurements [60] pointing at negligibly small impact of centrifugal buoyancy.

We set bottom and top temperatures such that $Ra \in \{0.11, 0.22, 0.43, 0.65, 1.1, 2.2, 4.3\} \times 10^{12}$, or, correspondingly, $Ra/Ra_C \in \{2.3, 4.7, 9.1, 14, 23, 47, 91\}$. Note that it is hard in practice to get to smaller Ra/Ra_C values in large setups like TROCONVEX, given that the small temperature differences required ($\Delta T < 0.5$ °C) cannot be controlled accurately enough at these scales (Section 3.1 and [27]). That is why we cannot enter the cellular state and only partially the CTC state. In addition, we consider one nonrotating case at $Ra = 6.5 \times 10^{11}$ for comparison.

[4] The contents of this section have been adopted from M. Madonia, A. J. Aguirre Guzmán, H. J. H. Clercx, and R. P. J. Kunnen. Velocimetry in rapidly rotating convection: Spatial correlations, flow structures and length scales. *Europhys. Lett.*, 135(5):54002, 2021 [64]; some symbols have been changed from the article to match with the current notation.

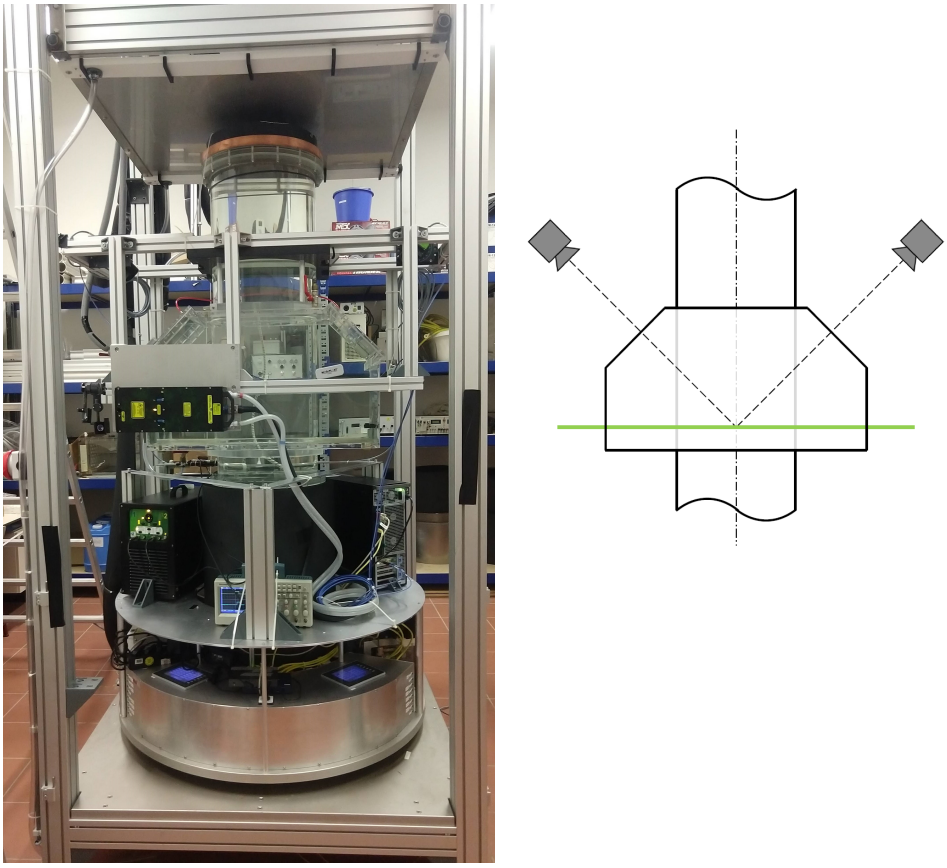

Figure 3.3: *Picture and sketch of the stereo-PIV arrangement. A water-filled acrylic prism surrounds the cylinder. The laser light sheet (green line) crosses the cylinder at mid-height. The 45° oblique planes of the prism facilitate imaging of the intersection area of the laser sheet with the cylinder using the cameras.*

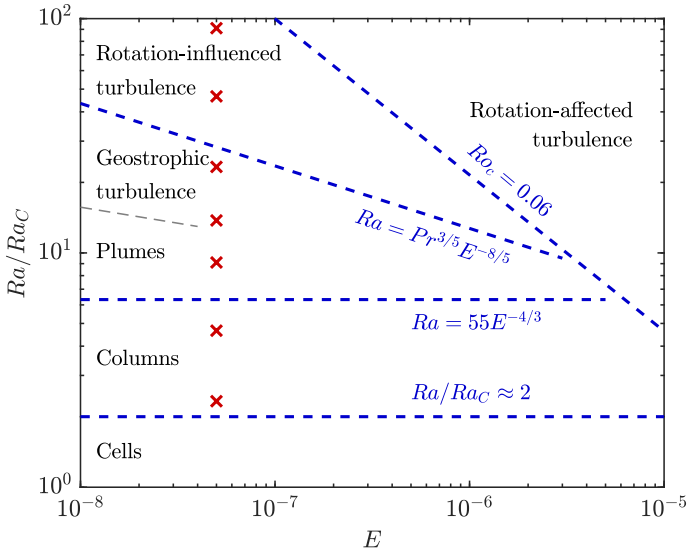

Figure 3.4: *Phase diagram for rotating convection in water. The expected flow structures and transitions between them (based on heat-flux and temperature measurements from TROCONVEX in Chapter 4) are labeled in the diagram. The velocimetry experiments discussed in this thesis are indicated with red crosses.*

Chapter 4

Heat Transfer Regimes in Rapidly Rotating Turbulent Convection[1]

In this chapter, we report heat transfer and temperature profile measurements in laboratory experiments of rapidly rotating convection in water under unprecedentedly strong rotational influence (Ekman numbers E as low as 10^{-8}). Measurements of the mid-height vertical temperature gradient connect quantitatively to predictions from numerical models of asymptotically rapidly rotating convection, separating various flow phenomenologies. Past the limit of validity of the asymptotically-reduced models, we find novel behaviors in a regime we refer to as rotationally-influenced turbulence, where rotation is important but not as dominant as in the known geostrophic turbulence regime. The temperature gradients collapse to a Rayleigh-number scaling as $Ra^{-0.2}$ in this new regime. It is bounded from above by a critical convective Rossby number $Ro_C^* = 0.06$ independent of domain aspect ratio Γ, clearly distinguishing it from well-studied rotation-affected convection.

4.1 Introduction

Convectively driven, rotationally constrained flows are the foundation of many geophysical and astrophysical processes, from dynamo action in Earth's molten iron core [66] to atmospheric patterns in gas giants [67]. These systems are massive and complex; our understanding of their flows depends on greatly simplified models. Much can be learned by distilling the physics down to the canonical problem of rotating Rayleigh-Bénard convection: a layer of fluid subject to an unstable vertical temperature gradient, rotating about a vertical axis. Even

[1] The contents of this chapter have been adopted from J. S. Cheng, M. Madonia, A. J. Aguirre Guzmán, and R. P. J. Kunnen. Laboratory exploration of heat transfer regimes in rapidly rotating turbulent convection. *Phys. Rev. Fluids*, 5(11):113501, 2020 [60], leaving out some introductory parts that have already been covered in this thesis; some symbols have been changed from the article to match with the current notation.

in this reduced problem, though, vastly different flows emerge depending on the relative strength of rotational and convective forces, whose properties must be understood before extrapolating results to geophysical settings. Though rotating convection is well-studied at moderate degrees of thermal forcing and rotation in laboratory experiments [68–71] and direct numerical simulations (DNS) [46,72], a massive parameter gap separates such studies from the extreme conditions in planets [17, 73].

Recent studies aiming to bridge this gap have employed large-scale experimental setups [35, 36, 74, 75] and high resolution simulations [32, 33, 75, 76]. Though gains may appear marginal in the planetary context, these studies have, in fact, manifested a plethora of previously unobserved behaviors. Of particular interest are regimes where both thermal forcing and rotation (described respectively by the Rayleigh number, Ra, and Ekman number, E, defined in Chapter 2) strongly affect the flow but neither dominates. Parameter estimates for planetary fluid layers indicate that understanding these regimes may be the crux to solidifying the relationship between rotating convection models and geophysical systems [18, 36]. Achieving strong enough rotational influence to establish these regimes, though, is no easy task: to date, our understanding of them relies primarily on simulations of the asymptotically-reduced equations, a set of equations rescaled in the limit of infinitely rapid rotation [31].

In this chapter, we analyze 70 new nonrotating and rotating convection experimental data points from the TROCONVEX laboratory setup [27]. Our data expand Ra by roughly a decade and reduce E by a factor of three compared to previous laboratory studies in water (and at significantly reduced influence of centrifugal acceleration), allowing us to make closer comparisons to asymptotic studies – and geophysical settings – than ever before. Using measurements of heat transfer and temperature gradients at the mid-height of the fluid layer, we demonstrate that asymptotically-predicted transitions between different flow regimes [21, 77] are quantitatively reproduced in laboratory settings. We confirm that the range of "geostrophic turbulence" (described below) expands as rotational influence increases. Our data also extend into regimes of thermal forcing stronger than is allowed by the asymptotic equations, i.e. thermal forcing is strong enough to weaken the rotational constraint. In this previously unexplored regime, we observe a novel scaling in the heat transfer and the mid-height temperature gradient, which could identify the existence of a new scaling range in between the ranges that have been studied previously. Furthermore, we observe that this new regime also becomes more and more prominent as rotation is increased (E is reduced).

4.2 Error analysis

The results presented in this chapter are based on statistics of long time series of temperature measurements. A careful error analysis is warranted to extract appropriate error intervals for the mean values, which can then be propagated to errors in the dimensionless parameters.

The errors in the Rayleigh number, $Ra = \alpha g \Delta T H^3/\nu\kappa$, and the Nusselt number, $Nu = qH/k\Delta T$, depend primarily on ΔT, T_{mean} and the error in heat flux, q. We formally propagate the errors for these quantities (e.g., Section 3.11 in [78]), and report the uncertainties in Ra and Nu in Table 3.1. For the top and bottom temperatures, the spread in temperature across different thermistors is larger than that of any single thermistor, and so the error in T_{bot} (T_{top}) is taken as the standard deviation σ across the set of all bottom (top) thermistors. The error in q is estimated as the standard deviation of the timeseries as well. Ultimately, the error bars in Nu and Ra are smaller than the marker sizes in the figures.

In contrast to the global parameters, interpretation of our laboratory results of $-\partial_z \overline{T}\big|_{z=0.5}$ requires careful error analysis. For a series of independent observations x, the standard deviation of the mean $\sigma(\overline{x}) = \sigma/N^{1/2}$ is often used to characterize the error in x. In our study, though, temperatures are maintained through PID loop controls which enforce a roughly periodic behavior on time scales of $\mathcal{O}\left(10^3\right)$ seconds. To formulate proper error estimates we employ N_{eff}, the number of observations over which measurements are 'effectively' independent [79]. This replaces N in the formulation for standard deviation of the mean [79, 80]:

$$\sigma(\overline{x}) = \frac{\sigma}{N_{\mathit{eff}}^{1/2}} \,. \tag{4.1}$$

[80] write N_{eff} in terms of elements of the autocorrelation function r_k, where:

$$N_{\mathit{eff}} = \frac{N}{1 + 2\sum_{k=1}^{N_c} \left(1 - \frac{k}{N}\right) r_k} \,. \tag{4.2}$$

The summation is truncated at the so-called limiting lag, $N_c < N - 1$. We determine the value of N_c for each temperature timeseries by finding the first transit through zero of r_k [80]:

$$N_c = \min\left\{k \middle| \left(r_k > 0 \ \wedge \ r_{k+1} < 0\right)\right\} \,. \tag{4.3}$$

In each case, the error on each time-averaged thermistor measurement is given

by (4.1). Since temperature data are horizontally averaged, $\sigma(T)$ at every height is the root-mean-square combination of σ for every thermistor at the same height. We then formally propagate errors in temperature into the normalized temperature profile following (3.1). Note that errors in not only the sidewall thermistors but also in T_{bot} and T_{top} figure into the error in $\overline{T}$.

$-\partial_z \overline{T}\big|_{z=0.5}$ is calculated as a best-fit slope for $\overline{T}$ vs. z, and so we employ the weighted least squares method to translate error bars in $\overline{T}$ into error bars in $-\partial_z \overline{T}\big|_{z=0.5}$ [78]. For a set of sidewall heights h_i, corresponding to normalized temperatures $\overline{T}_i$ with standard deviations σ_i, the weight factors are given by $w_i = 1/\sigma_i^2$. The standard deviation in $-\partial_z \overline{T}\big|_{z=0.5}$ is then written as:

$$\sigma_{\text{gradient}} = \left(\frac{\sum_i w_i}{\sum_i w_i \sum_i w_i h_i^2 - \left(\sum_i w_i h_i \right)^2} \right)^{1/2}, \tag{4.4}$$

which we interpret as the error bars for $-\partial_z \overline{T}\big|_{z=0.5}$. Errors are evidently small enough that trends in $-\partial_z \overline{T}\big|_{z=0.5}$ can be meaningfully discerned, though they may grow large as ΔT becomes small.

4.3 Results

4.3.1 Flow visualizations

We set the stage by presenting flow visualizations from the $\Gamma = 1/5$ setup (Fig. 4.1). We seed the water with neutrally buoyant rheoscopic particles [81] and illuminate with a vertical light sheet. Fig. 4.1(a,b) show the turbulent flows at high Ra and no rotation. For these cases, increasing Ra decreases the scale of flow structures. Under rotation, Fig. 4.1(c–f), the dominant flow structures evolve differently as Ra increases. In the context of asymptotic simulations where $E, Ro \to 0$ [18,21], panel (c) corresponds to "convective Taylor columns" ($Ra = 2Ra_C$) where narrow structures span the tank vertically, panel (d) to "convective plumes" ($Ra = 18Ra_C$) where the columns interact laterally and become wavy, and panel (e) to "geostrophic turbulence (GT)" ($Ra = 34Ra_C$), where convective forces have destroyed the columnar structure but flows remain constrained to rotational length scales. Asymptotic simulations display the transition between columns and plumes at [77]:

$$Ra = 55E^{-4/3} = 6.3Ra_C\,. \tag{4.5}$$

No such prediction can be made with sufficient confidence for the plumes to GT transition, however: for low E ($\lesssim 10^{-6}$), GT exists at the limit of accessibility for asymptotic simulations and DNS. It remains largely uncharacterized at $Pr \neq 1$ and with poorly constrained scaling properties even at $Pr = 1$ [21, 32, 33, 35].

The onset horizontal scale λ_C – believed to accurately describe flows in Fig. 4.1(c–e) – serves as a necessary condition for deriving the asymptotically-reduced equations [31]. This assumption persists until buoyancy takes over the horizontal length scale, theorized to occur at [37, 82]:

$$Ra \sim E^{-8/5} Pr^{3/5} . \tag{4.6}$$

Fig. 4.1(f) ($Ra = 70 Ra_C$) lies beyond this upper bound, demonstrating different flow morphology. Flows at $Ro \lesssim 1$ are well-studied at moderate E, but their properties change fundamentally as E decreases: for example, Nu overshoots above the non-rotational heat transfer efficiency ($Nu_0(Ra)$) in this range for $E \gtrsim 10^{-6}$ [29, 71], but becomes suppressed below Nu_0 as E is lowered [36]. Our laboratory experiment is uniquely well-suited to exploring high Ra/Ra_C values at simultaneously low E [27], offering significantly lower E than other setups while achieving higher Ra/Ra_C than is possible in simulations using the asymptotically reduced equations.

4.3.2 Heat transfer

Before considering rotating convection at extreme parameters, we consider non-rotating turbulent heat transfer for validations. Fig. 4.2 shows our nonrotating data in terms of Nu versus Ra. We achieve a maximum $Ra = 7 \times 10^{13}$ – nearly a decade higher than any previous $Pr > 1$ study (e.g. [36]). Nonrotating data [Fig. 4.2(a)] follow a best-fit scaling

$$Nu_0 = 0.11 \left(^{+0.02}_{-0.01}\right) Ra^{0.308 \pm 0.005} , \tag{4.7}$$

agreeing with previous scaling exponents $\sim 0.3 - 0.33$ found in water [36, 83, 84] and other fluids [41, 85, 86]. They are also consistent with the classical prediction $Nu \sim Ra^{1/3}$ where the bulk is sufficiently turbulent as to be approximately isothermal, with the temperature gradient confined to the upper and lower thermal boundary layers [87]. There is no evidence of transition to a steeper scaling that would indicate 'ultimate' convection; the state of convection where the boundary layers have become turbulent [30, 88] with more efficient heat transfer evident from a steeper scaling exponent $\gamma > 1/3$ in the scaling relation $Nu \sim Ra^{\gamma}$. The transition location $Ra \sim 10^{11}$–10^{13} where ultimate convection sets in is disputed [89, 90]. Note that our comparatively narrow geometry

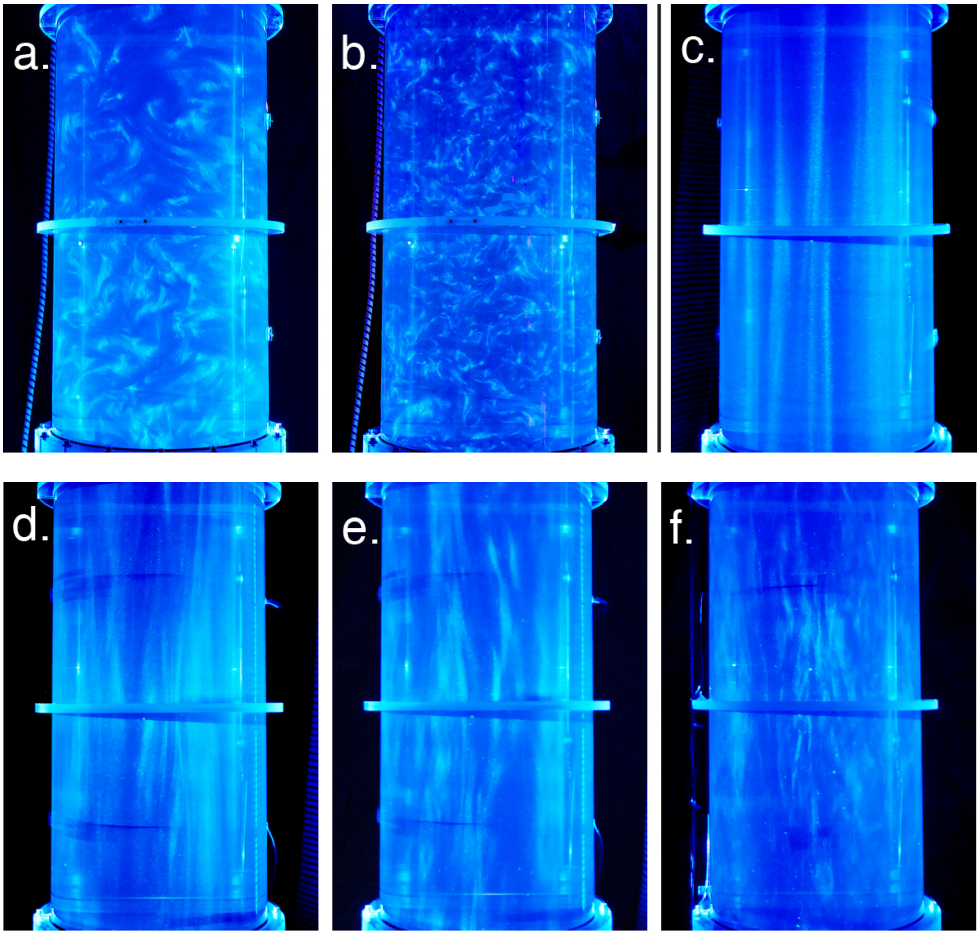

Figure 4.1: *Flow field visualizations in a vertical slice of the* $\Gamma = D/H = 1/5$ *tank. Panels (a,b): nonrotating convection at* $Ra =$ *(a)* 1.4×10^{11}*, (b)* 2.2×10^{12}*. Panels (c–f): rotating convection at* $E = 5 \times 10^{-8}$ *and* $Ra =$ *(c)* 9.6×10^{10} *(convective Taylor columns), (d)* 8.6×10^{11} *(plumes), (e)* 1.2×10^{12} *(geostrophic turbulence), (f)* 3.3×10^{12} *(rotationally-influenced turbulence). The vertical black line remarks the separation between non-rotating and rotating cases on the first row.*

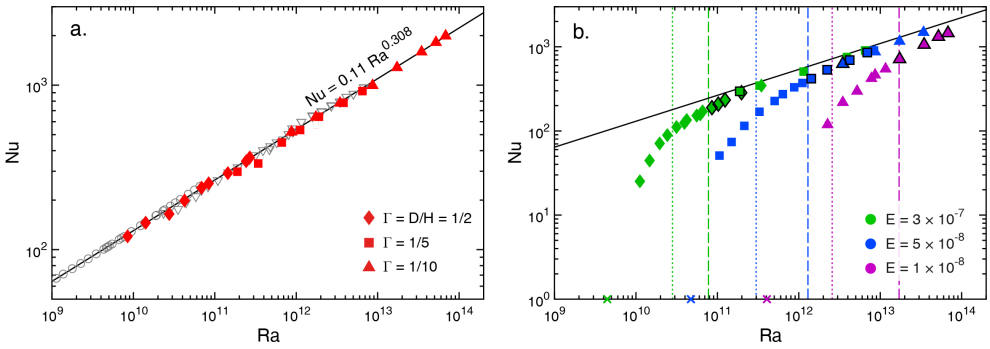

Figure 4.2: *Nusselt number (Nu) plotted versus Rayleigh number (Ra) for (a) nonrotating and (b) rotating convection experiments. In both panels, marker shape represents tank aspect ratio Γ; the solid line our nonrotating convection fit (4.7). Data from previous studies are included as open grey circles [92] and triangles [36]. In panel (b), color represents Ekman number (E), Ra_C in each case is marked by '×,' and black-outlined symbols are within our new postulated scaling range (to be precisely defined later). Dotted lines represent the columns–plumes transition (4.5) from [77]; dashed lines represent the transition (4.6) where the asymptotically reduced equations are projected to break down, it is the flow transition from GT to the postulated new scaling range.*

($\Gamma = 1/10$) is possibly detrimental to the transition to ultimate convection; from recent numerical simulations in a similar geometry [91] no transition could be observed either.

We now present our heat transfer data of rotating convection as $Nu(Ra)$ graphs at three different Ekman numbers, $E = 10^{-8}, 5\times10^{-8}$ and 3×10^{-7}. Each curve [Fig. 4.2(b)] follows a characteristic succession of ever shallower slopes as Ra increases (as postulated in [27]), eventually merging with the nonrotating scaling (4.7). As is characteristic for low E, rotational Nu values lie below the nonrotating Nu_0 values until well beyond onset. This separation becomes more pronounced as E decreases: the $E = 3 \times 10^{-7}$ trend first comes within 10% of the nonrotating trend at $Ra \approx 40Ra_C$, while for $E = 5 \times 10^{-8}$ this does not occur until $Ra \approx 400Ra_C$. This confirms that the so-called geostrophic regime of rotation-dominated convection, with its reported subdomains as cells, columns, plumes and GT, expands as E is lowered.

It is technically difficult to connect our lowermost experimental data point at $Ra = 1.12 \times 10^{10}$, $E = 3 \times 10^{-7}$ to the onset of convection (green '×' on the horizontal axis); the minute temperature differences required cannot be stably maintained [27, 75]. But it is clear that a steep $Nu(Ra)$ scaling in the cellular and columnar regimes is required. This picture is consistent with direct numerical simulation (DNS) studies at low E and $Pr \simeq 3$–10 [32, 36, 75] that do observe steep $Nu(Ra)$ scaling. However, there is an important difference

in domain composition: these studies typically use rectilinear domains with periodic boundary conditions in the horizontal directions rather than a cylinder. Recent simulations and experiments have indicated the persistent presence of so-called wall modes in confined rotating convection [38, 93–95]: a sidewall recirculation (absent in periodic DNS domains) leading to increased Nu, the effect more pronounced at lower Ra/Ra_C [38]. These complicate quantitative comparison of heat flux between experiment and DNS.

It is anticipated that the different regimes of flow phenomenology can be recognized as specific power-law scaling ranges with characteristic scaling exponents [27]. Here we illustrate that the $Nu(Ra)$ scaling alone does not provide conclusive evidence for regime transitions in Fig. 4.3, where Nu is compensated by the nonrotating Nu_0 fit (4.7), and Ra is compensated by several transition arguments. In contrast to previous studies [35, 36], none of these arguments definitively collapse data across multiple E values in our extreme parameter range. Compensating Ra by (4.5) gives little evidence of collapse [Fig. 4.3(a)]. Compensating with (4.6) collapses the near-onset trends while inducing spread in the GT range [Fig. 4.3(b)]; compensating by Ro_C does the opposite [Fig. 4.3(c)]. In the latter panel there is satisfactory collapse of our higher Ro_C data, with a clear transition at $Ro_C^* = 0.06$ [see inset in Fig. 4.3(c)] that is independent of aspect ratio Γ.

We argue that $Ro_C^* = 0.06$ could mark the upper boundary of a new scaling range. The transition point is significantly distinct from the well-documented transition from rotation-affected to nonrotating convection [96]: the latter transition has been shown to be strongly dependent on Γ and the predicted Ro_C^T ($Ro_C^T = \{1.2, 0.40, 0.16\}$ for $\Gamma = \{1/2, 1/5, 1/10\}$, respectively) is significantly higher than $Ro_C^* = 0.06$ [see inset in Fig. 4.3(c)]. Thus, we anticipate that for $Ro_C^* < Ro_C < Ro_C^T$ we have recovered rotation-affected convection where rotation does not significantly affect the heat transfer scaling; the data points approach the nonrotating $Nu(Ra)$ curve as Ra increases. We note that a qualitatively similar collapse is found in [35], but at a significantly higher transition value $Ro_C^* = 0.35$. The most prominent difference is the working fluid and associated Prandtl number; Ecke & Niemela [35] used low-temperature helium with $Pr = 0.7$ while we use water at $Pr = 5.2$.

We shall argue in Sec. 4.3.3 that the lower boundary of the new scaling range is given by Eq. (4.6): $Ra \geq E^{-8/5}Pr^{3/5}$. An indicative fit of heat transfer in the new regime results in $Nu/Nu_0 \sim Ro_C^{0.39}$ or $Nu \sim Ra^{0.52}$ ($Nu \sim Ra^{\gamma^*}$ with $\gamma^* = 0.52$).

Additionally, we can consider heat transfer in the regimes characterized by plumes and geostrophic turbulence, the range between dotted and dashed

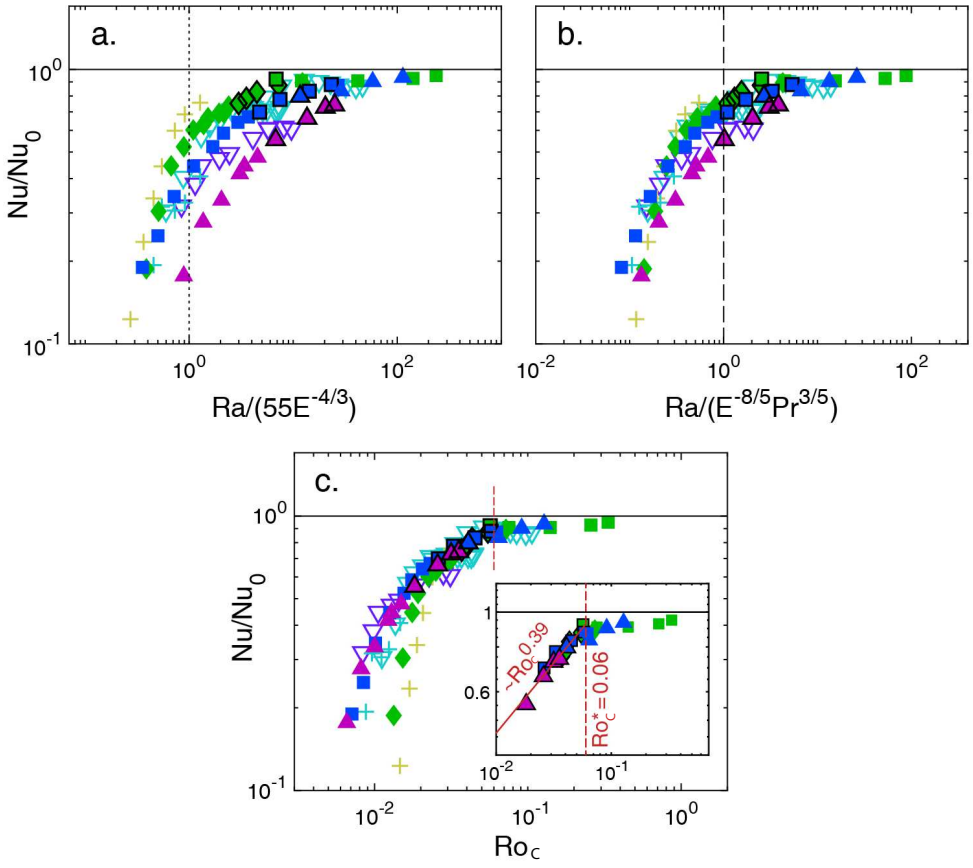

Figure 4.3: *Nu compensated by nonrotating scaling Nu_0 as per Eq. (4.7) versus: (a) $Ra/(55E^{-4/3})$ as per Eq. (4.5) [77]; (b) $Ra/(E^{-8/5}Pr^{3/5}) = Ra/(2.7E^{-8/5})$ as per Eq. (4.6) [37], and (c) Ro_C [45]. Bullet color and shape are the same as in Fig. 4.2, with additional points from [36]: numerical $E = 1 \times 10^{-6}$ cases are yellow crosses, numerical $E = 1 \times 10^{-7}$ cases are cyan crosses, lab $E \simeq 10^{-7}$ cases are empty cyan triangles, and lab $E \simeq 3 \times 10^{-8}$ cases are empty indigo triangles. The inset in panel (c) shows our rotating data for which $Ra > E^{-8/5}Pr^{3/5}$; see also Eq. (4.6). A change in slope occurs at $Ro_C^* \approx 0.06$, which we argue is the upper limit of the new scaling range.*

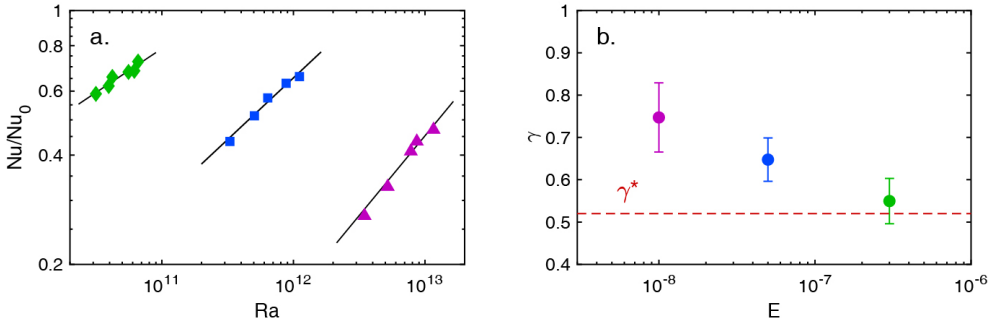

Figure 4.4: *(a) Zoomed-in view of the Nu data points of Fig. 4.2(b) in the plumes/GT range, plotted as Nu/Nu_0 as a function of Ra for clarity. Weighted least-squares power-law fits are included with solid black lines. Bullet color and shape as in Fig. 4.2. (b) Corresponding $Nu(Ra)$ scaling exponents γ as a function of E. The error bars indicate one standard deviation error intervals resulting from the weighted least-squares fits. The red dashed line indicates $\gamma^* = 0.52$, the previously discussed scaling exponent of the new scaling range beyond the GT regime.*

vertical lines in Fig. 4.2(b). These datapoints also display an approximate power-law scaling $Nu \sim Ra^{\gamma}$; the scaling exponent γ is generally larger than for the previously discussed new scaling range and shows a clear dependence on E. A close-up view of the data points in this range is plotted in Fig. 4.4(a), where we plot Nu/Nu_0 as a function of Ra to have the points lie closer together. Solid black lines are weighted least-squares power-law fits. Fig. 4.4(b) presents the corresponding scaling exponents γ as a function of E. Though the range is not extensive, it is clear that steeper scaling is observed for smaller E. This is again in line with the projected succession of scaling ranges with descriptive exponents per flow state [27]. Compared to the reported asymptotic scaling $\gamma = 1.5$ for geostrophic turbulence [37] our exponents are small, but increasing as E is reduced.

4.3.3 Mid-height temperature gradient

In lieu of further transition information from globally-averaged parameters, we shift focus to the time-averaged vertical temperature gradient $-\partial_z \overline{T}\big|_{z=0.5}$. In nonrotating turbulent convection, the temperature profile is sharply divided between the bulk, which is nearly isothermal ($-\partial_z \overline{T} \approx 0$), and the thermal boundary layers, within which nearly all of the temperature drop ΔT occurs [30, 97]. In rotating convection, however, the shape of the temperature profile evolves as Ra/Ra_C changes and with it the flow morphology, giving it diagnostic properties [21,33,77,98]. The aforementioned wall modes of confined convection

[38, 93, 94] actually do not affect long-time averaged temperature values; their symmetrical structure (azimuthal distribution into a 'colder' and a 'warmer' half) and gradual azimuthal precession [38] make it so that the wall mode signature can be nicely averaged out in the sidewall thermistor time series. Hence the time-averaged sidewall gradient still nicely follows that of the bulk, independent of the presence of the wall mode.

We want to make a remark on the error bars. The error in $-\partial_z\overline{T}\big|_{z=0.5}$, obtained with the procedure detailed in Section 4.2 can be seen to increase towards small values of Ra/Ra_C. This is mainly due to the smaller ΔT values used there with correspondingly larger relative error; ΔT is used for normalization in $-\partial_z\overline{T}\big|_{z=0.5}$. Furthermore, the error also grows towards small values of $-\partial_z\overline{T}\big|_{z=0.5}$ that are found at the largest Ra/Ra_C values. There, the temperature difference over the bulk reduces with larger relative error as a result.

Fig. 4.5(a–c) show that the temperature gradient measured at mid-height, $-\partial_z\overline{T}\big|_{z=0.5}$, is indeed a robust tool for determining regime transitions at each E value. Remarkably, the transitions found in asymptotic simulations show excellent quantitative agreement with the transitions we observe in our measured $-\partial_z\overline{T}\big|_{z=0.5}$, regardless of differences in domain composition and boundary conditions. In the cellular and columnar regimes, increasing Ra leads to a decreasing temperature gradient. At the transition point described by Eq. (4.5) this trend reverses, indicating that increasing Ra/Ra_C now forces more of the temperature gradient into the interior as the horizontal rigidity of bulk flow structures relaxes. Visualizations of the flow and $Nu(Ra)$ data do not reveal where the plumes–GT regime transition takes place, but asymptotic studies posit that GT corresponds to $-\partial_z\overline{T}\big|_{z=0.5}$ flattening with increasing Ra/Ra_C [21]. Our results do appear to manifest such a flattening at $Ra/Ra_C \simeq 15$ at each E value. This abruptly gives way to a decreasing trend at the transition point described by Eq. (4.6), which could be considered the lower boundary of the new scaling regime that we postulate. A factor $E^{-4/15}$ separates Eqs. (4.6) and (4.5), identifying that the parameter range of GT expands as E decreases toward geophysical values.

In Fig. 4.5(d) we plot $-\partial_z\overline{T}\big|_{z=0.5}$ data for all E values versus Ra rescaled by (4.6) using 1 as prefactor. Overplotting separate E trends collapses all data in this regime into an approximate $-\partial_z\overline{T}\big|_{z=0.5} \sim Ra^{-0.21}$ scaling, in sharp contrast to the Ra^0 scaling reported for the traditional rotationally-affected regime (see Table 2 of Ref. [99], the authors labeled it the 'weakly rotating' regime). We thus postulate Eq. (4.6) as the lower bound of a novel scaling range that displays temperature statistics different from previously identified scaling ranges: both "rotationally-affected convection" and GT. Data points belonging

to the new scaling range are marked by black outlines in Figs. 4.2–4.5. The scaling exponent of $-\partial_z \overline{T}\big|_{z=0.5}$ in this range is a novel result that we cannot currently explain. We speculate that nonrotating-style thermal boundary layers have formed beyond this transition, such that increasing Ra causes stronger mixing in the bulk and isolates more of the temperature gradient into the boundary layers.

In the following chapters we use flow measurements, in particular stereoscopic particle image velocimetry, to get more insight into the flow statistics in the different flow regimes and in particular to formulate a better understanding of the flow in the proposed new RIT scaling range. Our companion numerical study, performed in a laterally unbounded domain, retains similar results for both heat transfer and temperature gradient measurements in the RIT regime [100].

4.4 Conclusion

Our novel rotating convection survey demonstrates the emergence of several distinct regimes as E is pushed lower than any previous study in water. Scalings between Nu and Ra show consistency with previous results at moderate parameter values while extending them to more extreme values. To determine precise transition locations, the mid-height temperature gradient $-\partial_z \overline{T}\big|_{z=0.5}$ serves as a robust tool: transitions almost invisible in $Nu(Ra)$ plots [Figs. 4.2 & 4.3] are expressed as pronounced changes in the $-\partial_z \overline{T}\big|_{z=0.5}$ vs. Ra/Ra_C trend [Fig. 4.5]. Our data confirm that the GT range expands as E decreases. They also suggest the existence of an additional, previously unidentified scaling regime just beyond GT, for $Ra > E^{-8/5}Pr^{3/5}$ and $Ro_C < Ro_C^* = 0.06$ (Fig. 4.3). The new range displays behaviors differentiating it from both the GT regime at asymptotically small E [21] and the rotationally-affected regime at moderately large E [29, 71]: temperature gradients collapse as $-\partial_z \overline{T}\big|_{z=0.5} \sim Ra^{-0.21}$ (Fig. 4.5d) and heat flux as $Nu/Nu_0 \sim Ro_C^{0.39}$ (Fig. 4.3c). In the regime of plumes and GT, we observe that the heat flux scaling is generally steeper than that, with increasing exponent as E is reduced. Furthermore, we show that the mid-height temperature gradient can be used to identify regime transitions in remarkable quantitative agreement with transition predictions from asymptotic simulations, despite different domain composition and boundary conditions.

These results show that the parameter space of turbulent convection, from nonrotating to asymptotically rapid rotation, may show an even richer subdivision than known so far. We argue that there are signs of a new intermediate regime separating "rotationally-dominated" convection (GT) from traditional

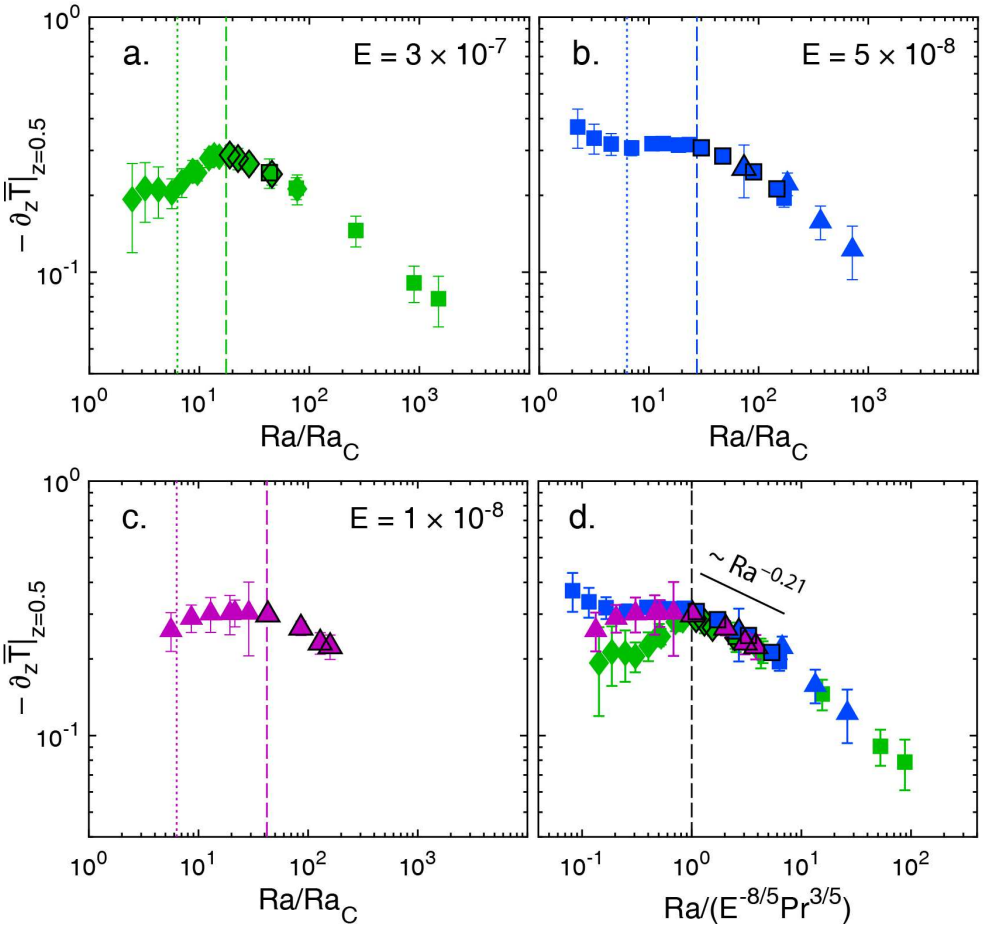

Figure 4.5: *Normalized mid-height temperature gradient* $-\partial_z \overline{T}\big|_{z=0.5}$ *versus* Ra/Ra_C *for (a)* $E = 3 \times 10^{-7}$*, (b)* $E = 5 \times 10^{-8}$*, and (c)* $E = 1 \times 10^{-8}$*. Symbol shapes represent* Γ *as in Fig. 4.2. Dotted lines represent Eq. (4.5); dashed lines Eq. (4.6). (d) Normalized gradient* $-\partial_z \overline{T}\big|_{z=0.5}$ *versus* $Ra/(E^{-8/5}Pr^{3/5}) = Ra/(2.7E^{-8/5})$ *as per Eq. (4.6), for all three E values. A fit to the black-bordered points (those lying in the new scaling range) across all E values gives* $-\partial_z \overline{T}\big|_{z=0.5} \sim Ra^{-0.21}$*.*

"rotation-affected convection". Extrapolating the scaling arguments supported in this chapter, the spaces between transitions widen as E decreases: the plumes / GT range expands as $Ra \sim E^{-4/15}$ while the proposed new scaling range expands as $Ra \sim E^{-2/5}$. In the geophysical context, estimates for planetary fluid layers give $E \sim 10^{-19} - 10^{-12}$ [17] and $Ra/Ra_C \sim 10^2 - 10^3$ [101]. Rotating convection in these layers then invariably inhabits either geostrophic turbulence or turbulence exhibiting the new scaling. Large-scale laboratory experiments can aid to bridge the gap between asymptotic studies and direct numerical simulations, while at the same time exploring the parameter space currently out of reach for both simulation approaches.

Chapter 5

Flow Statistics

In this chapter, we give an overview of different flow statistics of rotating Rayleigh–Bénard convection from stereo-PIV measurements, in a parameter range that has never been analyzed before. Our investigation focuses on seven rotating cases and a non-rotating one for comparison. We present mean flow fields in which we compensate for the azimuthal drift of the sidewall circulation that show the division into an outer part composed by two lobes of oppositely-signed vertical velocity and an inner part characterized by a quadrupolar vortex. Radial profiles of root-mean-square velocities and vertical vorticity show an increase of overall magnitude with higher thermal forcing, as well as increasing thickness of the sidewall boundary layer. The velocity fluctuations in the bulk flow show a scaling that is in between visco-Archimedean-Coriolis and Coriolis-inertial-Archimedean force balance arguments. The vorticity scaling follows that of the velocity fluctuations. The rotating cases exhibit also a velocity distribution that is nearly isotropic, in contrast with the non-rotating case which has a clear preference for the vertical components.

5.1 Introduction

In Chapter 4 we have used temperature measurements to investigate the different states of rotating Rayleigh-Bénard convection based on two different quantities, the Nusselt number and the midheight vertical temperature gradient. From this chapter on, we analyze data obtained from velocity measurements. As described in Section 3.3 we have performed stereo-PIV measurements of rotating RBC at different buoyancy forcing strengths and one non-rotating case as benchmark.

Velocity measurements can be used to characterize in further details the different behaviors of the states of rotating Rayleigh–Bénard convection. With this investigation, we can gain more insights into these states as well as the novel state of RIT, described in Chapter 4. With flow measurements, we have a new tool to try and distinguish RIT from the rotation-affected state.

In previous literature, alongside numerical simulations [21, 23, 32, 34, 77, 93, 102–104], flow velocities of rotating Rayleigh–Bénard convection have been measured in experimental setups [24, 105–108], with analysis that focused on different characteristics of rotating Rayleigh–Bénard convection.

From previous studies [38, 93, 94] we know that a secondary flow, the sidewall circulation, sets in in laterally confined domains (such as cylinders). This generates a boundary circulation that modifies the general heat transfer properties of the system. Moreover, the overall flow in a cylindrical domain precesses anticyclonically with a specific angular velocity. This drift changes with the different parameters of the flow; specifically, Ref. [38] connects the angular velocity with the Rayleigh number, while Ref. [93] relates it also to Pr, E and the aspect ratio.

In rotating Rayleigh–Bénard convection, there are many predictions of root-mean-square (RMS) velocity scalings depending on which force balance is at play [23, 99, 109]. The visco-Archimedean-Coriolis (VAC) balance assumes that the Taylor-Proudmann (TP) constraint (see Eq. (2.36)) is broken by viscous forces, while the Coriolis-inertial-Archimedean (CIA) balance assumes that the TP constraint is broken by inertia. Velocity measurements at low E can give a hint on which balance is present in experiments at extreme parameters, where the VAC balance predicts velocity fluctuations to scale as $u^{RMS} \sim Ra^{1/2}E^{1/3}(Nu-1)^{1/2}/Pr$ and CIA balance instead predicts $u^{RMS} \sim Ra^{2/5}E^{1/5}(Nu-1)^{2/5}/Pr^{4/5}$.

The distribution of such RMS velocities (horizontal vs. vertical) can also be a tool to identify the flow states of rotating Rayleigh–Bénard convection [24, 70, 105, 107].

In this chapter we analyze a subset of the cases treated in Chapter 4, all taken with a tank height of 2 m, composed by seven cases of rotating Rayleigh–Bénard convection at constant rotation rate ($E = 5 \times 10^{-8}$) with varying temperature differences ($Ra = \{0.108, 0.216, 0.432, 0.648, 1.08, 2.16, 4.32\} \times 10^{12}$) and one case of Rayleigh–Bénard convection with $Ra = 6.48 \times 10^{11}$ for comparison.

Velocities, with stereo-PIV, are measured in cartesian components (u_x, u_y, u_z), but we choose to express them in terms of cylindrical components (u_r, u_θ, u_z) given the cylindrical flow domain domain, that makes the latter more intuitive and appropriate to use.

In this chapter we express the results in a dimensionless form by scaling with viscous units $U_\nu = \nu/H$ and $\tau_\nu = H^2/\nu$ for a natural comparison of cases at different Rayleigh number (see also Section 2.2).

The remainder of the chapter is structured as follows. In Section 5.2 we show how we calculate the precession speed of the sidewall circulation and the

averaged flow fields taking into account this drift. In Section 5.3 we present radial profiles of RMS velocities and vertical vorticity of our selected cases. In Section 5.4 we plot the different definitions of sidewall boundary layer size and see how they compare to predictions. In Section 5.5 we focus on the RMS velocities and vorticities in the inner part of our domain, comparing our findings with velocity scalings hypothesized in previous research, and see how much the cases deviate from the isotropic distribution of velocities. Finally, in Section 5.6 we present our conclusions.

5.2 Precession averaged fields

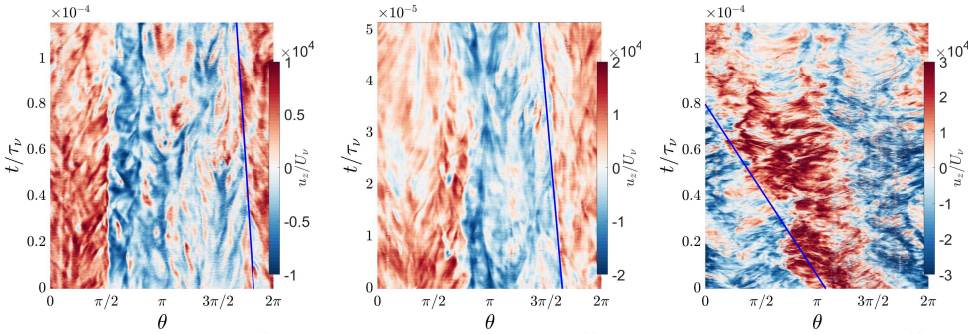

(a) $Ra = 2.16 \times 10^{11}$ **(b)** $Ra = 6.48 \times 10^{11}$ **(c)** $Ra = 2.16 \times 10^{12}$

Figure 5.1: *Time-angle plots of vertical velocity at constant $E = 5 \times 10^{-8}$ for different Ra. Velocity is normalized by the viscous velocity $U_\nu = \nu/H$, time is normalized using the viscous time $\tau_\nu = H/U_\nu$. The blue line indicates the precession as predicted from Eq. (5.1)*

In order to study the mean flow pattern set up by the interplay of bulk and sidewall circulation [38], it is worthwhile to take into account the precession speed ω_{prec} induced by the drift of the sidewall circulation. Failing to do so may result in canceling some of the features of the pattern that emerge in RRBC in a cylinder. To track the orientation of the sidewall circulation, we define a circle of 200 equally spaced points close to the sidewall and we observe the evolution in time of the vertical velocity: from our prior work [38], the two lobes of the sidewall circulation are most easily identified from this quantity. The radial position of these points is initially chosen from an estimate of the thickness of the sidewall circulation, and then adjusted to give the clearest data. The velocity in these points is estimated through bilinear interpolation from the 4 nearest data points. We plot the vertical velocity values in these points with their angular position on the horizontal axis and time on the vertical axis,

obtaining a time-angle plot. We normalize the time with the viscous time unit $\tau_\nu = H/U_\nu = H^2/\nu$ (with $U_\nu = \nu/H$ as defined in Eq. (2.20)). In Fig. 5.1 we can see the temporal evolution of the sidewall circulation and evaluate the precession speed ω_{prec}: the division into two lobes is clear, as is the clockwise drift. We can also observe some turbulent interruptions of this trend where the precession has some disturbance, as seen also in [102]. A line can be drawn along the interface between blue and red. This line indicates the precession of the sidewall circulation. Over time, it precesses anticyclonically, i.e. against the direction of rotation of the cylinder. The slope of the line is ω_{prec}. As it can be seen from the pictures and as expected from literature [38, 102] ω_{prec} increases with Ra. Also, we found great agreement with our data and the precession rate found from [102],

$$\omega_{prec}/\Omega = 0.03\Gamma^0 Pr^{4/3} Ra E^{5/3} \tag{5.1}$$

represented by the line in the figure that nicely follows the division of the lobes. The estimate from [38] does not match our data. That study used a different and constant value of $E = 10^{-7}$. It is clear from Eq. (5.1) that ω_{prec} is strongly dependent on E. We use the angular speed (5.1) determined by Zhang et al. [102] when we apply orientation-compensated averaging. For the low Ra cases, since the precession is slower and we have a shallower slope, it is a bit harder to see a clear precession from the figure, but the precession averaged plots in Fig. 5.2 show that we do capture the right angular speed of the structures.

As we set ω_{prec} we can analyze orientation compensated fields. For each time step, we rotate the flow field by the angle required to put the two lobes in their original position. This method allows us to find the mean field structures of the flow throughout the cross-sectional plane. Fig. 5.2 shows the precession averaged fields of the vertical, radial and azimuthal velocities for three RRBC cases at different Ra and one non-rotating RBC case. The results show great similarities with the same procedure applied to simulation results [38]. For the rotating cases the two lobes of oppositely signed velocities attached to the sidewall are clearly seen from the vertical velocity plots. We also see their thickness increase with increasing Ra. This relation is going to be further analyzed in Section 5.3. This phenomenon of the sidewall circulation, investigated in literature before, using direct numerical simulations [38, 93] and experimentally through temperature measurements [38, 110] is now, for the first time, seen in experimental velocity measurements. We can also see a secondary inner layer of oppositely signed lobes, although less prominent. These secondary structures are more defined and localized for lower Ra, while they become more diffuse at higher temperature differences, blending in with the bulk flow as it becomes more turbulent.

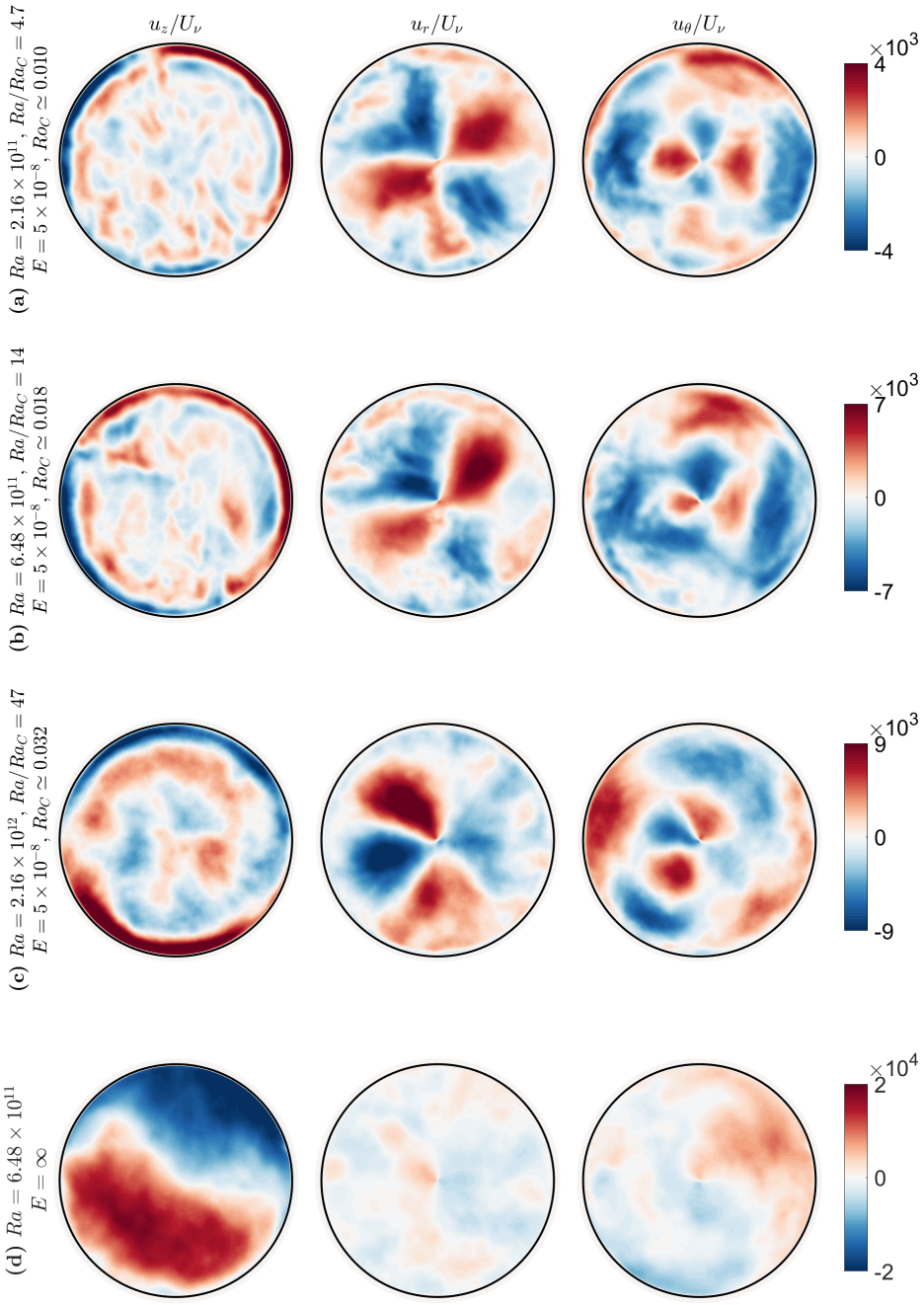

Figure 5.2: *Precession averaged fields of the vertical, radial and azimuthal velocities for different Ra. Velocity is normalized by the viscous velocity $U_\nu = \nu/H$.*

One caveat should be taken into account: these measurements are done in a section of the cylinder that was not as well insulated as it is for heat transfer measurements (see Chapter 4) and some heat might be leaking through the sides, an occurrence that is also not considered in simulations with adiabatic sidewalls. This might explain some of the irregularities and asymmetries of the sidewall circulation pattern for vertical velocity.

From the radial velocity plots, we can immediately identify a four quadrant division: there is flow entering the bulk of the cylinder from the position where the two lobes of the sidewall circulation meet. This inward flow is compensated by a radially outward flow perpendicular to these intrusions. These inward jets may be the main cause of the absence of a clear quasi-steady vortex grid that is generally expected at lower Ra, where the bulk flow should be characterized by convective Taylor columns [21, 111]. Averaged azimuthal velocity fields complete the picture, showing also clear similarities with [38]. The bulk zone is also divided into quadrants of oppositely signed velocities. Wherever the azimuthal velocity displays a maximum, the radial velocity is zero, suggesting a quadrupolar state where four vortices fill the cylinder section. This flow state is analyzed in more detail in Chapters 6 and 7 of this thesis.

The non-rotating case in Fig. 5.2(d) shows a clear division into two halves of oppositely signed vertical velocity, a clear signal of the large-scale circulation of RBC [30].

5.3 Azimuthally averaged statistics

In Section 5.2 we have averaged the velocity fields over time taking into account the precession speed of the sidewall circulation. We can clearly see the division between a bulk area and a sidewall zone from the plot of the vertical velocity and a hint of a general circulation in the inner part. Another way of analyzing this separation is to see how quantities behave if we also average azimuthally. Here we consider the radial dependency of different quantities, after averaging with respect to time and azimuthal angle. For our binning procedure, we divide the section in 65 concentric circular shells, so each shell would represent a ring of thickness 3 mm comparable to the resolution of our PIV vector field spacing (3.2 mm). We first analyze the root-mean-square (RMS) value of the vertical velocity fluctuations defined as $u_z^{RMS} \equiv \sqrt{\langle u_z^2 \rangle - \langle u_z \rangle^2}$, where $\langle \cdot \rangle$ denotes angle- and time-averaging. This quantity is chosen to highlight the radially dependent behavior that emerges from the fluctuations around the mean value. We compare this quantity with the horizontal RMS velocity defined as $u_{hor}^{RMS} \equiv \sqrt{\langle u_x^2 \rangle + \langle u_y^2 \rangle}$ where we assumed the mean of horizontal velocity to tend to zero.

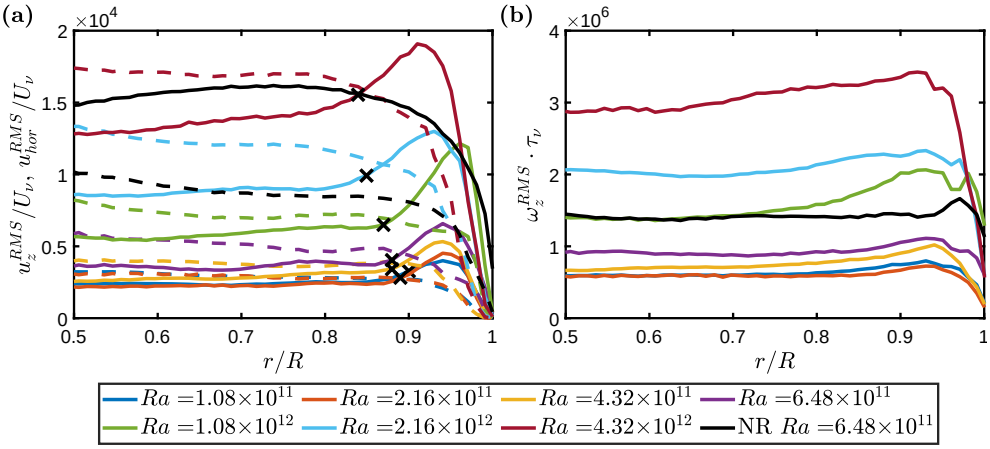

Figure 5.3: *(a) Radial dependence of u_z^{RMS} (solid lines) and u_{hor}^{RMS} (dashed lines) for different Ra, normalized by the characteristic velocity scale $U_\nu = \nu/H$. Black crosses indicate the beginning of the sidewall boundary layer following Eq. (5.2). (b) Radial dependence of ω_z^{RMS} at mid-height for different Ra, normalized using the viscous time scale $\tau_\nu = H^2/\nu$. All the quantities displayed in Fig. 5.3 are shown from half the cylinder radius onward for clarity.*

In Fig. 5.3(a) we plot them, normalized by the characteristic velocity scale U_ν, that can be interpreted as a Reynolds number $Re = u^{RMS}/U_\nu = u^{RMS}H/\nu$, see Eq. (2.24). Both quantities show an overall trend of larger values for larger Ra, as expected, with the exception of the two lowest Ra cases that are almost identical. We believe this behavior is due to the fact that for low thermal forcing the overall dynamics is dominated by the sidewall circulation and its jets impinging into the bulk. This results in smaller changes in vertical velocity, while for higher Ra the inner turbulent flow is of higher significance. The distinction between the inner and outer portions of the domain is clear from both quantities: the RMS vertical velocity and RMS horizontal velocity profiles both suggest a generally constant value that is independent of the radial position for the bulk part, away from the lateral sidewall, and a change of behavior close to this sidewall. Close to the sidewall we see an increase in u_z^{RMS}, where the sidewall circulation sets in. The black crosses in Fig. 5.3(a) indicate the thickness of the sidewall boundary following the equation

$$\delta_{u_{z,min}^{RMS}}/R = ARa^{0.15\pm0.02}\,, \tag{5.2}$$

where $A = (3 \pm 1) \times 10^{-3}$ is found in Ref. [38]. Here we use $A = 2 \times 10^{-3}$ as a prefactor and 0.15 as the exponent for Ra. This will be better explained in Section 5.4. This definition agrees well with our data as it indicates the start of the change in behavior of velocities, for both u_z^{RMS} and u_{hor}^{RMS}, where for the latter we see the beginning of the decay to zero, instead of a growth into a maximum close to the sidewall.

The non-rotating case (black curve in Fig. 5.3(a)) shows three main points of interest:

1. a different trend, with a decay to zero close to the sidewall without any previous increase,
2. much higher values of vertical velocity compared to the rotating case with the same Ra (see black and purple curves in Fig. 5.3(a)), a clear indication that heavy influence of rotation makes the flow less turbulent, suppressing both vertical and horizontal RMS velocities,
3. a more pronounced difference between vertical and horizontal velocities, with the bulk vertical velocity being higher than the horizontal one, as expected from the strong anisotropy of RBC.

These differences will be analyzed in more detail in Section 5.5.

From our data we can also extract information on vertical vorticity. In Fig. 5.3(b) we plot RMS vertical vorticity defined as $\omega_z^{RMS} \equiv \sqrt{\langle \omega_z^2 \rangle - \langle \omega_z \rangle^2}$, normalized using the viscous time τ_ν. The same trends as for vertical RMS velocities are reflected here, with the two cases with lowest Ra being almost identical and profiles that increase for higher Ra. Also here we see higher values for the non-rotating case compared to its corresponding rotating counterpart, even though the difference is less than the one we see for vertical velocities. The non-rotating case also shows a localized peak close to the sidewall, while the rotating cases have a wider radial region where the vorticity increases before dropping down at the wall.

All the quantities displayed in Fig. 5.3 are shown from half the cylinder radius onward for clarity. The inner part keeps showing a constant behavior down to approximately $\frac{1}{10}R$, a circle of around 2 cm around the axis of the cylinder where the azimuthal averaging does not give meaningful data.

5.4 Thickness of the sidewall circulation

In previous literature [38,93,102] different approaches have been used to define the thickness of the sidewall boundary layer. In Fig. 5.4 we plot the different

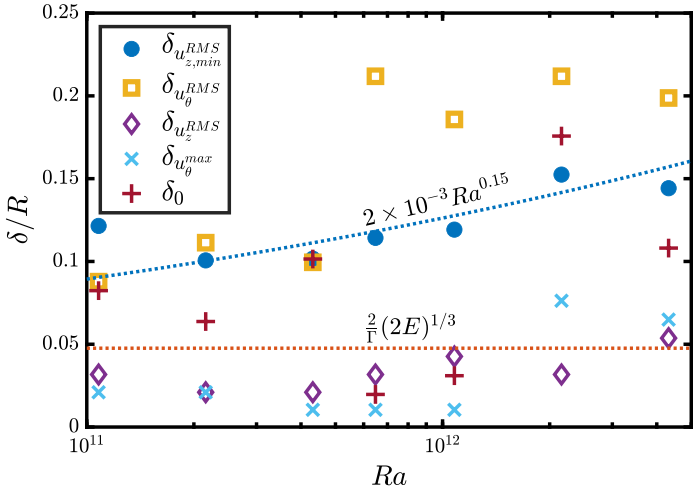

Figure 5.4: *Various thicknesses of the sidewall layer evaluated at different Ra. Definitions are indicated in the text. The red dotted line indicates the Stewartson boundary layer thickness* $\delta/R = \frac{2}{\Gamma}(2E)^{1/3}$. *The blue dotted line indicates the trend from Eq. (5.2).*

distances from the wall (the thickness δ) as a function of Ra following various definitions based on the velocity field:

- δ_0, where the azimuthal velocity averaged with respect to time and angle $\langle u_\theta \rangle_{t,\theta}$ is zero,
- $\delta_{u_\theta^{max}}$, where $\langle u_\theta \rangle_{t,\theta}$ is at its maximum,
- $\delta_{u_z^{RMS}}$, where u_z^{RMS} is at its maximum,
- $\delta_{u_\theta^{RMS}}$, where u_θ^{RMS} is at its maximum,
- $\delta_{u_{z,min}^{RMS}}$, where u_z^{RMS} has its near-wall minimum or point of inflection.

Positions of maxima are determined from parabolic fits to the near-wall profiles of mean and RMS velocity components. From the graph we can clearly see how the $\delta_{u_{z,min}^{RMS}}$ agrees well with the trend from [38], with $\delta_{u_{z,min}^{RMS}} \sim Ra^{0.15}$. Here we choose $A = 2 \times 10^{-3}$ as the prefactor of Eq. (5.2), where in [38] the prefactor $A = 3 \times 10^{-3}$ was used. This is explained by the different E used in that study ($E = 10^{-7}$) compared to the one used in this chapter ($E = 5 \times 10^{-8}$). The dependence on the Ekman number is not studied in either analysis and it is hidden in the prefactor, whereas the dependence on the Rayleigh number is confirmed. Also, $\delta_{u_z^{RMS}}$ and $\delta_{u_\theta^{max}}$ comply with the

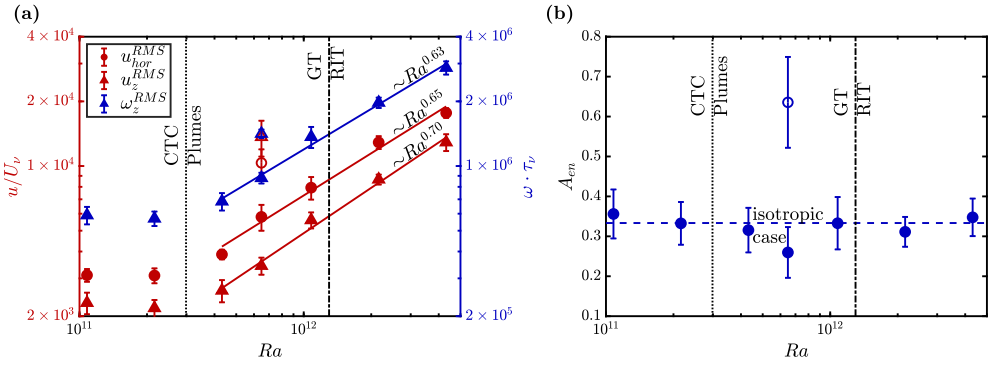

Figure 5.5: *(a) Vertical (u_z^{RMS}) and horizontal (u_{hor}^{RMS}) velocities (red, left ordinate) and vertical vorticities (ω^{RMS}) (blue,right ordinate) at mid-height vs Ra. The solid lines represent power-law fits $u_z^{RMS} \sim Ra^{0.70\pm0.06}$, $u_{hor}^{RMS} \sim Ra^{0.65\pm0.07}$ and $\omega^{RMS} \sim Ra^{0.63\pm0.05}$. (b) Kinetic energy anisotropy $A_{en} = \frac{1}{2}(u_z^{RMS})^2/K_{tot}$ versus Ra. The dashed line indicates the value that this quantity has in a totally isotropic case ($A_{en} = \frac{1}{3}$). In both panels the dotted and the dash-dotted lines represent the transitional Ra between CTCs and plumes and between GT and RIT, respectively, while open symbols represent the values for the non-rotating case.*

studies on sidewall Stewartson boundary layers [24, 25, 56, 112], with $\delta/R = \frac{2}{\Gamma}(2E)^{1/3}$. As noted in [38], the definition based on the azimuthal average of u_θ is highly sensitive to the exact structure of the sidewall layer that happens to develop at the chosen parameter values. The presence of four distinct lobes with alternating sign of u_θ makes its azimuthal average a strongly fluctuating quantity over time, which after time averaging can be quite erratic when varying Ra.

5.5 Bulk flow

After focusing on the sidewall part, we end the chapter with the analysis of the bulk flow. All the quantities analyzed in Section 5.3, u_z^{RMS}, u_{hor}^{RMS} and ω_z^{RMS}, are approximately constant in the inner part of the cylinder. From that we can extract for every Ra an average that represents the mean value of that quantity in the bulk. The bulk average is obtained by excluding the wall zone defined by Eq. (5.2) and a circle of radius 2 cm from the cylinder axis, an area where radial averaging does not give trustworthy data (see also Section 5.3).

In Fig. 5.5(a) we plot these averaged data as a function of Ra, with the error bars that represent the standard deviations of these means. As we mentioned before, the lower Ra cases, both in the CTC regime, show very similar values.

From the plumes regime onward, all the quantities display a steeper trend,

that appears not to vary between the plumes/GT and RIT states: $u_{hor}^{RMS} \sim Ra^{0.65\pm0.07}$, $u_z^{RMS} \sim Ra^{0.70\pm0.06}$ and $\omega^{RMS} \sim Ra^{0.63\pm0.05}$. From the literature concerning velocity scalings in different regimes of rotating convection (for example [99, 109]) we can expect two types of balance that might apply to our case: the visco-Archimedean-Coriolis (VAC) balance, that indicates the dominance of the viscous, buoyant and Coriolis forces, and the Coriolis-inertial-Archimedean (CIA) balance, that instead has the Coriolis, inertial and buoyancy term as the leading ones. The VAC balance predicts a velocity scaling that goes as $u^{RMS} \sim (RaNu)^{2/5}$, while the CIA scaling would be $u^{RMS} \sim (RaNu)^{1/2}$ [113]. We can use the Nu dependency derived from our heat transfer experiments (Chapter 4) that shows $Nu \sim Ra^{0.64}$ for the plumes/GT regime ($Nu \sim Ra^{0.52}$ for the RIT regime). We end up with a predicted scaling of $u^{RMS} \sim Ra^{0.82}$ ($u^{RMS} \sim Ra^{0.76}$) for the VAC balance and $u^{RMS} \sim Ra^{0.66}$ ($u^{RMS} \sim Ra^{0.61}$) for the CIA balance in the plumes/GT regime (RIT regime). Our exponents for the velocity scalings are in this range, closer to the CIA trend than to the VAC scaling, but not giving a conclusive answer on the exact dominant force balance of our flow. We are probably in a state where both inertial and viscous forces play a role: turbulent enough that inertial forces are relevant, but not yet turbulent enough to reach the diffusion-free scaling. The vorticity scaling $\omega_z^{RMS} \sim Ra^{0.63}$ nicely follows the one of horizontal velocity. From this information we can infer that the characteristic horizontal length scale ℓ for velocity fluctuations does not change much with Ra, employing the estimate $\omega_z \sim u_{hor}/\ell$. This will be further analyzed in Chapter 6. Also, we see that the vorticity does not follow previous trends measured in the rotation-affected regime of rotating convection, where vorticity scaling does not follow velocity scaling [24]. Additionally, in the rotation-affected range vertical velocities are stronger than the horizontal ones [24, 107], indicating once more that our current results are definitely representative of a different regime (the geostrophic regime).

We can see another clear difference between RRBC and non-rotating RBC: without rotation, values are overall higher, as we could see from the previous sections, but also the relative magnitudes of u_z^{RMS}, u_{hor}^{RMS} and ω_z^{RMS} are very different from the rotating cases. Vertical velocities, as expected from RBC, are stronger than the horizontal ones and the overall values are much higher than the corresponding rotating case at the same Ra.

To study the degree of anisotropy in the bulk flow, we plot in Fig. 5.5(b) the kinetic energy anisotropy for each case, defined as $A_{en} = \frac{1}{2}(u_z^{RMS})^2/K_{tot}$, where $K_{tot} = \frac{1}{2}((u_z^{RMS})^2 + (u_{hor}^{RMS})^2)$ is the total fluctuation kinetic energy. The uncertainties are calculated through error propagation from the error bars of

Fig. 5.5(a). In the isotropic case, where the energy is equally distributed among the three components, this value would be $\frac{1}{3}$. As we see from Fig. 5.5(b), the non-rotating case is far away from that value, while the rotating cases display values very close to the isotropic one, with the exception of the case with $Ra = 6.48 \times 10^{11}$, possibly a point of transition between different states of the geostrophic regime, or instead the point where the sidewall circulation has its minimum amplitude, as also discussed in Ref. [38]. The effect of rotation is to suppress the large anisotropy for non-rotating Rayleigh–Bénard convection, ending up in near-isotropy.

5.6 Conclusions

We present flow statistics that result from the stereo-PIV measurements of seven rotating Rayleigh–Bénard convection cases and one non-rotating case. From the two-dimensional averaged fields, taking into account the precession of the flow structures, we can clearly connect our measurements with Eq. (5.1), finding a good agreement. We identify a wall zone and a bulk zone whose size and appearance change with growing Ra for rotating Rayleigh–Bénard convection, and behave very differently from the non-rotating case: where in classical RBC the flow is clearly divided into the two lobes of the LSC, for the rotating cases we have a four quadrant division.

With the azimuthal averages, we analyzed the radial profile of different quantities, by plotting the RMS quantities of vertical velocity, horizontal velocity and vertical vorticity. Also here we can clearly distinguish two different flow regions, the bulk and the wall mode, and we can compare our data with Eq. (5.2), finding nice agreement. We see that for both velocities and vorticities higher Ra corresponds to higher values of these quantities, and at the same Ra the non-rotating case exhibits larger magnitudes than the corresponding rotating one.

Focusing on the sidewall zone, we find that definitions based on vertical (RMS) velocities are a better tool to fully grasp the phenomenon, where definitions based on the azimuthal velocity can at best recover the thickness of the Stewartson boundary layer. As in [38], we identify in $\delta_{z,min}^{RMS}$ the best definition to capture the growing size of the wall zone, and we find the same Ra dependency, albeit with a different prefactor that is explained by the different E chosen for this study.

Within the bulk region, for the states from plumes to RIT, the velocity scalings follow a trend that lies in the range of CIA and VAC scaling predictions, being closer to the former. The vorticity scaling follows the same trend as the

horizontal velocity, indicating that this is a different regime from earlier studies in rotation-affected convection. We also plot the energy contributions of the vertical velocity compared to the total fluctuation kinetic energy, finding that in rotating Rayleigh–Bénard convection the energy is distributed in a nearly isotropic way, in contrast to non-rotating Rayleigh–Bénard convection where the vertical component is strongly preferred.

The ultimate goal of our experimental setup is to recover the diffusion-free regime of rotating Rayleigh–Bénard convection predicted by theory [99, 109] and analyzed in models [21, 114]. Our first results of stereo-PIV measurements show that this is quite a hard task to achieve. Our confined geometry promotes the presence of a wall mode, that even though it can be of lesser influence for higher Ra_C, still influences the flow. The very low Ekman value employed in these runs is probably not low enough for reaching the "ultimate" diffusion-free geostrophic turbulent regime of rotating convection, as we can see from our velocity scalings, but we are definitely approaching its trend, getting closer to the CIA predictions. Yet, we still show the first flow measurements at such extreme parameters and we can clearly see differences with earlier works on rotation-affected convection. We do observe that the velocity scaling is moving towards the ultimate diffusion-free scaling. Moreover, we see the first experimental sign of a quadrupolar vortex state, that will be further analyzed in the following chapters.

Chapter 6

Spatial Correlations, Flow Structures and Length Scales[1]

Rotating Rayleigh–Bénard convection is an oft-employed model system to evaluate the interplay of buoyant forcing and Coriolis forces due to rotation, an eminently relevant interaction of dynamical effects found in many geophysical and astrophysical flows. These flows display extreme values of the governing parameters: large Rayleigh numbers Ra, quantifying the strength of thermal forcing, and small Ekman numbers E, a parameter inversely proportional to the rotation rate. This leads to the dominant geostrophic balance of forces in the flow between pressure gradient and Coriolis force. The so-called geostrophic regime of rotating convection is difficult to study with laboratory experiments and numerical simulations given the requirements to attain simultaneously large Ra values and small values of E. Here, we use flow measurements using stereoscopic particle image velocimetry in a large-scale rotating convection apparatus in a horizontal plane at mid-height to study the rich flow phenomenology of the geostrophic regime of rotating convection. We quantify the horizontal length scales of the flow using spatial correlations of vertical velocity and vertical vorticity, reproducing features of the convective Taylor columns and plumes flow states both part of the geostrophic regime. Additionally, we find in this horizontal plane an organisation into a quadrupolar vortex at higher Rayleigh numbers starting from the plumes state.

[1] The contents of this chapter have been adopted from M. Madonia, A. J. Aguirre Guzmán, H. J. H. Clercx, and R. P. J. Kunnen. Velocimetry in rapidly rotating convection: Spatial correlations, flow structures and length scales. *Europhys. Lett.*, 135(5):54002, 2021 [64], leaving out some introductory parts that have already been covered in this thesis; some symbols have been changed from the article to match with the current notation.

6.1 Introduction

In this chapter we employ our large-scale convection apparatus TROCONVEX [27, 60] to obtain experimental flow data with extensive coverage of the geostrophic regime, achieving unprecedented values of the governing parameters. The measurement method is stereoscopic particle image velocimetry [65], a technique that resolves full three-component flow velocity vectors in a planar cross-section. We explore the various flow features that make up the geostrophic regime and quantify their characteristic horizontal length scales using spatial correlations of vertical velocity and vertical vorticity, testing recent scaling arguments [109, 114] for the horizontal length scale of rapidly rotating convection. This correlation procedure has been employed to interpret results of numerical simulations [77]. We have successfully applied this method to experimental velocimetry results from a smaller experiment [106]. We distinguish the different flow structures from these spatial autocorrelations and the related length scales. At the same time, we search for so-called large-scale vortices (LSVs): simulations have shown that the GT state can develop a striking upscale energy transfer leading to the growth of domain-filling LSVs [21, 33, 34, 76, 115]. LSVs are so far only observed in numerical simulations of RRBC without lateral confinement: depending on the fluid and the operating parameters, a single LSV or a large dipolar vortex could be observed [34, 116]. It is thus not clear whether LSVs can manifest in RRBC experiments, too. Finally, with these flow measurements we explore the regime of rotation-influenced turbulence (RIT) that we inferred from our earlier heat flux and temperature measurements [60], with largely unknown flow properties.

6.2 Spatial autocorrelation

We can quantify and evaluate the spatial structure of the flow features by using spatial autocorrelations. This procedure has been applied to geostrophic convection results from simulations [77], where the authors have shown that the autocorrelation nicely recovers the typical radial structure of flow features like cells and CTCs, and later also to experimental data based on PIV and 3D-PTV (three-dimensional particle tracking velocimetry) [106]. Here we define the spatial autocorrelation of a scalar variable f as

$$R_f(r) = \frac{\langle f(\boldsymbol{x}) f(\boldsymbol{x}+\boldsymbol{r}) \rangle_{A,t}}{\langle f^2(\boldsymbol{x}) \rangle_{A,t}}\,, \tag{6.1}$$

where $\boldsymbol{r}$ is the separation vector with length $r = |\boldsymbol{r}|$. The angular brackets $\langle \ldots \rangle_{A,t}$ denote a spatial averaging over all available positions $\boldsymbol{x}$ within the cylinder cross-section A and all possible $\boldsymbol{r}$ emanating from there, and we apply averaging in time t as well. The effective area A for the autocorrelation is deliberately reduced to exclude the wall mode that is found near the sidewall [38, 93, 94, 98, 102, 110]; the thickness measure from [38] is employed. Within this reduced area we assume horizontal homogeneity; $\boldsymbol{r}$ can be the vector connecting any two points within that area. We use zero padding and 2D fast Fourier transforms to calculate R_f, where the resulting (axisymmetric) 2D correlation graphs are converted to 1D using binning with circular shells of width 3.7 mm.

Once the spatial autocorrelation $R_f(r)$ is known, we can compute the characteristic correlation length (or integral length scale [117]) as

$$L_f = \int_0^\infty R_f(r)\,\mathrm{d}r\,. \tag{6.2}$$

Nieves et al. [77] considered primarily correlations of temperature fluctuations T, but also of vertical velocity u_z and vertical vorticity $\omega_z = (\boldsymbol{\nabla} \times \boldsymbol{u})_z$, where $\boldsymbol{u} = (u_x, u_y, u_z)$ is the velocity vector. Rajaei et al. [106] could only consider correlation of ω_z from their regular PIV measurements. Here we shall consider both u_z and ω_z. We expect from theoretical models describing the cellular and CTC states as single-wavenumber modes [118, 119] that T, u_z and ω_z lead to very similar correlation graphs. For plumes and GT (and possibly RIT) the correlations for u_z and ω_z may develop significant differences in correlation length [77].

6.3 Flow snapshots

To get a first impression of the flow field that develops, we present instantaneous snapshots of velocity and vorticity at three different Ra/Ra_C values in figure 6.1. Panels (a,d) are in the range where CTCs are expected. We do observe vortices present in this flow, though the shields are hard to distinguish. One contributing factor is that we measure at mid-height where the columns are expected to be weaker; their vertical structure is torsional, with positive (cyclonic) vertical vorticity at one vertical end and negative (anticyclonic) vorticity at the other end [111, 118, 119]. Here we observe in animations of the flow (see the supplementary material [120]) that the flow state is quite dynamical; no quasi-steady vortex grid is formed. Instead, the vortices wander around and can interact with other vortices and the wall mode, making them not as long-

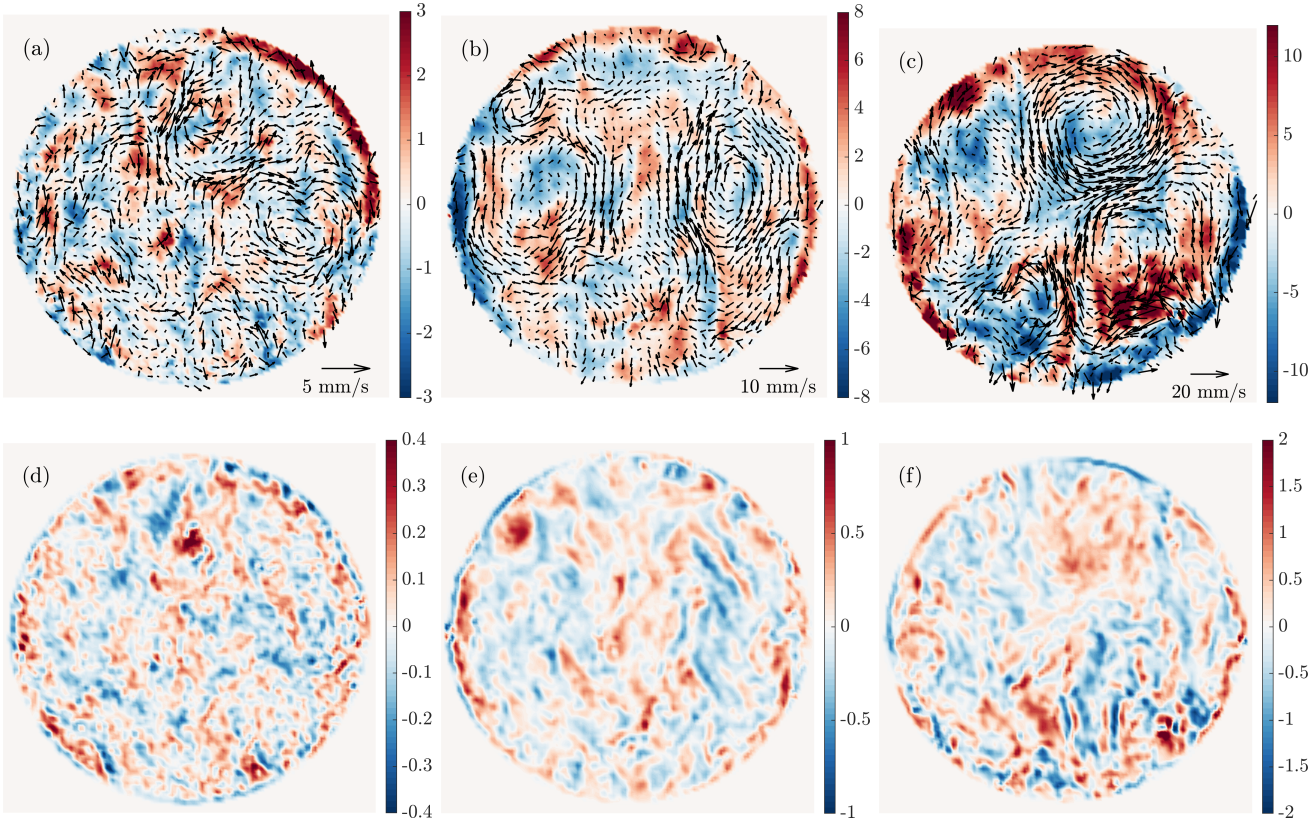

Figure 6.1: *(a–c) Flow velocity snapshots at mid-height at* $E = 5 \times 10^{-8}$ *for (a)* $Ra/Ra_C = 2.3$*, (b)* $Ra/Ra_C = 14$*, (c)* $Ra/Ra_C = 91$*. The background colour indicates vertical velocity in* mm/s*; arrows represent the in-plane velocity components. Only one ninth of the total number of vectors is plotted for clarity of the images. (d–f) Snapshots of vorticity* ω_z *in* 1/s *(red is cyclonic and blue is anticyclonic) at mid-height for (d)* $Ra/Ra_C = 2.3$*, (e)* $Ra/Ra_C = 14$*, (f)* $Ra/Ra_C = 91$*.*

lived. Near the sidewall, the signature of the wall mode [38, 93, 94, 98, 102, 110] can be seen: the top right half of the circumference displays a prominent vertically upward flow (red colour), while the opposite side shows downward flow (blue colour; though not as prominent in this snapshot). A prominent dynamical feature of this wall mode is the presence of two jets emanating from the azimuthal positions where the up- and downward lobes meet pointing radially inward [38]. These jets, more easily identified in animations of the flow (see supplementary material [120]), appear to play an important role in setting the flow structures in the bulk in motion. Similar structures have been found in (high Hartmann) magnetoconvection simulations [121, 122].

At the higher $Ra/Ra_C = 14$ (figure 6.1b,e), representative of plumes, a qualitatively similar flow field is observed. Velocities are larger given that the thermal forcing is stronger. It is readily observed that the vertical velocity is partitioned into larger patches, i.e. a larger correlation length is anticipated. At the same time, the vorticity remains confined to narrow patches. The wall mode is still quite prominently visible, though the fluctuations in the bulk have increased in magnitude compared to the amplitude of the wall mode [38] so that its relative dynamical significance is diminished.

Figures 6.1(c,f) display a snapshot at the highest $Ra/Ra_C = 91$ considered here, in the RIT range. Velocities are even larger than in the previous panel due to stronger thermal forcing. The correlation length of vertical velocity has become even larger. Contrarily, the vorticity field still reveals finer scales comparable to the previously discussed cases (figure 6.1d,e).

An interesting new feature — that can be recognised from animations of the flow field as a function of time (see supplementary material [120]) — is the organisation into a quadrupolar vortex state that fills the cross-sectional area with two cyclonic and two anticyclonic swirls. This flow arrangement forms a secondary large-scale flow somewhat reminiscent of LSV dynamics as previously observed in simulations in laterally unbounded domains. The wall mode couples to this quadrupolar vortex state (or the other way around) to organise the entire flow field into a pattern that displays a slow azimuthal drift [38]. This drift makes simple time-averaging ineffective to further illustrate this structure. Instead, we employ an orientation averaging similar to Ref. [38] and introduced in Chapter 5. We determine the phase angle of the wall mode at each time step by tracking the precession of the vertical velocity signal on a circular trajectory close to the sidewall. Each snapshot is rotated by its corresponding phase angle so that the orientation matches for each snapshot, then the velocity field is averaged to get a clear view of the mean flow profile. Figure 6.2 shows the result of such averaging, an orientation-compensated mean vorticity field for

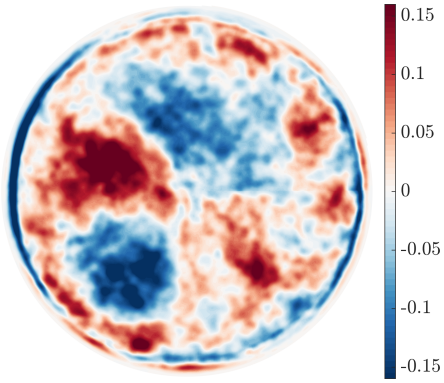

Figure 6.2: *Orientation-compensated mean vorticity field (in* 1/s*) at* $Ra/Ra_C = 47$.

the experiment at $Ra/Ra_C = 47$. There is an organisation as a quadrupolar vortex with four cores of vorticity that fill the central part of the domain.

For the nonrotating reference case (animation in the supplementary material [120]) the well-known large-scale circulation (LSC [30]; not to be confused with LSV) of nonrotating confined convection can be observed: a principal partitioning of vertical velocity into two patches (one with positive and one with negative vertical velocity) that cover the entire cross-section of the cylinder. Therefore, the largest correlation length is expected in this case, of the order of the radius of the cylinder.

6.4 Results: autocorrelations

We plot spatial autocorrelation graphs for the rotating convection cases and the nonrotating reference case in figure 6.3. In these plots we also indicate units of λ_C, the wavelength of convective instability ($\lambda_C = 4.8154E^{1/3}H$ for $Pr > 0.68$ [19]) that plays an important role throughout the geostrophic regime as a characteristic horizontal scale [21,31]. For R_{u_z}, the autocorrelation of vertical velocity, we see that the correlation is reduced as r increases, reaches a negative minimum, then approaches zero at large r. As Ra/Ra_C increases, stronger thermal forcing and more vigorous turbulence, the correlation length increases considerably. This is true even more so for the nonrotating case, where the minimum is out of the plotting range at $r/D = 0.57$. In that case the correlation length is determined by the presence of the LSC; it is of the order of the cylinder radius. The R_{u_z} results reported in Ref. [77] display a similar elongation of the correlation as Ra/Ra_C increases. However, the regular oscillatory behaviour for the CTC flow range is not reproduced here. We do not

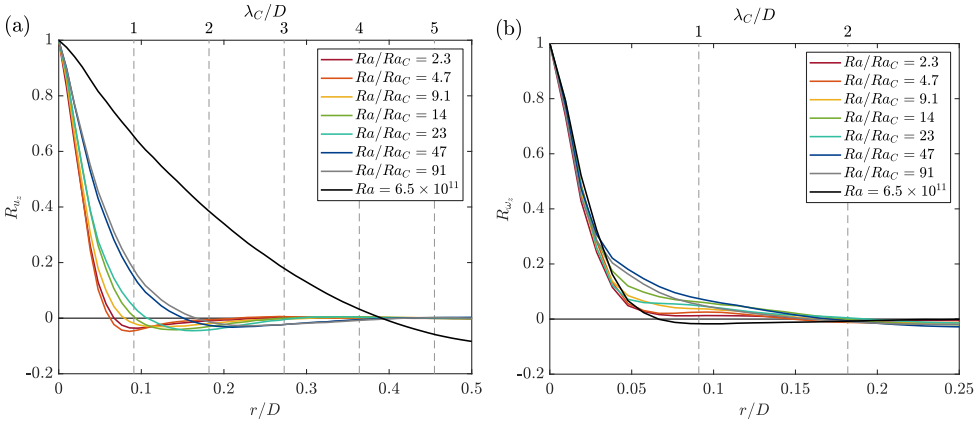

Figure 6.3: *Spatial autocorrelations of (a) vertical velocity u_z and (b) vertical vorticity ω_z. Length scales are normalised using the cell diameter D. Vertical dashed lines display multiples of λ_C for reference. Note the different horizontal axis ranges.*

see the development of a true ensemble of shielded Taylor columns. Instead, the bulk flow structures are moving around in a secondary circulation that appears to be set up by the strong wall mode in this flow range, with jets penetrating the bulk from laterally opposite sides of the cylinder cross-section [38]. This prevents the formation and preservation of a quasi-steady grid of CTCs as observed in simulations on horizontally periodic domains, e.g. [21, 32], as well as in smaller-scale experiments at larger E and Γ [106].

The vorticity correlations R_{ω_z} (figure 6.3b) decay on comparatively smaller scales than R_{u_z}, in agreement with the expectations based on the snapshots of figure 6.1. The initial decrease at small r is quite similar for all the considered cases. This is in line with a gradual transition from the structures of convection at small supercriticality (e.g. the single-mode solutions [118, 119]), where equal scales are found for velocity and vorticity, to a situation in line with nonrotating 3D turbulence composed of thin vortex tubes (e.g. Ref. [123]) with the vorticity correlation length roughly equal to the Kolmogorov length while the velocity correlation scale is the largest length scale in the flow. Then, the cases at the smallest values of Ra/Ra_C display a small oscillation that was expected for the CTC state based on earlier simulations [77] and experiments [106]. Its wavelength corresponds quite nicely with the convective wavelength λ_C. The oscillation is not as pronounced here as in the other studies, presumably due to the inability to form a quasi-steady CTC grid. For $Ra/Ra_C = 9.1$ and higher (excluding the nonrotating case) we observe the occurrence of a larger length scale on which some correlation can be seen: starting from $r/D \approx 0.05$ these

curves display a shallow downward slope, with a zero crossing at $r/D \approx 0.2$. The curves each reach a shallow minimum at $r/D \approx 0.26 - 0.30$ then asymptote to zero at large r. This correlation signature is a second indicator of the organisation into a quadrupolar vortex consisting of two cyclonic and two anticyclonic cells.

We can further quantify and compare these autocorrelation results by deriving characteristic length scales from them. We consider the integral scales L_{u_z} and L_{ω_z} as defined before. Additionally, we define length scales based on the correlation magnitude: $\ell_{0.5,u_z}$ and $\ell_{0.5,\omega_z}$ for the r where the corresponding autocorrelation has the value 0.5, and ℓ_{0,u_z} where R_{u_z} crosses zero for the first time. The zero crossing is not as informative for R_{ω_z} given the longer positive correlation that is observed. These length scales are plotted as a function of Ra/Ra_C in figure 6.4. It is clear that the vorticity-based scales are always smaller than their velocity-based counterparts. While L_{ω_z} shows some variation with Ra/Ra_C, the smaller $\ell_{0.5,\omega_z}$ remains more or less constant throughout. Indeed, the initial decay of R_{ω_z} is quite similar in all cases. At the two smallest Ra/Ra_C values considered here the velocity-based scales L_{u_z} and $\ell_{0.5,u_z}$ are of comparable size to their vorticity-based counterparts, as expected based on prior results for the CTC state [77, 106, 118, 119]. For larger $Ra/Ra_C \gtrsim 9$ the velocity-based scales become increasingly larger. Based on this observation we expect that the CTC-to-plumes transition takes place between $Ra/Ra_C = 4.7$ and 9.1. This is in agreement with the reported transition $RaE^{4/3} = 55$ (or $Ra/Ra_C = 6.3$) for the asymptotic simulations and fully in line with conclusions based on our earlier heat-flux and temperature measurements in the same setup [60]. Beyond that transition, in the plumes state, the velocity correlation widens, though for the highest two Ra/Ra_C values some saturation can be observed. The correlation graphs for these cases, in the RIT range, are in line with the plumes cases in terms of shape. The saturation of ℓ_{0,u_z} at such length is in line with the organisation into a quadrupolar structure, where correlation up to about one fourth of the diameter is expected. Note the significant difference with the nonrotating case, where correlation continues up to about half the diameter due to presence of the LSC with the cross-sectional area divided into one half upward and one half downward flow.

Two recent works have considered the horizontal length scale of convection in the geostrophic regime. Guervilly et al. [114] combine results of various numerical models to find an effective scaling $\ell \sim Ro_U^{1/2} \sim (RaE^2/Pr)^{1/2}$ with the Rossby number Ro_U based on a measured velocity scale U. In our notation this amounts to $\ell \sim Ro_C$. They only find this scaling at very small $E \lesssim 10^{-9}$. Aurnou et al. [109] provide theoretical scaling arguments based on the so-

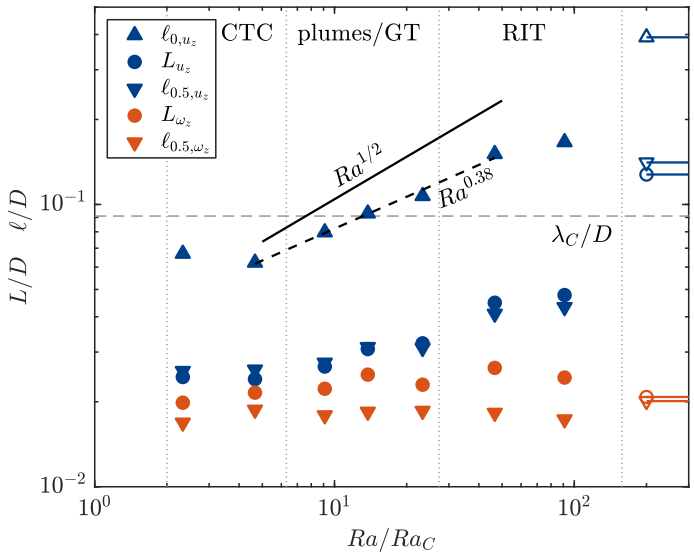

Figure 6.4: *Correlation length scales as a function of Ra/Ra_C at $E = 5 \times 10^{-8}$. Included are integral length scales L for vertical velocity and vertical vorticity, as well as length scales ℓ based on the respective correlation graphs reaching certain values. The line segments with open symbols are the corresponding results for the nonrotating reference case (same symbols and colours; not to scale in terms of Ra/Ra_C). Error intervals (not plotted) are equal to the symbol size or smaller. The horizontal dashed line indicates the convective wavelength λ_C. Vertical dotted lines indicate the regime transitions of figure 3.4. The black solid line indicates the scaling $\ell \sim Ra^{1/2}$; the black dashed line is a fit $\ell \sim Ra^{0.38}$ to the data.*

called CIA (Coriolis–Inertial–Archimedean) force balance that also predict $\ell \sim Ro_C$. In our experiments at constant E with variation of Ra this translates to $\ell \sim Ra^{1/2}$. This scaling slope is included in figure 6.4 with the solid black line; a trend clearly steeper than our data. A power law fit to our data for $4.7 \leq Ra/Ra_C \leq 47$ (dashed black line) renders a scaling $\ell \sim Ra^{0.38}$. Looking at figure 4(b) of Guervilly et al. [114], our shallower scaling corresponds nicely to the shallower trend of their data for $10^{-9} \lesssim E \lesssim 10^{-7}$, which indeed encloses our E value. While the scaling of the length scale is similar, comparison of the magnitude is not possible due to differences in domain (sphere vs. cylinder) and Pr value (0.01 vs. 5.2).

6.5 Conclusion

We have performed stereoscopic particle image velocimetry measurements in rotating thermal convection in the geostrophic regime at small Ekman number

$E = 5 \times 10^{-8}$ where the effects of rotation are prominent. The flow phenomenology has been quantitatively analysed using spatial correlations of vertical velocity and vertical vorticity. The correlation length scales based on vertical vorticity remain reasonably constant over the considered range of supercriticality values $2.3 \leq Ra/Ra_C \leq 91$, in line with observations that the critical wavelength λ_C for onset of convection is an important horizontal length scale throughout the geostrophic regime. Correlation length scales of vertical velocity grow with increasing Ra/Ra_C and can be used to identify different flow states: the state of convective Taylor columns (CTC) for $Ra/Ra_C \lesssim 6$, the plumes state for $Ra/Ra_C \gtrsim 6$ changing gradually into the previously uncharacterised state of rotation-influenced turbulence (RIT), in good agreement with earlier results from reduced numerical models in the same E range [114]. The plumes/GT and RIT ranges display an interesting new organisation into a quadrupolar vortex (recognised from orientation-compensated mean vorticity fields) which is presumably preferred over a single LSV or a dipole [34, 116] in this confined domain.

Throughout these measurements we can identify the wall mode, a coherent vertical flow structure near the sidewall consisting of one lobe with upward transport on one half of the circumference and one downward lobe on the other half. The prominence of the wall mode relative to the fluctuations in the interior diminishes at higher Ra/Ra_C. At low Ra/Ra_C the jets emanating from the wall mode set the vortical structures in horizontal motion; contrary to the results from horizontally periodic simulations no quasi-steady CTC grid forms. The nature and origin of the coupling of the wall mode and the interior flow, at both high and low limits of Ra/Ra_C, is an open question that we want to address later.

The study of rotating convection in the geostrophic regime poses challenges to experimentalists and numericists alike. Nonetheless, recent numerical works have elucidated the rich flow phenomenology that develops in this convection setting. Here, we contribute experimental results at more extreme values of the governing parameters that expand our understanding of this intriguing and geo-/astrophysically relevant flow problem, despite the influence of unexpected yet intriguing features like the persistent wall mode and its interaction with the bulk flow.

Chapter 7

Energy Transfer

In this chapter, we analyze energy spectra and energy transfer of the seven rotating Rayleigh–Bénard convection cases and the non-rotating Rayleigh–Bénard convection case that we described in the previous two chapters. The results are divided in two parts. Kinetic energy spectra are shown with a division into vertical and horizontal contributions, showing the different behavior of the two components and the prominence of the quadrupolar structure. A $k^{-5/3}$, with k the wavenumber, scaling range can be identified in all the rotating and non-rotating spectra, while a short k^{-3} scaling for smaller wavenumbers is found in the rotating cases. The scale-by-scale flux of energy is then calculated at different length scales, showing a different behavior between the cases with lower thermal forcing, dominated by the influence of the intruding jets originating from the sidewall circulation, and the ones at stronger thermal forcing that are more turbulent, where the quadrupolar structure is probably generated by an upscale transfer of energy. A traditional, purely direct energy cascade is observed for the non-rotating case.

7.1 Introduction

In the previous two chapters we saw that the flow in rotating Rayleigh–Bénard convection in our experimental setup tends to form a large-scale structure that we called the quadrupolar vortex. In Chapter 5 we could notice that, even though the different cases taken into account reside in different regions of the parameter space, all of them show a four-sector division for the horizontal velocity components. In Chapter 6, instead, we noticed from the movies that the quadrupolar structure is clearly noticeable for higher buoyant forcings (higher Ra/Ra_C). In this chapter we consider the energy spectrum and transfer of energy across the scales in order to investigate the quadrupolar vortex and its generation in more detail.

The analysis of the energy spectrum $E(k)$ — where k is the wavenumber related to the wavelength $\lambda = 2\pi/k$ of structures in the velocity field — is

a well-known tool in turbulence research. It describes how kinetic energy is distributed over the spatial scales of the flow field. Turbulent three-dimensional flows exhibit a scaling of $E(k) \sim k^{-5/3}$ in the inertial range, delimited by the scale on which the energy is injected into the system (the forcing scale) and the scale of viscous dissipation (the Kolmogorov scale) [43,124]. This scaling is due to the energy cascade, a process through which kinetic energy is transferred (without dissipation) from the larger scales to the smaller scales, until it reaches the scale at which it is dissipated by viscous forces [43].

Rotating flows, on the other hand, can under specific circumstances show a different kind of process, an inverse energy cascade, that transfers energy to the largest scale of motion in the system. It generates large-scale structures that fill the entire domain, not unlike the inverse energy cascade characteristic for 2D turbulence [43,125,126].

The distribution of energy over the spatial scales in rotating and non-rotating Rayleigh–Bénard convection have previously been explored. For example, experimentally through measurements of second-order structure functions [127,128] or by measuring proper kinetic energy spectra [129,130].

Previous numerical studies, performed in laterally unbounded domains, have shown that rapidly rotating Rayleigh–Bénard convection at high enough Ra, highly turbulent flows that are also strongly influenced by rotation, show a quasi-two-dimensional (Q2D) flow, with an upscale transfer of kinetic energy. This transfer to the largest scale is eventually balanced by friction in finite size domains and accumulates in large-scale structures, called large-scale vortices (LSV), vortex condensates that revolve parallel to the rotation axis of the system [21,33,34,76,115,131].

In this chapter we present an analysis of the energy spectra of the same cases investigated in Chapter 5 and Chapter 6 using stereo-PIV, showing the total kinetic energy as well as the contributions by horizontal and vertical velocity components. Moreover, we analyze the energy flux to see how the energy is transferred scale by scale.

The rest of the chapter is structured as follows: Section 7.2 first describes the methods we use to calculate the energy spectra and then shows the graphs of the total kinetic energy and the kinetic energy contributions due to the horizontal and the vertical velocity components. Section 7.3 is likewise divided into two parts, with the first describing the methods and the second reporting the results of the energy flux across the scales in the horizontal plane and how they possibly connect with the mechanisms of energy transfer. In Section 7.4 we present our concluding remarks.

7.2 Energy spectra

7.2.1 Methods

To compute the energy spectra we employ 2D fast Fourier transforms of the velocity field, after padding the signals with zeros up to 512 grid points per dimension to avoid artifacts due to implied periodicity in the Fourier transform [132]. Each grid point of the vector field is spaced $\Delta_x = 3.2$ mm apart, making the domain a square with side $L \approx 1.64$ m after the zero padding. This means that our lowest k value is $k_L = 2\pi/L \approx 3.83$ m^{-1}, and the maximum k value is $k_{\Delta_x} = 2\pi/2\Delta_x \approx 982$ m^{-1}. All the k values are integer multiples of k_L. Nevertheless, the smallest physically relevant k is determined by the diameter D of our circular domain: that would be given by $k_D = 2\pi/D \approx 16.1$ m^{-1}, but since all the wavenumbers are multiples of k_L, our first relevant value is $k_{min} \approx 19.2$ m^{-1}.

To discuss our maximum relevant k we need a bit more explanation. Previous literature [133, 134] has shown that the window averaging applied in PIV measurements acts as a low-pass filter in Fourier space with a cut-off wavenumber that depends on the size of the measurement window X (in our case $X = 2\Delta_x = 6.4$ mm). The PIV filtering amounts to a multiplication in Fourier space of the real signal with a squared cardinal sine function

$$\mathrm{sinc}^2(kX/2) = \left(\frac{\sin kX/2}{kX/2}\right)^2 . \tag{7.1}$$

We can then correct for it, with our "real" energy spectra becoming

$$E_{corr} = \frac{E_{measured}}{\mathrm{sinc}^2(kX/2)} , \tag{7.2}$$

where $E_{measured}$ is the spectrum measured from the PIV data and E_{corr} being the corrected one, which we show in this chapter.

Given that $\mathrm{sinc}^2(kX/2) \to 0$ as $kX/2 \to \pi$, direct application of Eq. (7.2) may cause practical difficulties. Additionally, any measurement noise will be severely amplified when approaching the zero of the denominator. To deal with this, we employ the rule of thumb proposed in Ref. [133] to cut off the spectra at a maximum $k_{max} = 2.8/X$. At this k value the filter function $\mathrm{sinc}^2(k_{max}X/2) \approx 0.5$, i.e. the filtering reduces the measured spectrum by 50%. In our case $k_{max} = 437$ m^{-1}.

7.2.2 Results

In Fig. 7.1 we show the energy spectra of seven rotating Rayleigh–Bénard convection cases (Figs. 7.1(a) to 7.1(g)) and a non-rotating case (Fig. 7.1(h)). We plot the total energy spectrum (E_{tot}) of each case together with its vertical (E_{vert}) and horizontal (E_{hor}) contributions.

The rotating cases show common features. In all of them E_{tot} exhibits a peak at $k \approx 35$ m^{-1}, that corresponds to the physical length scale $\lambda \approx 0.18$ m, approximately the size of one of the four vortices that compose the quadrupolar structure discussed in the previous chapters. These peaks are clearly determined by the horizontal energy contributions; E_{hor} shows a peak of the same magnitude and at the same location as E_{tot}. As we saw in Chapter 5 and in Chapter 6 the quadrupolar vortex is generated by the horizontal velocity field, and this is a further confirmation of it.

The shape of the remaining part of each spectrum is strongly dependent on the vertical energy contribution. As Ra/Ra_C increases, the peak in E_{vert} goes towards smaller k (larger length scales), another feature that we could see in Chapter 6 where in Fig. 6.4 we show that the length scale based on vertical velocity increases with Ra. We could think of that scale as the scale at which buoyancy is most prominently adding energy into the turbulent motion. The spectral scaling, from the maximum of E_{vert} toward larger k values, shows for all cases a very good agreement with the predicted scaling for turbulent flows $E(k) \sim k^{-5/3}$. Their contributions also modify the total energy spectra (the sum of both vertical and horizontal contributions) and the shape of the vertical-energy spectrum is reflected in the shape of the total energy spectrum, causing a shoulder on the main peak of the quadrupolar structure.

The horizontal spectra, in fact, all show a scaling trend of $E(k) \sim k^{-3}$ from the approximate location of the peak of E_{vert} to smaller wavenumbers, ending on the maximum of E_{hor}. The k^{-3} scaling could be a sign of an (nonlocal) inverse cascade [21, 34].

The non-rotating Rayleigh–Bénard convection case, instead, shows a very different situation. The peak of the overall spectrum is at k_{min}, and it is dominantly due to the contribution of E_{vert}. It is a sign of the presence of the LSC: in this configuration it is the vertical velocity that defines the structure of two lobes that fill the entire cylinder cross-section. This corresponds to a wavelength of approximately the size of the diameter of the cylinder, that in the k-space is translated to k_{min}. Here both the vertical and the horizontal contributions follow the $k^{-5/3}$ scaling.

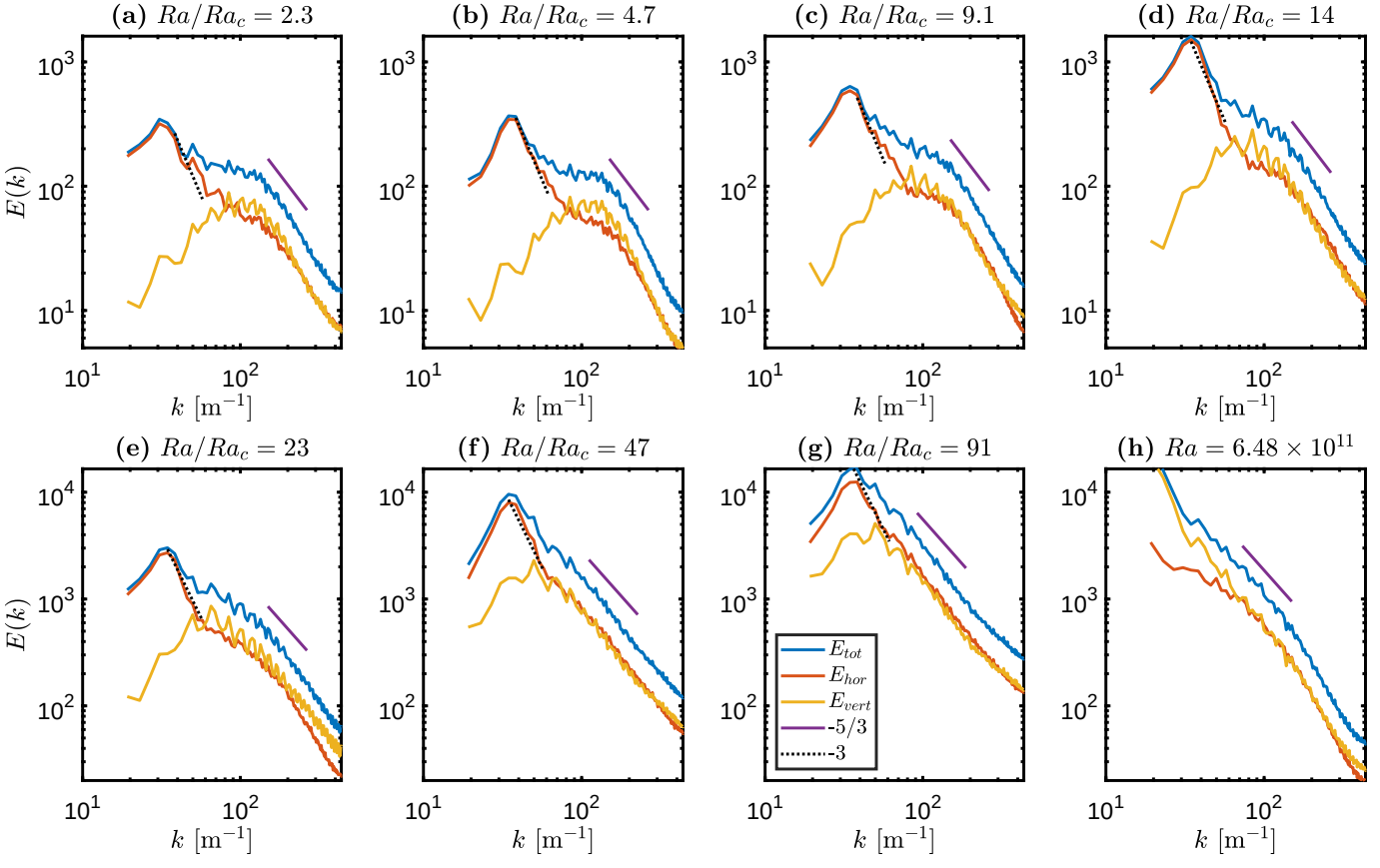

Figure 7.1: *Energy spectra divided into total energy (E_{tot}, blue), horizontal (E_{hor}, red) and vertical (E_{vert}, yellow) contributions. The solid purple line and the dotted black line indicate the scalings $E(k) \sim k^{-5/3}$ and k^{-3}, respectively.*

7.3 Energy Transfer

After having seen the spectra, we now want to analyze how the energy is transferred between scales. This can help us understand the mechanisms that generate the quadrupolar vortex. We focus on the scale-by-scale energy transfer. This analysis is performed in the physical space instead of the spectral space giving that a spectral transfer analysis of our PIV results did not give conclusive results.

7.3.1 Methods

We define the energy transfer term as follows [57, 124, 135]

$$\Pi(\boldsymbol{r}) = \frac{1}{4}\boldsymbol{\nabla}_{\boldsymbol{r}} \cdot \langle (\delta\boldsymbol{u})^2 \, \delta\boldsymbol{u} \rangle \, . \tag{7.3}$$

Here, $\delta\boldsymbol{u} = \boldsymbol{u}(\boldsymbol{x}+\boldsymbol{r}) - \boldsymbol{u}(\boldsymbol{x})$ represents the velocity increment between two points $\boldsymbol{x}$ and $\boldsymbol{x}+\boldsymbol{r}$ in the measurement plane with separation vector $\boldsymbol{r}$ and $\boldsymbol{\nabla}_{\boldsymbol{r}}$ is the gradient operator with respect to the separation vector $\boldsymbol{r}$; $\langle\cdot\rangle$ represents spatial and ensemble average. We note that the dependence on the position ($\boldsymbol{x}$) drops only for statistically homogeneous turbulence; here we assume local homogeneity only. From the RMS velocity curves in the bulk shown in Chapter 5 this should be a reasonable assumption, after having excluded the sidewall boundary zone from the calculation. Moreover, we assume that we are in a statistically stationary state, so that we can use time averaging as a replacement for ensemble averaging. The spatial average implicitly includes azimuthal averaging; transfers $\Pi(r)$ are treated to have only dependence on the separation length $r = |\boldsymbol{r}|$ within the set assumptions.

The value of $\Pi(r)$ quantifies the flux of energy from scales smaller than r towards scales larger than r. If $\Pi(r) < 0$ we have a direct cascade of energy, from larger scales to smaller scales; on the contrary if $\Pi(r) > 0$ we have an inverse transfer from smaller to larger scales.

Following Ref. [135], we can decompose the flux into its horizontal and vertical contributions:

$$\Pi = \Pi_\perp + \Pi_\parallel = \frac{1}{4}\boldsymbol{\nabla}_\perp \cdot \langle (\delta\boldsymbol{u})^2 \, \delta\boldsymbol{u}_\perp \rangle + \frac{1}{4}\nabla_\parallel \langle (\delta\boldsymbol{u})^2 \, \delta u_\parallel \rangle \, , \tag{7.4}$$

with $\boldsymbol{\nabla}_\perp = \hat{\boldsymbol{x}}\partial_{r_x} + \hat{\boldsymbol{y}}\partial_{r_y}$ and $\nabla_\parallel = \partial_{r_z}$. Here, we focus on the first term of the energy transfer and on horizontal separation vectors. This is due to our experimental settings (with our current stereo-PIV configuration we can only analyze the xy-plane). Also, highly rotational systems would give vertical

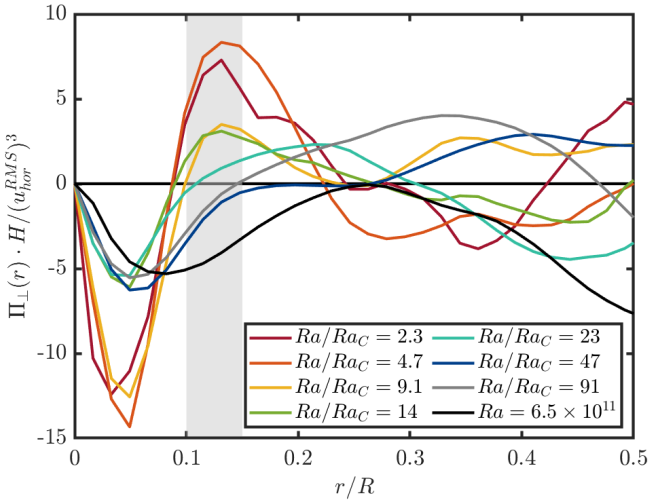

Figure 7.2: *Nondimensional horizontal energy flux $\Pi_\perp(r) \cdot H/(u_{hor}^{RMS})^3$ as a function of nondimensional horizontal separation r/R. The shaded grey area represents the approximate range of the sizes of the sidewall circulation thickness, calculated in Chapter 5.*

coherence and therefore $\Pi_\parallel \approx 0$. For our rotating cases, we consider that vertical coherence can be broadly assumed, at least for the bulk flow. We calculate the horizontal energy flux $\Pi_\perp$ along the principal coordinate directions x and y of the stereo-PIV results, where we average them assuming isotropy in the bulk zone of the cross-section.

7.3.2 Results

In Fig. 7.2 we plot the horizontal energy flux $\Pi_\perp(r)$ normalized by $(u_{hor}^{RMS})^3/H$. We can observe that all the cases have $\Pi_\perp < 0$ at small r. This represents a direct downscale cascade at smaller scales, in line with Ref. [135]. The non-rotating case (black curve) never presents a positively signed zone: as already mentioned, here we expect a mechanism of a direct cascade from large to small wavelengths at all scales.

The rotational cases, instead, show a different behavior with a part where $\Pi_\perp$ becomes positive at larger r/R. For small Ra/Ra_C we clearly see that there is a positive peak around the size of the sidewall circulation thickness that we indicate with a shaded gray area, calculated using the data shown in Fig. 5.4 and taking into account that the value shifts with Ra. This thickness is approximately the size of the jets that enter into the bulk pointing radially inwards from the positions where the two vertical-velocity lobes of the sidewall

circulation meet and interfere with the bulk flow. These jets are described in more detail in Section 5.2. We can see that the position of that first peak is quite locked, especially for the two lowest-Ra cases that are in the CTC state, that we know are strongly influenced by the intrusion of these jets (as seen in Chapter 5). These peaks might be the cause of the formation of the quadrupolar vortex structure for these cases at low supercriticality Ra/Ra_C. The jets impose a secondary circulation in the bulk that for our geometrical boundaries ends up in a four-sector division.

As Ra/Ra_C grows this peak reduces in magnitude and gets broader until it basically disappears for the two cases with the highest supercriticalities, that are in the RIT state. Here the part where $\Pi_\perp(r)$ is positive is very broad and in a clearly different scale range, suggesting a quite different origin. We anticipate that these broad positive regions could be hinting at an upscale energy transfer from small to large scales that generates the quadrupolar vortex structure for the highly turbulent cases, not unlike the formation of the LSVs [21,34]. Here the geometry also plays a role, giving this large-scale structure the same overall shape of the secondary circulation generated by the jets, but induced by a very different production mechanism: inverse energy transfer instead of jet forcing from the sidewall circulation.

We already have some hints of an inverse cascade given by the energy spectra that show a k^{-3} scaling: now the energy transfer data give further confirmation to this hypothesis. This is an issue that deserves further exploration. We do see the signs that an inverse energy transfer mechanism is at work here, but due to geometry this is expressed rather differently than in the DNS studies on horizontally periodic domains [21,33,34,76,115,131].

7.4 Conclusions

We analyze higher-order quantities from seven rotating Rayleigh–Bénard convection cases and one non-rotating Rayleigh–Bénard convection case, derived from stereo-PIV measurements. We are the first to measure energy spectra from velocity data at such high Ra numbers in rotating Rayleigh–Bénard convection. From the energy spectra we can see a clear difference between the rotating and the non-rotating experiments: while the canonical Rayleigh–Bénard convection case shows a clear sign of an LSC in its vertical kinetic energy contribution, rotating Rayleigh–Bénard convection cases have clear peaks on the horizontal contributions that reflect the size of the quadrupolar vortex. Vertical contributions of the rotating cases also show a peak that shifts to larger length scales with increasing Ra: this is in line with the findings reported in Chapter 6 where

we saw that the vertical velocity structures grow with stronger buoyant forcing. All the cases show a range where the total kinetic energy goes as $\sim k^{-5/3}$, and this range gets larger as the flow becomes more turbulent (higher Ra). The rotating cases also show a range at lower wavenumbers where $E \sim k^{-3}$. This is a hint of an inverse energy cascade that can be the cause of the quadrupolar vortex formation.

This hypothesis is further investigated with the analysis of the scale-by-scale energy transfer. We see that the energy flux in our examined plane is negative at small scales, for all the cases. This means that we have, as expected, a direct energy cascade for small length scales. The non-rotating case always shows a non-positive flux at all scales, indicating an overall transfer of energy from larger to smaller scales. The rotating cases exhibit a different behavior depending on the flow regimes they are in. Cases closer to Ra_C show a positive peak at the scale of the size of the intruding jets. We interpret this as a scenario where the jets may drive the circulation and cause the upscale transfer that is translated in the four-vortex structure. For the cases at higher Ra/Ra_C, instead, the positive peak of the energy flux is broader and distributed over a wider range of length scales. We believe this is a hint of a different mechanism: an upscale energy transfer, not unlike the large-scale vortices (LSVs) seen in DNS of rotating Rayleigh–Bénard convection on horizontally periodic domains.

The geometry of our experiment determines the shape of the overall circulation, that it is bounded to be a four-sector structure, but the different behaviors in the energy transfer graphs suggest a very different mechanism of production of such a large-scale structure. We cannot further address this open question based on the current results. A DNS in a cylindrical domain would be welcome to shed more light on this issue; the energy transfers can be studied in more detail and in spectral space when the full velocity information across the domain is available.

Chapter 8

Concluding remarks

In this thesis we analyze rotating Rayleigh–Bénard convection using a novel experimental setup, TROCONVEX, that allows us to enter a parameter range that was never explored before. This is quite important since the geostrophic regime, the regime of rotating Rayleigh–Bénard convection that we want to investigate, becomes more pronounced only when very high rotational constraint and very high buoyant forcing are reached simultaneously. In this final chapter we recapitulate our main results and propose future directions for further investigations.

8.1 Conclusions

Rotating Rayleigh–Bénard convection is studied using an experimental setup that thanks to its height (up to 4 m) can reach unprecedentedly extreme values of both Ra and E, using water as the working fluid ($Pr \approx 5.2$). Through an experimental campaign divided into two phases, consisting of heat transfer measurements and flow measurements, we could visualize and characterize the different flow states of the geostrophic regime of rotating convection. Below we summarize our main findings.

Temperature measurements of 70 rotating and non-rotating Rayleigh–Bénard convection cases with a minimum Ekman number as low as 10^{-8} have provided an extensive survey of heat transfer efficiency (Nu) at different E, including $E = \infty$ data (non-rotating Rayleigh–Bénard convection) that we used as benchmark for our experimental setup. We confirm that the geostrophic regime does indeed become wider with higher rotational force. The Nu measurements appear to be less useful than the mid-height temperature gradient if we want to clearly identify the transitions between the states. During the survey, a novel intermediate state, between GT and rotation-affected turbulence (RAT) has been identified: rotation-influenced turbulence (RIT). Its lower and upper boundaries are delineated by $Ra \simeq E^{-8/5}Pr^{3/5}$ and $Ro_C \simeq 0.06$ ($Ra \simeq 0.06^2 E^{-2} Pr$), respectively. It appears to be a different state than GT, since it exists beyond the values of Ra on which asymptotically reduced equations that postulated GT

loose their validity [21], as well as a different state than the rotation-affected regime of convection, since its transition is independent of the aspect ratio [96]. Moreover, RIT shows a clear scaling of the mid-height temperature gradient of $\sim Ra^{-0.2}$ (different from the scaling $\sim Ra^{0}$ of RAT [99]) and a Nusselt scaling of $Nu/Nu_0 \sim Ro_C^{0.39}$. In the same examination we have also visualized the different flow states, including the novel RIT state and two non-rotating Rayleigh–Bénard convection cases with different Ra.

We start the discussion of the results of our stereo-PIV measurements with a study of the flow statistics. A cross-section at half the height our cylindrical tank is illuminated by a laser sheet and we measured the three velocity components in that plane. We have performed stereo-PIV measurements for seven rotating Rayleigh–Bénard convection cases at $E = 5 \times 10^{-8}$ with varying Ra and one non-rotating Rayleigh–Bénard convection case, for comparison. Our flow measurements recover the basic results from DNS in cylindrical domains, even though our experiments are done at more extreme parameters that are not achievable by current simulations. The flow in the section, for the rotating cases, precesses with an angular speed that matches the one found in previous DNS studies [102]. With that we could analyze the precession averaged fields of the velocity, correcting for the azimuthal precession of the overall flow field. The averaged fields show a clear division in an outer (close to the sidewalls) and an inner zone (in the bulk). This phenomenon is ascribed to the recently studied sidewall circulation [38, 93], a secondary flow that develops close to the walls in laterally confined domains that is also the cause of the global precession. Another interesting feature that emerges for the horizontal velocities is a four-sector division of the flow. The non-rotating case, instead, shows a clear LSC structure outlined by the vertical velocity. The size δ/R of the sidewall zone of the rotating cases is measured through different methods and we recover two relations: $\delta/R \sim Ra^{0.15}$ (based on the near-wall minimum of vertical RMS velocity) and $\delta/R \sim E^{1/3}$ (based on peak RMS values, matching with the theoretical Stewartson boundary layer thickness), depending on the method. We analyze the flow in the bulk as well, finding that for rotating Rayleigh–Bénard convection cases horizontal RMS velocities, vertical RMS velocities and vertical RMS vorticities follow similar scaling trends, $u_{hor}^{RMS} \sim Ra^{0.65}$, $u_z^{RMS} \sim Ra^{0.70}$ and $\omega^{RMS} \sim Ra^{0.63}$, respectively. These trends indicate that with the current parameters we are close to reaching the velocity scaling of the "ultimate" diffusion-free geostrophic regime of rotating convection, but not quite there yet. Our results, nevertheless, give us hints that we are indeed getting closer than previous studies [24, 107].

We continue our analysis on the stereo-PIV data with an insight on flow

phenomenology, analyzing spatial correlation of vertical velocity and vertical vorticity. The length scale based on vorticity remains constant at different Ra/Ra_C, giving confirmation that the typical horizontal wavelength based on the onset of rotating convection ℓ_C is an important parameter for all the states in the geostrophic regime. Instead, the scale based on vertical velocity increases with increasing Ra/Ra_C, a result that confirms what have been observed in previous studies based on models [114]. Precession averaged vorticity fields and movies [120] display a large-scale organization, divided into four vortices, that we denominate the quadrupolar circulation.

We have finally analyzed energy spectra and energy transfer across the scales from our flow measurements. For rotating and non-rotating Rayleigh–Bénard convection cases, kinetic energy spectra $E(k)$ show a range where $E(k) \sim k^{-5/3}$, as one would expect from turbulent flows. The non-rotating case exhibits it for a wider range of scales than any rotating case and also has a peak for the vertical contribution at the length scale corresponding to the diameter of the cylinder, a clear signature of the LSC. The rotating cases, instead, present for the horizontal contribution a pronounced peak associated with the quadrupolar circulation, while the vertical contributions display a peak that, in confirmation with our autocorrelation findings, goes to larger scales for higher Ra/Ra_C. Scale-by-scale energy transfer investigations give us a hint of the mechanisms that generate the four-vortex structure: while for cases with lower Ra/Ra_C the energy appears to be transferred to the larger structures by the intruding jets that come from the sidewall zone, for higher Ra/Ra_C the data suggest an upscale energy transfer at larger length scales, possibly related to the inverse energy transfer that is known to generate LSVs [34, 116].

This unique, large-scale setup has given results that are clearly a major step into the understanding of the geostrophic regime. The various flow features have been recovered and characterized by scaling of the heat transfer, mean temperature gradient and velocity fluctuations. However, direct quantitative interpretation is severely complicated by the presence of the sidewall circulation, that makes comparison with laterally unbounded simulations quite complicated.

8.2 Outlook

This thesis is closed with a discussion of future directions in the study of rotating Rayleigh–Bénard convection, within the current context of TROCONVEX but also with modifications or using different approaches.

Our investigation has one working fluid at a constant mean temperature, leading to no differences in the Prandtl number Pr. We have followed this approach in order to minimize the "disturbances" that a change in Pr could

prompt in our measurements. Nevertheless, TROCONVEX can reach its lowest possible Ekman value ($E = 5 \times 10^{-9}$) only if we increase the mean temperature of the water from 31° C to ∼ 80° C, significantly modifying the Pr in the process (from $Pr \approx 5.2$ to $Pr \approx 2.1$, [27]). The heat transfer setup is prepared for these temperatures. This could be a way to get closer to the "ultimate" diffusion-free regime theorized for planetary flows [114, 136].

Another way to (drastically) change Pr within our setup would be to change working fluid from water to air ($Pr \approx 0.7$). TROCONVEX is designed to maximize the accessible flow states using water, and air would only enable access to the states further away from the onset (RA or possibly RIT).

Temperature measurements could be improved with addition of more thermistors to enhance its diagnostic power at longer time scales in particular. TROCONVEX, currently, hosts two arrays of temperature sensors inside the plates and 11 pairs of thermistors in the sidewall, vertically distributed over the height (all but one of the sections have 3 pairs of thermistors; see Fig. 3.1). Other experimental setups, for example the U-boot in Göttingen [27, 110], show how a larger number of temperature probes placed inside the working fluid at different radial and vertical positions are a promising tool for further flow analysis. The drift of the sidewall circulation could be further analyzed in more detail with additional temperature probes close to or inside the sidewall, while an array of thermistors at various radial distances could give us indications on its thickness. We did measure the properties of the sidewall circulation using stereo-PIV data, but the strength of temperature measurements is that they are more suitable for measurements that last for long time periods, and we have seen that the drift of the sidewall circulation has a very low angular speed. This strong quality about temperature measurements could also be useful if we want to analyze other features of our flow: temperature signals have been used to study the variation of temperature fluctuations in Rayleigh–Bénard convection and probe, indirectly, velocity statistics by correlating the signals of two thermistors spaced apart [41]. These measurements, although indirect, could be recorded with ease for much longer times than with PIV.

The flow measurements setup is prepared for further extension of the study: we have analyzed the case where the cross-section was at mid-height on a 2 m configuration, but the transparent segment can also be used in a 3 or 4 m configuration, allowing for flow measurements at lower E that are closer to the anticipated diffusion-free flow state. The transparent PIV segment can also be turned upside down. This alternative configuration allows us to investigate cross-sections that are closer to the top plate. Structures like CTCs and plumes are originating from the Ekman boundary layers on the bottom and top plates

and an analysis of the flow fields near the top plate similar to the one we did in this thesis would certainly give more insights on the development and vertical extent of these structures.

The transparent section is also ready to be used for other types of particle-based velocimetry techniques [137], such as particle tracking or the recently developed "Shake-the-box" technique [138]. It is of clear interest to measure the velocities in the vertical plane to improve the energy transfer analysis. A volumetric measurement technique would even give access to full volumetric velocity data: three velocity components at many positions along the three principal coordinate directions. This strongly reduces the number of assumptions required to analyze the scale-by-scale energy transfer, and may allow us to discern between the 2D vertically-invariant modes and the 3D fluctuations.

Of course, further investigation on energy spectra and energy transfer mechanisms can be done with the aid of DNS: while it cannot reach these extreme parameters, DNS provides information on the whole volume of the fluid. Simulations allow for a true scale-to-scale study on how the energy is transferred between the modes. Recent studies [21,34] have shown that LSVs are generated by a non-local upscale transfer to the largest scales of the domain: knowing how such an analysis in a horizontal plane relates to the global flow through data from simulations could help us interpret and extrapolate our current data of a single slice of our domain. DNS on a cylindrical domain can be used to discern the origin of the quadrupolar vortex observed in our experiments, and determine whether it is generated by an upscale energy transfer, by the intruding jets or by other causes that have not been considered yet.

Another open issue is the effect of the geometry on the turbulent convective flow that develops. This is clear from the results presented in this thesis and comparison with results from simulations on horizontally unbounded periodic domains. We know that the presence of the sidewall circulation can strongly interfere with both the global heat transfer and the velocities of the flow, especially for cases not far from the onset [38,95,102,139], but possibly at high Ra/Ra_C the influence is so little than we can directly compare our data with idealized models without sidewalls, or, perhaps, the need of a different, less slender, setup will clearly arise. There lies another opportunity where DNS may prove to be more flexible than an experiment.

Considering that experiments can now explore regions of the parameter space not accessible by numerical simulation, the combination of laboratory experiments and simulations is a path that can lead to a better comprehension of the astrophysical and geophysical flows that are so fascinating and relevant, yet still ill-understood.

Bibliography

[1] F. H. Busse. Convection driven zonal flows and vortices in the major planets. *Chaos*, 4(2):123–134, 1994. (Cited on page 1.)

[2] F. H. Busse and C. R. Carrigan. Laboratory simulation of thermal convection in rotating planets and stars. *Science*, 191(4222):81–83, 1976. (Cited on page 1.)

[3] G. Budéus, B. Cisewski, S. Ronski, D. Dietrich, and M. Weitere. Structure and effects of a long lived vortex in the Greenland Sea. *Geophys. Res. Lett*, 31(5), 2004. (Cited on page 1.)

[4] J.-C. Gascard, A. J. Watson, M.-J. Messias, K. A. Olsson, T. Johannessen, and K. Simonsen. Long-lived vortices as a mode of deep ventilation in the Greenland Sea. *Nature*, 416(6880):525–527, 2002. (Cited on page 1.)

[5] J. Marshall and F. Schott. Open-ocean convection: Observations, theory, and models. *Rev. Geophys*, 37(1):1–64, 1999. (Cited on pages 1 and 2.)

[6] P. Wadhams, J. Holfort, E. Hansen, and J. P. Wilkinson. A deep convective chimney in the winter Greenland Sea. *Geophys. Res. Lett.*, 29(10):76–1, 2002. (Cited on page 1.)

[7] G. Hadley. Concerning the cause of the general trade-winds. *Phil. Trans. R. Soc. Lond.*, 39(437):58–62, 1735. (Cited on page 1.)

[8] P. Cardin and P. Olson. Chaotic thermal convection in a rapidly rotating spherical shell: consequences for flow in the outer core. *Phys. Earth Planet. Inter.*, 82(3-4):235–259, 1994. (Cited on page 1.)

[9] G. A. Glatzmaier, R. S. Coe, L. Hongre, and P. H. Roberts. The role of the Earth's mantle in controlling the frequency of geomagnetic reversals. *Nature*, 401(6756):885–890, 1999. (Cited on page 1.)

[10] C. A. Jones. Convection–driven geodynamo models. *Phil. Trans. R. Soc. Lond. A*, 358(1768):873–897, 2000. (Cited on page 1.)

[11] G. R. Sarson. Reversal models from dynamo calculations. *Phil. Trans. R. Soc. Lond. A*, 358(1768):921–942, 2000. (Cited on page 1.)

[12] H. Bénard. Les tourbillons cellulaires dans une nappe liquide. *Rev. Gén. Sci. Pure Appl.*, 11:1261–1271, 1900. (Cited on page 1.)

[13] H. Bénard. Les tourbillons cellulaires dans une nappe liquide. *Rev. Gén. Sci. Pure Appl.*, 11:1309–1328, 1900. (Cited on page 1.)

[14] H. Bénard. Les tourbillons cellulaires dans une nappe liquide transportant de la chaleur par convection en régime permanent. *Ann. Chim. Phys.*, 23:62–144, 1901. (Cited on page 1.)

[15] Lord Rayleigh. On convection currents in a horizontal layer of fluid, when the higher temperature is on the under side. *Phil. Mag.*, 32(192):529–546, 1916. (Cited on page 1.)

[16] M. S. Miesch. The coupling of solar convection and rotation. *Solar Phys.*, 192:59–89, 2000. (Cited on page 2.)

[17] G. Schubert and K. M. Soderlund. Planetary magnetic fields: observations and models. *Phys. Earth Planet. Inter.*, 187(3-4):92–108, 2011. (Cited on pages 2, 30, and 42.)

[18] J. M. Aurnou, M. A. Calkins, J. S. Cheng, K. Julien, E. M. King, D. Nieves, K. M. Soderlund, and S. Stellmach. Rotating convective turbulence in Earth and planetary cores. *Phys. Earth Planet. Inter.*, 246:52–71, 2015. (Cited on pages 2, 30, and 32.)

[19] S. Chandrasekhar. *Hydrodynamic and Hydromagnetic Stability*. Oxford University Press, Oxford, 1961. (Cited on pages 2, 9, 11, and 62.)

[20] H. P. Greenspan. *The Theory of Rotating Fluids*. Cambridge University Press, 1968. (Cited on pages 2, 8, 13, and 14.)

[21] K. Julien, A. M. Rubio, I. Grooms, and E. Knobloch. Statistical and physical balances in low Rossby number Rayleigh–Bénard convection. *Geophys. Astrophys. Fluid Dyn.*, 106(4-5):392–428, 2012. (Cited on pages 2, 4, 30, 32, 33, 38, 39, 40, 44, 48, 55, 58, 62, 63, 68, 70, 74, 78, and 81.)

[22] R. P. J. Kunnen. The geostrophic regime of rapidly rotating turbulent convection. *J. Turbul.*, 22:267–296, 2021. (Cited on pages 2 and 4.)

[23] A. J. Aguirre Guzmán, M. Madonia, J. S. Cheng, R. Ostilla-Mónico, H. J. H. Clercx, and R. P. J. Kunnen. Force balance in rapidly rotating Rayleigh–Bénard convection. *J. Fluid Mech.*, 928, 2021. (Cited on pages 3 and 44.)

[24] R. P. J. Kunnen, B. J. Geurts, and H. J. H. Clercx. Experimental and numerical investigation of turbulent convection in a rotating cylinder. *J. Fluid Mech.*, 642:445–476, 2010. (Cited on pages 2, 20, 21, 44, 52, 53, and 78.)

[25] R. P. J. Kunnen, R. J. A. M. Stevens, J. Overkamp, C. Sun, G. J. F. van Heijst, and H. J. H. Clercx. The role of Stewartson and Ekman layers in turbulent rotating Rayleigh–Bénard convection. *J. Fluid Mech.*, 688:422, 2011. (Cited on pages 2 and 52.)

[26] R. J. A. M. Stevens, H. J. H. Clercx, and D. Lohse. Effect of plumes on measuring the large scale circulation in turbulent Rayleigh–Bénard convection. *Phys. Fluids*, 23(9):095110, 2011. (Cited on page 2.)

[27] J. S. Cheng, J. M. Aurnou, K. Julien, and R. P. J. Kunnen. A heuristic framework for next-generation models of geostrophic convective turbulence. *Geophys. Astrophys. Fluid Dyn.*, 112(4):277–300, 2018. (Cited on pages 2, 4, 5, 7, 26, 30, 33, 35, 36, 38, 58, and 80.)

[28] A. J. Aguirre Guzmán. *Numerical study of rapidly rotating turbulent convection*. PhD thesis, Eindhoven University of Technology, Eindhoven, The Netherlands, 2021. (Cited on pages 2 and 4.)

[29] R. J. A. M. Stevens, H. J. H. Clercx, and D. Lohse. Heat transport and flow structure in rotating Rayleigh–Bénard convection. *Eur. J. Mech. B Fluids*, 40:41–49, 2013. (Cited on pages 4, 33, and 40.)

[30] G. Ahlers, S. Grossmann, and D. Lohse. Heat transfer and large scale dynamics in turbulent Rayleigh-Bénard convection. *Rev. Mod. Phys.*, 81(2):503, 2009. (Cited on pages 4, 33, 38, 48, and 62.)

[31] M. Sprague, K. Julien, E. Knobloch, and J. Werne. Numerical simulation of an asymptotically reduced system for rotationally constrained convection. *J. Fluid Mech.*, 551:141, 2006. (Cited on pages 4, 30, 33, and 62.)

[32] S. Stellmach, M. Lischper, K. Julien, G. Vasil, J. S. Cheng, A. Ribeiro, E. M. King, and J. M. Aurnou. Approaching the asymptotic regime of

rapidly rotating convection: boundary layers versus interior dynamics. *Phys. Rev. Lett.*, 113(25):254501, 2014. (Cited on pages 4, 30, 33, 35, 44, and 63.)

[33] R. P. J. Kunnen, R. Ostilla-Mónico, E. P. van der Poel, R. Verzicco, and D. Lohse. Transition to geostrophic convection: the role of the boundary conditions. *J. Fluid Mech.*, 799:413–432, 2016. (Cited on pages 4, 30, 33, 38, 58, 68, and 74.)

[34] A. J. Aguirre Guzmán, M. Madonia, J. S. Cheng, R. Ostilla-Mónico, H. J. H. Clercx, and R. P. J. Kunnen. Competition between Ekman plumes and vortex condensates in rapidly rotating thermal convection. *Phys. Rev. Lett.*, 125(21):214501, 2020. (Cited on pages 4, 44, 58, 66, 68, 70, 74, 79, and 81.)

[35] R. E. Ecke and J. J. Niemela. Heat transport in the geostrophic regime of rotating Rayleigh–Bénard convection. *Phys. Rev. Lett.*, 113(11):114301, 2014. (Cited on pages 4, 30, 33, and 36.)

[36] J. S. Cheng, S. Stellmach, A. Ribeiro, A. Grannan, E. M. King, and J. M. Aurnou. Laboratory-numerical models of rapidly rotating convection in planetary cores. *Geophys. J. Int.*, 201(1):1–17, 2015. (Cited on pages 4, 30, 33, 35, 36, and 37.)

[37] K. Julien, E. Knobloch, A. M. Rubio, and G. M. Vasil. Heat transport in low-Rossby-number Rayleigh–Bénard convection. *Phys. Rev. Lett.*, 109(25):254503, 2012. (Cited on pages 4, 33, 37, and 38.)

[38] X. M. de Wit, A. J. Aguirre Guzmán, M. Madonia, J. S. Cheng, H. J. H. Clercx, and R. P. J. Kunnen. Turbulent rotating convection confined in a slender cylinder: The sidewall circulation. *Phys. Rev. Fluids*, 5(2):023502, 2020. (Cited on pages 4, 20, 21, 36, 39, 44, 45, 46, 48, 50, 51, 52, 54, 59, 61, 63, 78, and 81.)

[39] A. Oberbeck. Über die Wärmeleitung der Flüssigkeiten bei Berücksichtigung der Strömungen infolge von Temperaturdifferenzen. *Ann. Phys.*, 243(6):271–292, 1879. (Cited on page 7.)

[40] J. V. Boussinesq. *Théorie Analytique de la Chaleur*, volume 2. Paris: Gauthier-Villars, 1903. (Cited on page 7.)

[41] J. J. Niemela, L. Skrbek, K. R. Sreenivasan, and R. J. Donnelly. Turbulent convection at very high Rayleigh numbers. *Nature*, 404(6780):837–840, 2000. (Cited on pages 7, 33, and 80.)

[42] X. Chavanne, F. Chillà, B. Chabaud, B. Castaing, and B. Hébral. Turbulent Rayleigh–Bénard convection in gaseous and liquid He. *Phys. Fluids*, 13(5):1300–1320, 2001. (Cited on page 7.)

[43] P. K. Kundu, I. M. Cohen, and D. Dowling. *Fluid Mechanics*. Elsevier, 6th edition, 2016. (Cited on pages 8, 13, and 68.)

[44] L. Prandtl. Meteorologische Anwendung der Strömungslehre. *Beitr. Phys. Atmosph.*, 19:188–202, 1932. (Cited on page 9.)

[45] P. A. Gilman. Nonlinear dynamics of Boussinesq convection in a deep rotating spherical shell-I. *Geophys. Astrophys. Fluid Dyn.*, 8(1):93–135, 1977. (Cited on pages 9, 21, and 37.)

[46] K. Julien, S. Legg, J. McWilliams, and J. Werne. Rapidly rotating turbulent Rayleigh–Bénard convection. *J. Fluid Mech.*, 322:243–273, 1996. (Cited on pages 9 and 30.)

[47] R. J. A. M. Stevens, J.-Q. Zhong, H. J. H. Clercx, G. Ahlers, and D. Lohse. Transitions between turbulent states in rotating Rayleigh–Bénard convection. *Phys. Rev. Lett.*, 103(2):024503, 2009. (Cited on page 9.)

[48] J. M. Aurnou, V. Bertin, A. M. Grannan, S. Horn, and T. Vogt. Rotating thermal convection in liquid gallium: Multi-modal flow, absent steady columns. *J. Fluid Mech.*, 846:846–876, 2018. (Cited on page 11.)

[49] W. B. Heard and G. Veronis. Asymptotic treatment of the stability of a rotating layer of fluid with rigid boundaries. *Geophys. Fluid Dyn.*, 2(1):299–316, 1971. (Cited on page 11.)

[50] K. Julien, J. M. Aurnou, M. A. Calkins, E. Knobloch, P. Marti, S. Stellmach, and G. M. Vasil. A nonlinear model for rotationally constrained convection with Ekman pumping. *J. Fluid Mech.*, 798:50–87, 2016. (Cited on page 11.)

[51] J. Pedlosky. *Geophysical Fluid Dynamics*. Springer, 1979. (Cited on page 13.)

[52] G. I. Taylor. Motion of solids in fluids when the flow is not irrotational. *Proc. R. Soc. Lond. A*, 93(648):99–113, 1917. (Cited on page 13.)

[53] J. Proudman. On the motion of solids in a liquid possessing vorticity. *Proc. R. Soc. Lond. A*, 92(642):408–424, 1916. (Cited on page 13.)

[54] K. Stewartson. On almost rigid rotations. *J. Fluid Mech.*, 3(1):17–26, 1957. (Cited on page 14.)

[55] K. Stewartson. On almost rigid rotations. Part 2. *J. Fluid Mech.*, 26(1):131–144, 1966. (Cited on page 14.)

[56] R. P. J. Kunnen, H. J. H. Clercx, and G. J. F. van Heijst. The structure of sidewall boundary layers in confined rotating Rayleigh–Bénard convection. *J. Fluid Mech.*, 727:509–532, 2013. (Cited on pages 14 and 52.)

[57] A. S. Monin and A. M. Yaglom. *Statistical Fluid Mechanics*, volume 2. The MIT Press, Cambridge, Mass., 1975. (Cited on pages 15 and 72.)

[58] B. I. Shraiman and E. D. Siggia. Heat transport in high-Rayleigh-number convection. *Phys. Rev. A*, 42(6):3650, 1990. (Cited on page 16.)

[59] E. D. Siggia. High Rayleigh number convection. *Annu. Rev. Fluid Mech.*, 26(1):137–168, 1994. (Cited on page 16.)

[60] J. S. Cheng, M. Madonia, A. J. Aguirre Guzmán, and R. P. J. Kunnen. Laboratory exploration of heat transfer regimes in rapidly rotating turbulent convection. *Phys. Rev. Fluids*, 5(11):113501, 2020. (Cited on pages 17, 19, 26, 29, 58, and 64.)

[61] S. Horn and J. M. Aurnou. Rotating convection with centrifugal buoyancy: Numerical predictions for laboratory experiments. *Phys. Rev. Fluids*, 4:073501, 2019. (Cited on page 19.)

[62] David R. Lide. *CRC Handbook of Chemistry and Physics: A Ready–Reference Book of Chemical and Physical Data: 2003–2004*. CRC Press, 2003. (Cited on page 20.)

[63] E. Brown and G. Ahlers. Temperature gradients, and search for non-Boussinesq effects, in the interior of turbulent Rayleigh-Bénard convection. *Europhys. Lett.*, 80(1):14001, 2007. (Cited on page 20.)

[64] M. Madonia, A. J. Aguirre Guzmán, H. J. H. Clercx, and R. P. J. Kunnen. Velocimetry in rapidly rotating convection: Spatial correlations, flow structures and length scales. *Europhys. Lett.*, 135(5):54002, 2021. (Cited on pages 26 and 57.)

[65] M. Raffel, C. E. Willert, S. T. Wereley, and J. Kompenhans. *Particle Image Velocimetry*. Springer, Berlin, 2nd edition, 2007. (Cited on pages 26 and 58.)

[66] G. A. Glatzmaier and P. H. Roberts. A three-dimensional convective dynamo solution with rotating and finitely conducting inner core and mantle. *Phys. Earth Planet. Inter.*, 91(1):63–75, 1995. (Cited on page 29.)

[67] M. Heimpel, J. Aurnou, and J. Wicht. Simulation of equatorial and high-latitude jets on Jupiter in a deep convection model. *Nature*, 438:193–196, 2005. (Cited on page 29.)

[68] H. T. Rossby. A study of Bénard convection with and without rotation. *J. Fluid Mech.*, 36(2):309–335, 1969. (Cited on page 30.)

[69] Y. Liu and R. E. Ecke. Heat transport scaling in turbulent Rayleigh–Bénard convection: effects of rotation and Prandtl number. *Phys. Rev. Lett.*, 79(12):2257, 1997. (Cited on page 30.)

[70] R. P. J. Kunnen, H. J. H. Clercx, and B. J. Geurts. Breakdown of large-scale circulation in turbulent rotating convection. *Europhys. Lett.*, 84(2):24001, 2008. (Cited on pages 30 and 44.)

[71] J.-Q. Zhong, R. J. A. M. Stevens, H. J. H. Clercx, R. Verzicco, D. Lohse, and G. Ahlers. Prandtl-, Rayleigh-, and Rossby-number dependence of heat transport in turbulent rotating Rayleigh–Bénard convection. *Phys. Rev. Lett.*, 102(4):044502, 2009. (Cited on pages 30, 33, and 40.)

[72] S. Schmitz and A. Tilgner. Heat transport in rotating convection without Ekman layers. *Phys. Rev. E*, 80(1):015305, 2009. (Cited on page 30.)

[73] P. H. Roberts and E. M. King. On the genesis of the Earth's magnetism. *Rep. Prog. Phys.*, 76:096801, 2013. (Cited on page 30.)

[74] S. Weiss and G. Ahlers. Heat transport by turbulent rotating Rayleigh–Bénard convection and its dependence on the aspect ratio. *J. Fluid Mech.*, 684:407, 2011. (Cited on page 30.)

[75] E. M. King, S. Stellmach, and J. M. Aurnou. Heat transfer by rapidly rotating Rayleigh–Bénard convection. *J. Fluid Mech.*, 691:568–582, 2012. (Cited on pages 30 and 35.)

[76] B. Favier, L. J. Silvers, and M. R. E. Proctor. Inverse cascade and symmetry breaking in rapidly rotating Boussinesq convection. *Phys. Fluids*, 26(9):096605, 2014. (Cited on pages 30, 58, 68, and 74.)

[77] D. Nieves, A. M. Rubio, and K. Julien. Statistical classification of flow morphology in rapidly rotating Rayleigh–Bénard convection. *Phys. Fluids*, 26(8):086602, 2014. (Cited on pages 30, 32, 35, 37, 38, 44, 58, 59, 62, 63, and 64.)

[78] J. Taylor. *Introduction to Error Analysis, The Study of Uncertainties in Physical Measurements*. University Science Books, second edition, 1997. (Cited on pages 31 and 32.)

[79] G. V. Bayley and J. M. Hammersley. The "effective" number of independent observations in an autocorrelated time series. *J. R. Stat. Soc. Suppl.*, 8(2):184–197, 1946. (Cited on page 31.)

[80] A. Zięba and P. Ramza. Standard deviation of the mean of autocorrelated observations estimated with the use of the autocorrelation function estimated from the data. *Metrol. Meas. Syst.*, 18(4):529–542, 2011. (Cited on page 31.)

[81] D. Borrero-Echeverry, C. J. Crowley, and T. P. Riddick. Rheoscopic fluids in a post-Kalliroscope world. *Phys. Fluids*, 30(8):087103, 2018. (Cited on page 32.)

[82] T. Gastine, J. Wicht, and J. Aubert. Scaling regimes in spherical shell rotating convection. *J. Fluid Mech.*, 808:690–732, 2016. (Cited on page 33.)

[83] E. Brown, A. Nikolaenko, D. Funfschilling, and G. Ahlers. Heat transport in turbulent Rayleigh-Bénard convection: Effect of finite top-and bottom-plate conductivities. *Phys. Fluids*, 17(7):075108, 2005. (Cited on page 33.)

[84] C. Sun, L.-Y. Ren, H. Song, and K.-Q. Xia. Heat transport by turbulent Rayleigh-Bénard convection in 1 m diameter cylindrical cells of widely varying aspect ratio. *J. Fluid Mech.*, 542:165–174, 2005. (Cited on page 33.)

[85] D. Funfschilling, E. Bodenschatz, and G. Ahlers. Search for the "ultimate state" in turbulent Rayleigh–Bénard convection. *Phys. Rev. Lett.*, 103(1):014503, 2009. (Cited on page 33.)

[86] J. J. Niemela, S. Babuin, and K. R. Sreenivasan. Turbulent rotating convection at high Rayleigh and Taylor numbers. *J. Fluid Mech.*, 649:509, 2010. (Cited on page 33.)

[87] W. V. R. Malkus. The heat transport and spectrum of thermal turbulence. *Proc. R. Soc. Lond. A*, 225(1161):196–212, 1954. (Cited on page 33.)

[88] R. H. Kraichnan. Turbulent thermal convection at arbitrary Prandtl number. *Phys. Fluids*, 5(11):1374–1389, 1962. (Cited on page 33.)

[89] X. Chavanne, F. Chillà, B. Castaing, B. Hébral, B. Chabaud, and J. Chaussy. Observation of the ultimate regime in Rayleigh–Bénard convection. *Phys. Rev. Lett.*, 79:3648–3651, 1997. (Cited on page 33.)

[90] X. He, D. Funfschilling, H. Nobach, E. Bodenschatz, and G. Ahlers. Transition to the ultimate state of turbulent Rayleigh–Bénard convection. *Phys. Rev. Lett.*, 108:024502, 2012. (Cited on page 33.)

[91] K. P. Iyer, J. D. Scheel, J. Schumacher, and K. R. Sreenivasan. Classical 1/3 scaling of convection holds up to $Ra = 10^{15}$. *Proc. Natl. Acad. Sci. USA*, 117:7594–7598, 2020. (Cited on page 35.)

[92] D. Funfschilling, E. Brown, A. Nikolaenko, and G. Ahlers. Heat transport by turbulent Rayleigh–Bénard convection in cylindrical samples with aspect ratio one and larger. *J. Fluid Mech.*, 536:145–154, 2005. (Cited on page 35.)

[93] X. Zhang, D. P. M. Van Gils, S. Horn, M. Wedi, L. Zwirner, G. Ahlers, R. E. Ecke, S. Weiss, E. Bodenschatz, and O. Shishkina. Boundary zonal flow in rotating turbulent Rayleigh–Bénard convection. *Phys. Rev. Lett.*, 124(8):084505, 2020. (Cited on pages 36, 39, 44, 46, 50, 59, 61, and 78.)

[94] B. Favier and E. Knobloch. Robust wall states in rapidly rotating Rayleigh–Bénard convection. *J. Fluid Mech.*, 895:R1, 2020. (Cited on pages 36, 39, 44, 59, and 61.)

[95] H.-Y. Lu, G.-Y. Ding, J.-Q. Shi, K.-Q. Xia, and J.-Q. Zhong. Heat-transport scaling and transition in geostrophic rotating convection with varying aspect ratio. *Phys. Rev. Fluids*, 6(7):L071501, 2021. (Cited on pages 36 and 81.)

[96] S. Weiss, R. J. A. M. Stevens, J.-Q. Zhong, H. J. H. Clercx, D. Lohse, and G. Ahlers. Finite-size effects lead to supercritical bifurcations in turbulent rotating Rayleigh–Bénard convection. *Phys. Rev. Lett.*, 105:224501, 2010. (Cited on pages 36 and 78.)

[97] S. Grossmann and D. Lohse. Scaling in thermal convection: a unifying theory. *J. Fluid Mech.*, 407:27–56, 2000. (Cited on page 38.)

[98] O. Shishkina. Tenacious wall states in thermal convection in rapidly rotating containers. *J. Fluid Mech.*, 898, 2020. (Cited on pages 38, 59, and 61.)

[99] E. M. King, S. Stellmach, and B. Buffett. Scaling behaviour in Rayleigh–Bénard convection with and without rotation. *J. Fluid Mech.*, 717:449–471, 2013. (Cited on pages 39, 44, 53, 55, and 78.)

[100] A. J. Aguirre Guzmán, M. Madonia, J. S. Cheng, R. Ostilla-Mónico, H. J. H. Clercx, and R. P. J. Kunnen. Flow- and temperature-based statistics characterizing the regimes in rapidly rotating turbulent convection in simulations employing no-slip boundary conditions. *Phys. Rev. Fluids*, 7(1):013501, 2022. (Cited on page 40.)

[101] J. S. Cheng and J. M. Aurnou. Tests of diffusion-free scaling behaviors in numerical dynamo datasets. *Earth Planet. Sci. Lett.*, 436:121–129, 2016. (Cited on page 42.)

[102] X. Zhang, R. E. Ecke, and O. Shishkina. Boundary zonal flows in rapidly rotating turbulent thermal convection. *J. Fluid Mech.*, 915, 2021. (Cited on pages 44, 46, 50, 59, 61, 78, and 81.)

[103] S. Horn and O. Shishkina. Toroidal and poloidal energy in rotating Rayleigh–Bénard convection. *J. Fluid Mech.*, 762:232–255, 2015. (Cited on page 44.)

[104] M. Plumley, K. Julien, P. Marti, and S. Stellmach. The effects of Ekman pumping on quasi-geostrophic Rayleigh–Bénard convection. *J. Fluid Mech.*, 803:51–71, 2016. (Cited on page 44.)

[105] H. Rajaei, P. Joshi, K. M. J. Alards, R. P. J. Kunnen, F. Toschi, and H. J. H. Clercx. Transitions in turbulent rotating convection: A Lagrangian perspective. *Phys. Rev. E*, 93:043129, 2016. (Cited on page 44.)

[106] H. Rajaei, R. P. J. Kunnen, and H. J. H. Clercx. Exploring the geostrophic regime of rapidly rotating convection with experiments. *Phys. Fluids*, 29(4):045105, 2017. (Cited on pages 44, 58, 59, 63, and 64.)

[107] H. Rajaei, K. M. J. Alards, R. P. J. Kunnen, and H. J. H. Clercx. Velocity and acceleration statistics in rapidly rotating Rayleigh–Bénard convection. *J. Fluid Mech.*, 857:374–397, 2018. (Cited on pages 44, 53, and 78.)

[108] J.-Q. Shi, H.-Y. Lu, S.-S. Ding, and J.-Q. Zhong. Fine vortex structure and flow transition to the geostrophic regime in rotating Rayleigh-Bénard convection. *Phys. Rev. Fluids*, 5(1):011501, 2020. (Cited on page 44.)

[109] J. M. Aurnou, S. Horn, and K. Julien. Connections between nonrotating, slowly rotating, and rapidly rotating turbulent convection transport scalings. *Phys. Rev. Research*, 2:043115, 2020. (Cited on pages 44, 53, 55, 58, and 64.)

[110] M. Wedi, D. P. M. van Gils, E. Bodenschatz, and S. Weiss. Rotating turbulent thermal convection at very large Rayleigh numbers. *J. Fluid Mech.*, 912:A30, 2021. (Cited on pages 46, 59, 61, and 80.)

[111] S. Sakai. The horizontal scale of rotating convection in the geostrophic regime. *J. Fluid Mech.*, 333:85–95, 1997. (Cited on pages 48 and 59.)

[112] R. P. J. Kunnen, Y. Corre, and H. J. H. Clercx. Vortex plume distribution in confined turbulent rotating convection. *Europhys. Lett.*, 104(5):54002, 2014. (Cited on page 52.)

[113] E. M. King and B. A. Buffett. Flow speeds and length scales in geodynamo models: the role of viscosity. *Earth Planet. Sci. Lett.*, 371:156–162, 2013. (Cited on page 53.)

[114] C. Guervilly, P. Cardin, and N. Schaeffer. Turbulent convective length scale in planetary cores. *Nature*, 570(7761):368–371, 2019. (Cited on pages 55, 58, 64, 65, 66, 79, and 80.)

[115] C. Guervilly, D. W. Hughes, and C. A. Jones. Large-scale vortices in rapidly rotating Rayleigh–Bénard convection. *J. Fluid Mech.*, 758:407–435, 2014. (Cited on pages 58, 68, and 74.)

[116] K. Seshasayanan and A. Alexakis. Condensates in rotating turbulent flows. *J. Fluid Mech.*, 841:434–462, 2018. (Cited on pages 58, 66, and 79.)

[117] S. B. Pope. *Turbulent Flows*. Cambridge University Press, 2001. (Cited on page 59.)

[118] J. W. Portegies, R. P. J. Kunnen, G. J. F. van Heijst, and J. Molenaar. A model for vortical plumes in rotating convection. *Phys. Fluids*, 20:066602, 2008. (Cited on pages 59, 63, and 64.)

[119] I. Grooms, K. Julien, J. B. Weiss, and E. Knobloch. Model of convective Taylor columns in rotating Rayleigh–Bénard convection. *Phys. Rev. Lett.*, 104(22):224501, 2010. (Cited on pages 59, 63, and 64.)

[120] See Supplementary Data at `https://iopscience.iop.org/article/10.1209/0295-5075/ac30d6`. (Cited on pages 59, 61, 62, and 79.)

[121] W. Liu, D. Krasnov, and J. Schumacher. Wall modes in magnetoconvection at high Hartmann numbers. *J. Fluid Mech.*, 849:R2, 2018. (Cited on page 61.)

[122] R. Akhmedagaev, O. Zikanov, D. Krasnov, and J. Schumacher. Turbulent Rayleigh–Bénard convection in a strong vertical magnetic field. *J. Fluid Mech.*, 895:R4, 2020. (Cited on page 61.)

[123] T. Ishihara, T. Gotoh, and Y. Kaneda. Study of high-Reynolds number isotropic turbulence by direct numerical simulation. *Annu. Rev. Fluid Mech.*, 41:165–180, 2009. (Cited on page 63.)

[124] U. Frisch. *Turbulence*. Cambridge University Press, 1995. (Cited on pages 68 and 72.)

[125] A. Alexakis and L. Biferale. Cascades and transitions in turbulent flows. *Phys. Rep.*, 767:1–101, 2018. (Cited on page 68.)

[126] G. Boffetta and R. E. Ecke. Two-dimensional turbulence. *Annu. Rev. Fluid Mech.*, 44:427–451, 2012. (Cited on page 68.)

[127] R. P. J. Kunnen, H. J. H. Clercx, B. J. Geurts, L. J. A. van Bokhoven, R. A. D. Akkermans, and R. Verzicco. Numerical and experimental investigation of structure-function scaling in turbulent Rayleigh–Bénard convection. *Phys. Rev. E*, 77(1):016302, 2008. (Cited on page 68.)

[128] C. Sun, Q. Zhou, and K.-Q. Xia. Cascades of velocity and temperature fluctuations in buoyancy-driven thermal turbulence. *Phys. Rev. Lett.*, 97(14):144504, 2006. (Cited on page 68.)

[129] T. Mashiko, Y. Tsuji, T. Mizuno, and M. Sano. Instantaneous measurement of velocity fields in developed thermal turbulence in mercury. *Phys. Rev. E*, 69(3):036306, 2004. (Cited on page 68.)

[130] R. Ni and K.-Q. Xia. Kolmogorov constants for the second-order structure function and the energy spectrum. *Phys. Rev. E*, 87(2):023002, 2013. (Cited on page 68.)

[131] A. M. Rubio, K. Julien, E. Knobloch, and J. B. Weiss. Upscale energy transfer in three-dimensional rapidly rotating turbulent convection. *Phys. Rev. Lett.*, 112(14):144501, 2014. (Cited on pages 68 and 74.)

[132] R. B. Randall. *Spectral Analysis and Correlation*, pages 33–52. Springer, 2008. (Cited on page 69.)

[133] J.-M. Foucaut, J. Carlier, and M. Stanislas. PIV optimization for the study of turbulent flow using spectral analysis. *Meas. Sci. Technol.*, 15(6):1046, 2004. (Cited on page 69.)

[134] R. Savelsberg. *Experiments on free-surface turbulence.* PhD thesis, Eindhoven University of Technology, Eindhoven, The Netherlands, 2006. (Cited on page 69.)

[135] A. Campagne, B. Gallet, F. Moisy, and P. P. Cortet. Direct and inverse energy cascades in a forced rotating turbulence experiment. *Phys. Fluids*, 26(12):125112, 2014. (Cited on pages 72 and 73.)

[136] V. Bouillaut, B. Miquel, K. Julien, S. Aumaître, and B. Gallet. Experimental observation of the geostrophic turbulence regime of rapidly rotating convection. *Proc. Natl. Acad. Sci. USA*, 118(44), 2021. (Cited on page 80.)

[137] D. Dabiri and C. Pecora. *Particle Tracking Velocimetry.* IOP Publishing Bristol, 2020. (Cited on page 81.)

[138] D. Schanz, S. Gesemann, and A. Schröder. Shake-The-Box: Lagrangian particle tracking at high particle image densities. *Exp. Fluids*, 57(5):1–27, 2016. (Cited on page 81.)

[139] R. E. Ecke, X. Zhang, and O. Shishkina. Connecting wall modes and boundary zonal flows in rotating Rayleigh-Bénard convection. *Phys. Rev. Fluids*, 7(1):L011501, 2022. (Cited on page 81.)

Summary

Laboratory study of rotation-dominated convective turbulence

The study of turbulent rotating convection is of paramount importance for the understanding of many features of geophysical and astrophysical flows. The apparently simple interplay of the two competing principal forces, buoyancy and rotation, generates a variety of different regimes that span from convective columns through geostrophic turbulence to the well-known (rotation-unaffected) Rayleigh–Bénard convection. As we know from previous studies, many and vastly unexplored flow behaviors appear beyond certain thresholds of the rotational constraint.

These states are probed for the first time using a novel setup, TROCONVEX, a cylindrical rotating convection cell. Its modular construction allows the investigation of different regions of the parameter space, while its height (up to 4 m) enables an unprecedented view on the so-called geostrophic flow regime that was difficult to study experimentally in the past. TROCONVEX can be operated in two different configurations: a thermally insulated cell, used for measurement of heat transfer and thermal properties of the flow; and an optical accessible configuration for stereoscopic particle image velocimetry (stereo-PIV) measurements, through which flow measurement is possible.

The first chapter of results shows heat transfer and temperature profile measurements in laboratory experiments of rapidly rotating convection in water. We can identify different geostrophic flow regimes: convective Taylor columns (CTC), plumes, geostrophic turbulence (GT), and the novel state of rotation-influenced turbulence (RIT). The different trends of the heat transfer scaling for the known flow states agree well with previous studies, despite differences in boundary conditions and domain composition. We also employ the midheight temperature gradient as a tool to characterize the regimes and we find good agreement with transitions predicted in the literature. The newly explored regime of RIT is separated from GT by investigating the different behavior of the midheight temperature gradient and its characteristic heat transfer scaling.

The following part focuses on the overall flow statistics from stereo-PIV measurements, showing the flow scaling properties of rotating convection at

the extreme parameters reached by TROCONVEX. The measurements show two different behaviors: for low thermal forcing the wall structure dominates the flow, while for more turbulent cases four vortical structures (the quadrupolar vortex) occupy most of the horizontal cross-section.

In the next part of the thesis we show a quantitative analysis of the flow phenomenology using the spatial correlation of both vertical velocity and vertical vorticity. The characteristic length scale of vertical vorticity exhibits a constant behavior for the whole geostrophic regime, linked to the critical wavelength of the columnar structures for onset of convection. On the contrary, for the first time we could see the length scales of vertical velocity that instead grow with increasing thermal forcing and can now be used as a novel tool to identify flow states. The sidewall boundary region shows a wall mode, with two separate lobes of coherent upward and downward vertical velocity, respectively. For low thermal forcing, the inner region shows intrusion of jets propagated from the colliding wall-mode lobes (at opposite sides of the cylinder circumference) that prevent the formation of the typical rather well-organized array of convective Taylor columns shown for horizontally periodic simulations. For the RIT regime, a remarkable quadrupolar organization of the flow, the quadrupolar vortex mentioned above, is found instead of the well-known single large-scale vortex or dipole observed in many horizontally periodic simulations (for certain parameter settings).

In the last chapter this quadrupolar vortex structure is analyzed in more detail. The energy transfer between different scales is investigated in order to understand the main driving mechanism for this phenomenon.

Summarizing, this work analyses the dynamics of the geostrophic regime of rapidly rotating convection. Thanks to the unique properties of the TROCONVEX setup, we gain insights in a region of parameter space that was not accessed before. This work reduces the gap between previous experimental and numerical studies on rotating convection and planetary-scale flows at extreme parameters, thus enabling extrapolation of our findings to these systems, a task that is impossible at lower rotational constraints.

Cover Illustration

Flow field visualization in a vertical slice of TROCONVEX in the the 2 m tank configuration ($\Gamma = 1/5$) showing rotation-affected turbulence at $E = 1 \times 10^{-7}$ and $Ra = 2.1 \times 10^{12}$.

Curriculum Vitae

Matteo Madonia was born on 02-04-1990 in Marino (RM), Italy. He studied physics at the University of Rome Tor Vergata, obtaining his Bachelor of Science degree in 2012 with a thesis based on the work he did during his Erasmus at the University of Twente in 2011. He then continued his studies obtaining in 2016 the Master of Science degree in theoretical physics (statistical mechanics) at the University of Rome Tor Vergata with a master thesis based on the work he did in the Hydraulic Channel Laboratory at the Institute of Marine Engineering in Rome. In May 2017 he started a Ph.D. project at the Eindhoven University of Technology (TU/e) of which the results are presented in this dissertation. Since February 2022 he is employed at Bright Society.

List of publications and conferences

This thesis is based on the following publications

- J. S. Cheng, M. Madonia, A. J. Aguirre Guzmán, and R. P. J. Kunnen. Laboratory exploration of heat transfer regimes in rapidly rotating turbulent convection. *Phys. Rev. Fluids*, 5(11):113501, 2020. **(Chapter 4)**

- M. Madonia, A. J. Aguirre Guzmán, H. J. H. Clercx, and R. P. J. Kunnen. Velocimetry in rapidly rotating convection: Spatial correlations, flow structures and length scales. *Europhys. Lett.*, 135(5):54002, 2021. **(Chapter 6)**

- M. Madonia, A. J. Aguirre Guzmán, H. J. H. Clercx and R. P. J. Kunnen. Experimental flow statistics of rapidly rotating Rayleigh–Bénard convection. *In preparation.* **(Chapter 5)**

Other publications

- X. M. de Wit, A. J. Aguirre Guzmán, M. Madonia, J. S. Cheng, H. J. H. Clercx, and R. P. J. Kunnen. Turbulent rotating convection confined in a slender cylinder: The sidewall circulation. *Phys. Rev. Fluids*, 5(2):023502, 2020.

- A. J. Aguirre Guzmán, M. Madonia, J. S. Cheng, R. Ostilla-Mónico, H. J. H. Clercx, and R. P. J. Kunnen. Competition between Ekman plumes and vortex condensates in rapidly rotating thermal convection. *Phys. Rev. Lett.*, 125(21):214501, 2020.

- A. J. Aguirre Guzmán, M. Madonia, J. S. Cheng, R. Ostilla-Mónico, H. J. H. Clercx, and R. P. J. Kunnen. Force balance in rapidly rotating Rayleigh–Bénard convection. *J. Fluid Mech.*, 928, 2021.

- A. J. Aguirre Guzmán, M. Madonia, J. S. Cheng, R. Ostilla-Mónico, H. J. H. Clercx, and R. P. J. Kunnen. Flow- and temperature-based statistics characterizing the regimes in rapidly rotating turbulent convection in simulations employing no-slip boundary conditions. *Phys. Rev. Fluids*, 7(1):013501, 2022.

Conference contributions

- M. Madonia, A. J. Aguirre Guzmán, H. J. H. Clercx, and R. P. J. Kunnen. Talk: Stereo-PIV measurements of turbulent rotating Rayleigh-Bénard convection in the geostrophic regime. JMBC Turbulence Contact Day, University of Twente, Enschede, NL, September 2021.

- M. Madonia, A. J. Aguirre Guzmán, H. J. H. Clercx, and R. P. J. Kunnen. Flow measurements in rapidly rotating Rayleigh-Bénard convection. 73rd Annual Virtual Meeting of the APS Division of Fluid Dynamics, Chicago, Illinois, USA, November 2020.

- M. Madonia, J. S. Cheng, A. J. Aguirre Guzmán, H. J. H. Clercx, and R. P. J. Kunnen. Poster: TROCONVEX Anatomy of a Rotating Rayleigh-Bénard experiment. Physics@Veldhoven 2020, Veldhoven, NL, January 2020.

- M. Madonia, J. S. Cheng, A. J. Aguirre Guzmán, H. J. H. Clercx, and R. P. J. Kunnen. Talk: Probing Regimes and Transitions in Rapidly Rotating Rayleigh-Bénard Convection. 72nd Annual Meeting of the APS Division of Fluid Dynamics, Seattle, Washington, USA, November 2019

- M. Madonia, J. S. Cheng, A. J. Aguirre Guzmán, H. J. H. Clercx, and R. P. J. Kunnen. Video: Razor-sharp visualizations of rapidly rotating Rayleigh-Bénard convection. 72nd Annual Meeting of the APS Division of Fluid Dynamics, Seattle, Washington, USA, November 2019.

- M. Madonia, J. S. Cheng, A. J. Aguirre Guzmán, H. J. H. Clercx, and R. P. J. Kunnen. Talk: Heat transfer and temperature measurements in extreme rapidly rotating convection. ETC2019 17th European Turbulence Conference, Turin, IT, September 2019.

- M. Madonia, J. S. Cheng, A. J. Aguirre Guzmán, H. J. H. Clercx, and R. P. J. Kunnen. Video: Razor-sharp visualizations of rapidly rotating Rayleigh-Bénard convection. Burgers Symposium 2019, J. M. Burgers Centre for Fluid Dynamics, Lunteren, NL, May 2019.

- M. Madonia, J. S. Cheng, A. J. Aguirre Guzmán, H. J. H. Clercx, and R. P. J. Kunnen. Talk: TROCONVEX: Heat transfer measurements in extreme rapidly rotating convection. Physics@Veldhoven 2019, Veldhoven, NL, January 2019.

- M. Madonia, J. S. Cheng, A. J. Aguirre Guzmán, H. J. H. Clercx, and R. P. J. Kunnen. Talk: TROCONVEX: Heat transfer in rapidly rotating

turbulent convection. Burgers Symposium 2018, J. M. Burgers Centre for Fluid Dynamics, Lunteren, NL, June 2018.

- M. Madonia, J. S. Cheng, A. J. Aguirre Guzmán, H. J. H. Clercx, and R. P. J. Kunnen. Poster: TROCONVEX: A glimpse into extreme rotating convection. Rotating Convection from the Lab to the Stars - EUROMECH Colloquium 599, Leiden, NL, May 2018.
- M. Madonia, J. S. Cheng, A. J. Aguirre Guzmán, H. J. H. Clercx, and R. P. J. Kunnen. Poster: TROCONVEX: A glimpse into extreme rotating convection. Physics@Veldhoven 2018, Veldhoven, NL, January 2018.

Acknowledgements

This PhD dissertation is the result of four intense years full of extraordinary moments and amazing people, travels and isolation. TROCONVEX took me from Italy to the Netherlands and gave me the chance to work within a great group, to start a new life abroad and to study a very fascinating subject with wonderful colleagues.

It is to my supervisors Herman Clercx and Rudie Kunnen that I want to express my profound gratitude for letting me work to this unique PhD project. Herman, your guidance during the critical moments of these years gave me the push I needed to complete this dissertation. Rudie, the support you gave me during the whole journey is inestimable. From the smallest lab issue to the broadest research question, you were always there. Not to mention our cycling talks that may or may not have bored everyone else who sat at the same table as us and which I will really miss.

My sincere thanks go to the members of my committee Marco de Baar, Christian Poelma, Richard Stevens and Nico Dam for reading and evaluating my thesis and to Jonathan Aurnou for his commitment and his valuable comments that improved this dissertation. Thank you prof. Kroesen for chairing the defence.

This research would have been impossible without the collaboration of Jonathan Cheng and Andrés Aguirre-Guzmán, with whom I shared this journey inside the world of rotating Rayleigh–Bénard convection. I am really thankful to them for both our really insightful science meetings but also for our fun times together.

As I said many times during these years: big experiment, big problems! I am glad I could work with great technicians. Without their effort I would still be stuck in the lab trying to get something to work. Thanks Ad, Freek, Gerald and Jørgen.

I extend my gratitude to my friends and colleagues of the Fluids and Flows group (formerly Turbulence and Vortex Dynamics group): Abheeti, Abhineet, Alessandro, Alessandro, Andrei, Anton, Arnab, Bijan, Bojia, Cas, Cem, Cosimo, Federico, Felix, GertJan, Gianluca, Gianmarco, Giorgia, Giulio, Hadi, Haijing, Hanneke, Hirokazu, Ivo, Jan, Jeancarlo, Jos, Josje, Karun, Kim, Lenin, Leon, Maarten, Muhammed, Pinaki, Ralf, Rik, Samuel, Sebastián, Shravan, Shuo,

Steven, Timo, Twan, Vignesh, and Xiao. Thank you all for the all the experiences we shared during borrels, conference trips, courses, dinners and soccer games but also online meetings, seminars and coffee chats. A special thanks to Marjan, who has always been there to help and support me as well as the whole group with great dedication and to Matias with whom I really enjoyed organizing the external seminars and mini-symposiums.

I would also like to thank Xander, Indra, Rein, Youri, Sjoerd, Sietze, Luc, Hannah and Wouter for their contribution to the field of rotating Rayleigh–Bénard convection through their master and bachelor projects.

Un ringraziamento speciale alla (larga) comunità italiana di F&F: Alessandro, Alessandro, Cosimo, Federico, Felix, Gianluca, Gianmarco, Giorgia e Giulio, e a Steven, membro onorario.

During these years I had the luck of being part of the Collegium Vocale Eindhoven, who made my life a lot better with amazing choral music. I would like to thank everyone in it and especially Jan, Paul, Ruud and Tarkan.

Thanks to the many people that came to visit Arianna and me during these years and who made our life abroad much simpler. Thanks Elisa, Gabriele and Giulia, Marta, Bambi and Filippo, Pis, Dario, Giacomo, Italo, Francesco, Davide, Giulio, Picchi, Marta, Manuela, Matteo, Emma and Leo, Giovanni, GP, Hutch, Irene, Filippo and Valeria for letting us share our Eidnhoven life with you.

Grazie Giulia e Francesco (e Flora!) per essere la nostra famiglia italiana qui a Eindhoven.

Obrigado Carina and gracias Julio, you were amazing neighbors (and you would have been the best also against tougher competitors) and you are now amazing friends.

Non starei scrivendo queste parole se non fosse per la mia famiglia, mamma, papà e Elena che in tutti questi anni mi hanno sempre spronato a non accontentarmi mai di fare solo quello che mi riusciva facilmente.

Grazie anche alla mia famiglia acquisita, Anna, Augusto e Matteo, che da ormai più di dieci anni mi hanno accolto tra loro.

Ari, mi ricordo ancora quando ti ho chiamata mentre eri in Francia per dirti della possibilità di iniziare un dottorato a Eindhoven. In pochi mesi abbiamo scelto una casa che avevamo visto solo online e siamo andati a vivere, per la prima volta, insieme. Ora sono passati quasi cinque anni, siamo sposati e abbiamo il nostro piccolo Martino. Questa tesi è dedicata a te, che sei stata il mio punto fisso in questi anni e che lo sarai per tutti gli anni a venire.

Matteo